SSI-DT46215203

Doctor Thesis

A Study on the Design Optimization of the Bipolar Permanent Magnet Type Low-field MRI Device

Xiaohan Kong

A dissertation submitted in partial fulfillment
Of the requirements for the degree of
Doctor of Information Science

Division of System Science and Informatics
Graduate School of Information Science and Technology
Hokkaido University

Doctor Thesis
Submitted to Graduate School of Information Science and Technology
Hokkaido University
In partial fulfillment of the requirements for the degree of
Doctor of Information Science

Xiaohan Kong

Thesis Committee:	**Professor**	**So NOGUCHI**
	Professor	**Hiroyuki KITA**
	Professor	**Hajime IGARASHI (Chief examiner)**
	Professor	**Atsushi KONNO**

A Study on the Design Optimization of the Bipolar Permanent Magnet Type Low-field MRI Device

Xiaohan Kong

Abstract

In recent years, portable low-field Magnetic resonance imaging (MRI) devices have been developed to complement high-field superconducting MRI. Portable low-field MRI devices offer advantages such as being lightweight, movable, and providing low-cost diagnostic services compared to the commonly used high-field MRI devices. However, there are still some challenges to be addressed, particularly concerning the electromagnetic (EM) structure, including gradient coil design and permanent magnets design. Based on how the main magnetic field is generated, there are different types of low-field MRI device. Among these, the bipolar permanent magnet type low-field MRI device is commonly used due to its advantages, such as good magnetic field homogeneity, structural compactness, and an open imaging area. However, some problems remain to be studied, especially about the EM structure including gradient coil design and permanent magnets design.

In this paper, we focus on the design optimization of the bipolar permanent magnet type low-field MRI device, the main content of the thesis is as follows:

In Chapter 1, the research background and motivations are introduced, and the contributions of this study are also summarized.

In Chapter 2, a novel method for designing gradient coils for low-field MRI devices is

proposed. The proposed method considers the effect of magnetic materials, particularly anti-eddy plates, by introducing image dipole currents. In the optimal design of gradient coils, the effect of ferromagnetic materials is minimized to obtain highly linear fields. The magnetic field measurement results and phantom images reveal the validity of the proposed method.

In Chapter 3, a design method for Z-gradient coils in low-field MRI systems is proposed, focusing on enhancing anti-eddy performance. The newly introduced design procedure significantly improves the anti-eddy performance of the coils. Measurement and imaging results demonstrate that the optimal coil exhibited superior anti-eddy performance compared to conventional coils.

In Chapter 4, a multi-fidelity topology optimization method has been proposed to alleviate the local optima problem. This method simplifies the design difficulty by dividing the optimization into sub-problems at the physical level. The proposed method shows a better performance than the conventional method in the design of low-field MRI devices.

In Chapter 5, a passive shimming method is proposed for fine-tuning the static magnetic field in a low-field MRI device. A test case validated the effectiveness of this approach, reducing non-uniformity from 10,000 ppm to 125 ppm after three iterations.

In Chapter 6, conclusions and future works are discussed.

Keywords: portable magnetic resonance imaging, gradient coil, permanent magnets, topology optimization, evolutionary algorithm.

∗ Doctoral Thesis, Course of Systems Science and Informatics, Graduate School of Information Science and Technology, Hokkaido University, SSI-DT46215203, September 10, 2023.

List of Contents

List of Figures

List of Tables

Chapter 1 Introduction

1.1 Background

Magnetic Resonance Imaging (MRI) [1-2] is a crucial diagnostic tool known for its noninvasive imaging capabilities of physiological structures without using radiation. However, conventional high-field MRI scanners (1.5T and 3T) have limitations, such as strict operating environment requirements, lack of mobility due to their weight, making them less practical in certain situations. To address these challenges, low-field MRI devices have been developed as supplementary tools to high-field superconducting MRI. As shown in Fig. 1.1, low-field portable MRI offers advantages like being lightweight, mobile, and providing cost-effective diagnostic services compared to the commonly used high-field MRI scanners [3]-[7].

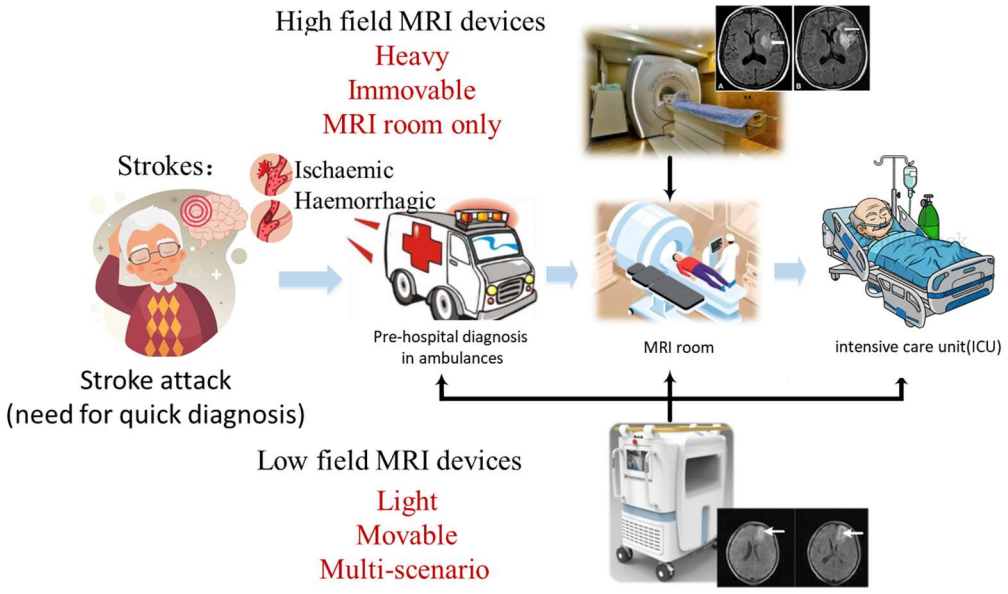

Fig. 1. 1 Comparison between high-field and low-field MRI devices

There are several types of low-field MRI equipment based on how the main magnetic field is generated, such as electromagnet-type [8]-[10], Halbach-magnet-type [11]-[13], and bipolar-magnet-type [3]-[5], [14]-[17]. Due to the large size of electromagnet-type devices and the cooling requirement, they are not suitable for mobile scenarios. Commonly used portable low-field MRI systems are permanent magnet-based, including Halbach-magnet-type, and bipolar-magnet-type. There are several representing devices developed by teams around the world, as shown in Fig. 1.2. Among them, the bipolar magnet-type device is generally preferred due to its advantages, including good magnetic field homogeneity, structural compactness, and an open imaging area. Researchers have conducted extensive and effective investigations in this field. However, certain issues still require further study, particularly concerning the EM structure, including gradient coil design and permanent magnets design.

Type	Halbach-type	
Team	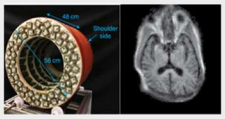 Havard University (America, 2017)	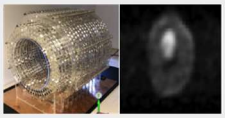 Leiden University (Netherlands, 2019)
Field strength	64 mT	50 mT
Non-uniformity	27800 ppm	2500 ppm
Weight	122 kg	120 kg
Shortcoming	Image distortion	Image distortion
Type	Bipolar-type	
Team	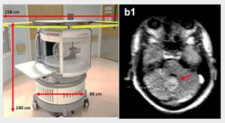 Hyperfine (America, 2021)	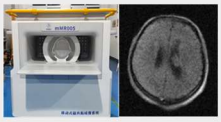 Chongqing University (China, 2019)
Field strength	64 mT	50 mT
Non-uniformity	250 ppm	100 ppm
Weight	630 kg	500 kg
Shortcoming	Heavy	Heavy

Fig. 1. 2 Representative types of portable low-field MRI devices

· **Gradient coil design considering field distortion effects.**

Fig. 1.3 illustrates the electromagnetic (EM) structure of the bipolar-magnet-type low-field MRI device, which includes essential components such as a permanent magnet, gradient coils, and the RF coils, as well as an iron yoke and an anti-eddy plate.

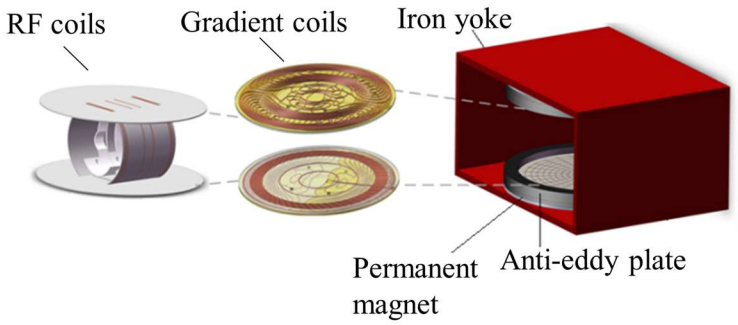

Fig. 1. 3 Overall structure of the bipolar-magnet-type low-field MRI device

MRI scanners utilize gradient coils to generate linear gradient fields that enable spatial localization in the region of interest (ROI). As shown in Fig. 1.4, three sets of bipolar gradient coils (X, Y, and Z gradient coil) produce a linear gradient field in ROI along x, y, and z directions, respectively. In this system, all gradient coils are designed using the planar coil structure. Both the X and Y gradient coils have the same structure, consisting of two pairs of semicircular coils, with opposite currents flowing through the two semicircular coils. The Z gradient coil is composed of planar circular coils. Gradient fields cause changes in the resonance frequency of atomic nuclei at different locations. This variation leads to spatial encoding during image acquisition, enabling resolution and localization of different positions within the image. As shown in Fig. 1.4, the voxel (marked with red color) has a unique field strength, considering the super-position of gradient fields in three directions.

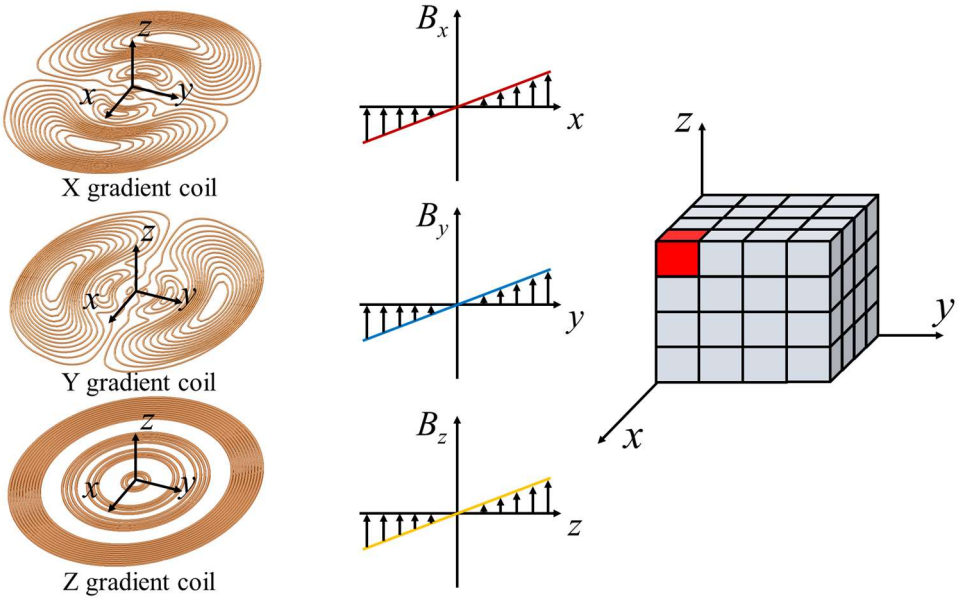

Fig. 1. 4 Working principle of gradient coils

Ensuring high linearity in gradient fields is crucial for accurate imaging. In bipolar magnet-type devices, switching gradient fields can induce undesirable eddy currents in the surrounding conducting materials. To counter this issue, active shielding coils or anti-eddy plates are commonly employed. Active shielding coils generate a reverse magnetic field to cancel out the original field in the shielded areas. Although they effectively reduce eddy currents, they can also lead to decreased efficiency by offsetting the field in the target region. Qualified shielding effects and efficiency can be obtained at similar time only when the distance between the main and shielding coil is considerable. Different from active shielding coils, anti-eddy plates offer a more direct and convenient solution for gradient field shielding. However, the high-permeability material used in these plates can distort the gradient field in the target region, as shown in Fig. 1.5. Therefore, it is essential to consider the magnetic effect of the surrounding structures during the gradient coil design process to prevent image distortion.

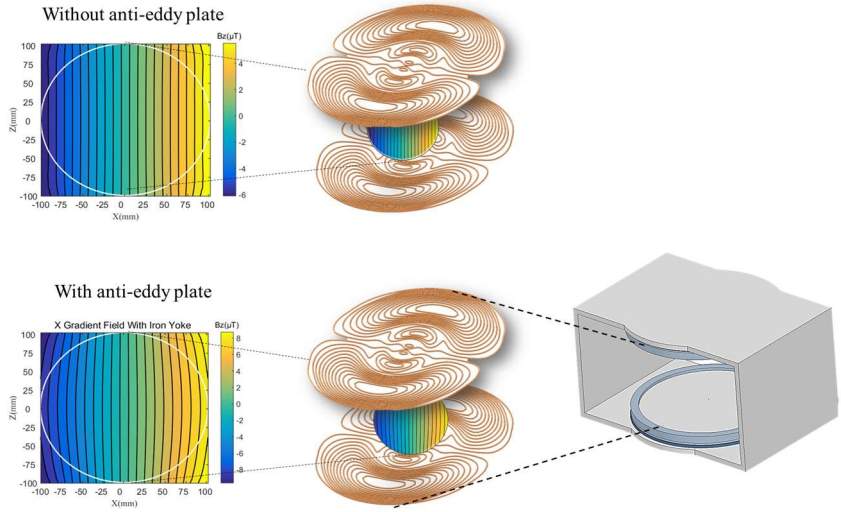

Fig. 1. 5 Field distortion effects of the surrounding structures

Even in devices using active shielding coils, it's important to account for the ferromagnetic effects of the pole piece and iron yoke during the design process to achieve optimal performance and image quality. The methods used for designing gradient coils in MRI scanners can be categorized into two types: discrete winding [18] and distributed winding methods [19]-[23]. The distributed winding method, which includes stream function [19], target field [20, 21], and equivalent magnetic dipole (EMD) methods [22-24], is more flexible as it doesn't require predetermined coil shapes. Among these methods, the EMD method [22], introduced by Stuart Crozier and Hector Sanchez Lopez, has been used for designing MRI gradient coils. However, in many of these designs, the impact of magnetic materials has been overlooked, leading to issues with gradient field linearity and image distortion.

In other areas, some studies have explored the influence of ferromagnetic materials in coil designs. For instance, Zhao [25] and Yang [26] focused on designing active shielding coils to create a zero-field environment. They utilized the image method [27, 28] to consider the ferromagnetic effects of a magnetic shielding room and a closed magnetically shielded cylinder, respectively. However, these studies have not taken into account the image representation for

laminated structures like anti-eddy plates. Furthermore, there has been limited exploration of gradient coil design for low-field MRI systems while considering the effects of ferromagnetic materials.

·Gradient coil design considering eddy current effects.

When the gradient magnetic field in an MRI scanner changes rapidly, it induces eddy currents in nearby conductive materials. Despite the use of anti-eddy plates to shield the gradient field in MRI systems, nearby conducting structures are still affected by eddy currents, leading to image distortion, especially when using the z-axis for phase-encoding. The principle of how gradient eddy currents affect imaging can be explained briefly using Fig. 1.6. The gradient pulse becomes elongated due to the superposition of secondary magnetic fields generated by eddy currents. This elongation in the rising edge of the gradient pulse waveform leads to spatial mis-localization, consequently resulting in geometric distortions in the imaging results.

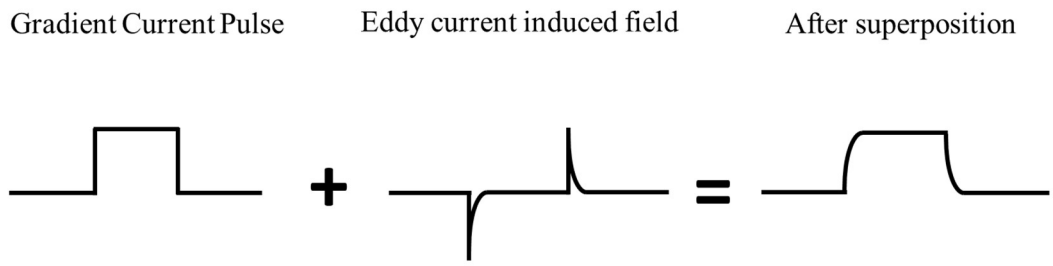

Fig. 1. 6 Eddy current influenced gradient pulse

Unlike X and Y gradient coils, which exhibit smaller eddy effects due to their opposing secondary magnetic field response in the region of interest (ROI), Z gradient coils are more susceptible to these effects. Previous studies [29-30] on gradient eddy currents in MRI systems have mainly focused on permanent-type MRI systems and have not considered the presence of anti-eddy plates. However, due to the significant impact of anti-eddy plates on the gradient magnetic field distribution, it is essential to evaluate gradient eddy currents in the presence of

these plates. The evaluation process for gradient eddy currents in low-field NMR systems is computationally intensive and challenging to integrate directly into the coil design process. Therefore, a simpler and more efficient method for eddy current evaluation is needed to effectively incorporate it into the coil design process.

In general, the desired characteristics of a gradient coil include high gradient efficiency, low inductance, and minimal gradient nonlinearity [31]. Designing Z gradient coils becomes a multi-objective optimization problem (MOP) due to conflicting performance requirements. However, in the case of gradient coil design for low-field MRI systems, previous studies [32-33] have examined various parameters individually without considering their interactions, and gradient eddy currents have been overlooked. Similarly, high-field systems' coil design as an MOP has neglected gradient eddy currents [34-35]. It's important to note that low-field MRI systems present unique challenges regarding eddy currents that differ from high-field systems. Thus, special attention should be given to addressing the issue of eddy currents in low-field MRI systems.

· **Topology design of the permanent magnets and iron yoke.**

The design of the magnet structure is a critical aspect of low-field MRI devices. The purpose of low-field MRI device is to reduce the magnet weight, shrink the magnet size, and achieve a lightweight and portable system. Therefore, the challenge lies in generating a uniform static magnetic field in the specified region using fewer magnetic materials. Currently, as introduced before, there are two main types of permanent magnet structures used in low-field MRI: the Halbach-type and the bipolar-type.

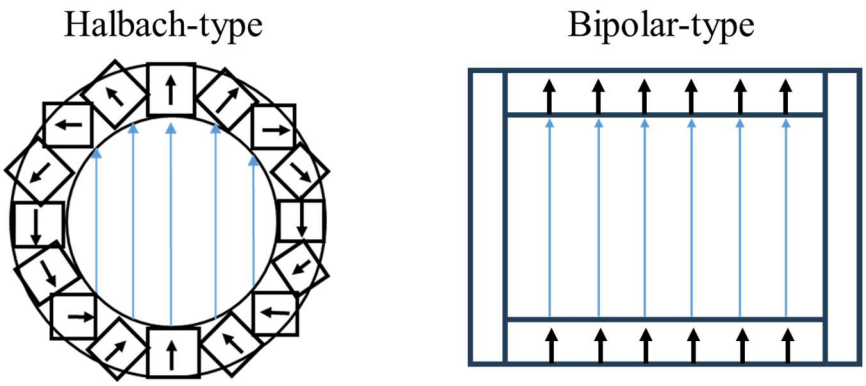

Fig. 1. 7 Halbach-type and bipolar-type magnet structure

The first type is based on the Halbach magnet structure. This design is adjusted from the ideal Halbach ring to achieve high uniformity and high field strength. Researchers at Harvard Medical School, led by Cooley [36], used a genetic algorithm to optimize the sparse structure of Halbach magnetic blocks, resulting in a lightweight permanent magnet structure. This magnet achieved a field strength of 64 mT, with a diameter of 29 cm and a weight of 122 kg. However, the magnetic field non-uniformity was as high as 27,800 ppm, leading to severe image distortion. Another study by O'Reilly [37] and colleagues from Leiden University used a genetic algorithm to design a double-layered Halbach array magnet with a diameter of 27 cm. This magnet weighed 75 kg and achieved an average field strength of 50.4 mT with a non-uniformity of about 2500 ppm within a 20 cm imaging region. Similarly, researchers from Singapore, led by Huang [38], designed a Halbach structure composed of rectangular magnetic blocks that generated a 101.5 mT magnetic field in a cylindrical target region with a diameter of 200 mm and height of 125 mm, but the non-uniformity was still 7500 ppm. Patrick and colleagues [39] designed a lightweight cap-shaped unilateral magnet for brain imaging, weighing 6.3 kg, with an average magnetic field of 63.6 mT, and a non-uniformity of 69,200 ppm. Although the imaging results were not satisfactory, this study demonstrated the feasibility of lightweight ultra-low-field magnets. In China, WAMI Corporation reported the development of a research-stage whole-body Halbach

ultra-low-field MRI device weighing less than 800 kg, but no imaging results were reported. The characteristics of Halbach magnets include lightweight construction but poor uniformity, leading to challenges in achieving satisfactory imaging results.

The second type is based on the bipolar plate structure, which is more widely used. This design consists of two opposing permanent magnet plates combined with iron yokes to generate a uniform magnetic field in the target region. The team from Hyperfine [40] in the United States used a separated magnet block structure to construct the bipolar plate magnet with a total weight of 630 kg, producing a magnetic field strength of 64 mT in a head-sized target region. The team from the University of Hong Kong [41] used a bipolar plate magnet to generate a 55 mT static magnetic field in the target region, with a device weight of 750 kg and a non-uniformity of 250 ppm. The device developed by the Chongqing University team [42] has a total weight of approximately 500 kg and can generate a static magnetic field with a strength of 50 mT and non-uniformity of less than 100 ppm within a spherical target area of 200 mm.

Compared to Halbach magnet structures, bipolar plate magnets can achieve higher uniformity in head-sized target regions, and both the magnet and magnetic shielding system have considerable weight reduction potential. However, most of the current optimization methods are based on empirical design or parameter optimization, and there is still a lack of effective global topology optimization methods. Topology optimization [43-44] is a promising method for generating innovative structures without being constrained by predetermined shapes. However, when dealing with complex optimization problems that involve multiple design objectives and materials (take the problem shown in Fig. 1.8 (a) for example), there is a risk of encountering local solutions. This is due to non-convex, multi-peak solution space (e.g., Fig. 1.8(b)).

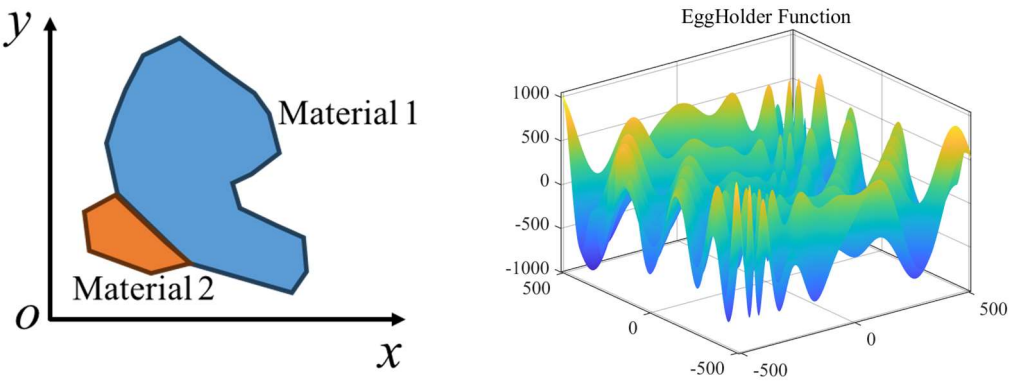

(a) (b)

Fig. 1. 8 Complex topology optimization problem. (a) Schematic diagram of a complex topology optimization problem, and (b) solution space of Egg holder function, as an example of non-convex, multi-peak solution space.

This issue arises due to the high-dimensional, nonconvex, and nonlinear nature of the solution space. It becomes particularly challenging when there are objective functions that exhibit significant variations concerning the structure, such as field non-uniformity. In topology optimization problems, evolutionary algorithms are commonly used for optimal search. Although advanced algorithms [45] have been developed to tackle these challenges, obtaining a stable optimal solution remains difficult. Therefore, it is essential to address this issue at the physical level of topology design. In other words, considering the underlying physical aspects of the problem can help overcome the limitations associated with local solutions and enhance the effectiveness of topology optimization for complex problems.

- **Passive Shimming of Static Magnetic Field**

In the fabrication process, the machining errors and assembly errors result in some deviation of the actual magnetic field strength and field non-uniformity from the calculation results. After assembly, the main magnetic field requires further field shimming. To achieve required field uniformity, two methods have been developed: active shimming technology [46,47] and passive

shimming technology [48,49]. Active shimming technology involves applying currents to specific coils to compensate for the non-uniformities in the static magnetic field. However, active shimming may require a significant amount of space, and it can encounter challenges in compensating for high-order harmonics. In contrast, passive shimming technology typically utilizes magnetized steel components or permanent magnets to adjust the static magnetic field. Passive shimming is an effective method that does not require additional coils, which can be advantageous in terms of space and cost considerations. In low-field MRI devices, the static field strength is not sufficiently high to fully magnetize the steel components. Therefore, permanent magnets are better suited for shimming in low-field MRI devices. To describe this problem, a two-dimensional (2-D) model is provided, as shown in Fig. 1.9 (a). Shimming magnets are positioned on the surface of bipolar magnets, and the distribution of shimming magnets presents a vast array of possibilities.

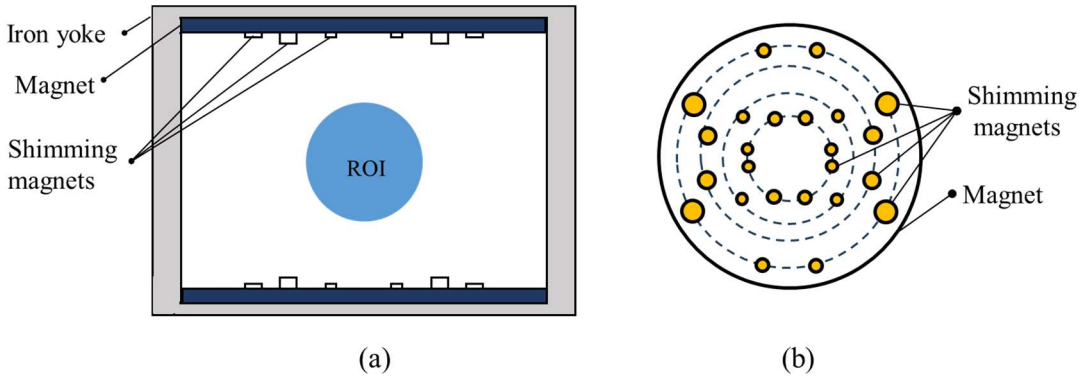

Fig. 1. 9 Schematic diagram of passive shimming in the low-field MRI device. (a) Side view, and (b) top view.

To determine the best distribution of shimming components, two methods are developed: the target field method [50–53], and the harmonic method [54,55]. The target field method aims to minimize the difference between the target field and the current field, while the harmonic method focuses on reducing disparities between the targeted harmonics and the current ones. To address

the optimization problem in shimming design, linear programming (LP) is commonly employed [50–53] due to its rapid computational speed. The field contribution of shimming components can be easily evaluated using theoretical solution based on magnetic moment theory [53].

However, when it comes to field shimming in low-field MRI devices using permanent magnets, the presence of the iron yoke alters the magnetic field of the shimming magnet. The analytical formula mentioned above is no longer applicable. In order to determine the best positions of the shimming magnets, we need to evaluate the magnetic field contributions to the ROI from shimming magnets of different sizes and positioned at different locations. When considering precise field evaluation, the overall model cannot be simplified into a 2-D model. And evaluating field distribution of three-dimensional (3-D) models using FEM method requires a significant amount of computational time, leading to lower efficiency in the entire shimming process. We need to develop a method for the fast determination of positions of shimming magnets in low-field MRI devices.

1.2 Objectives

This thesis attempts to develop methods for the optimal design of the bipolar permanent magnet type low-field MRI device. In detail, the objectives are:

- to develop a gradient coil design method considering field distortion of surrounding ferromagnetic structures, and to reduce image distortion caused by poor gradient linearity.
- to develop a method especially for the Z gradient coil design considering eddy current effects of surrounding conducting structures, and to reduce image artifacts caused by the gradient eddy currents.
- to develop a topology optimization method that used for designing a new structure of the permanent magnet as well as iron yoke, and to realize high field strength, high

uniformity and low weight meanwhile.

・to develop a method which can realize fast passive shimming, and to improve the uniformity of the static magnetic field to the level required for imaging.

1.3 Contribution of the Study

1.3.1 Gradient Coil Design Considering Field Distortion Effects.

In this study, a comprehensive procedure for designing gradient coils specifically for low-field MRI devices was introduced, with a focus on considering the impact of ferromagnetic materials, especially anti-eddy plates. The original contributions of this research are as follows:

(a) The laminated anti-eddy plate was simplified to a homogenized magnetic plate, and its equivalent permeability was extracted using an analytical solution. This simplification significantly reduced the complexity of the structure.

(b) The ferromagnetic effects of the homogenized magnetic plate were represented using image current loops based on the image current method.

(c) A novel equivalent image magnetic dipole (EIMD) method was proposed by combining the aforementioned approaches. This method effectively accounted for the ferromagnetic effects by adding the image magnetic dipoles (image current loops) as magnetic field sources.

(d) The proposed EIMD method was applied to a real low-field MRI device, and both field measurement and imaging results demonstrated its effectiveness in reducing field distortion caused by ferromagnetic materials, particularly the anti-eddy plates.

1.3.2 Gradient Coil Design Considering Eddy Current Effects.

This study introduces a design procedure for the Z-gradient coils in low-field MRI systems, with consideration of the gradient eddy current effects. The original contributions of this research are as follows:

(a) To enable fast evaluation of gradient eddy currents, a simplified 2-D FEM model is introduced. The final criterion for selecting the optimal coil is based on its anti-eddy performance as predicted by this model.

(b) A total of 158 Z-gradient coil patterns are generated from the 1-D stream function method, from which the approximated Pareto solutions to MOP are found. Then, considering nonlinearity, gradient efficiency, and inductance simultaneously, the nine best candidates are selected from the Pareto front. The optimal coil is determined by comparing the anti-eddy performance of the nine coils based on the proposed 2-D FEM model.

(c) The optimal coil was fabricated and used for T2-weighted imaging. A comparison was made between our method and the conventional method. The results show a reduction in the eddy currents effects with the proposed design method, thus validating the effectiveness of our method.

1.3.3 Topology Design of the Permanent Magnets and Iron Yoke.

This study proposes a multi-fidelity method to alleviate the local optima problem in the complex topology optimization process. The original contributions of this research are as follows:

(a) A multi-fidelity topology optimization method that decomposes the complex optimization problem into sub-problems at the physical level. The proposed method outperforms conventional single-fidelity methods in the design of low-field MRI device structures. This approach successfully generates novel structures in both two-dimensional (2-D) and three-dimensional (3-D) spaces.

(b) The multi-fidelity topology optimization method proposed in this study was utilized for designing both the permanent magnets and iron yoke. Through this approach, novel and irregular topology structures were generated without relying on predetermined designs. These newly developed structures exhibited superior performance compared to conventional regular structures.

1.3.4 Passive Shimming of Static Magnetic Field

This study proposes a fast passive shimming method to predict the best distribution of shimming magnets in the low-field MRI device.

(a) A fast field evaluation model for single shimming magnet is established, combining Finite Element Method (FEM) with a theoretical solution.

(b) The LP method is employed to determine the optimal distribution of shimming magnets, achieving a non-uniformity of 125 ppm using this method.

1.4 Thesis Outline

This thesis is structured as follows:

Chapter 1: Introduction

The research background, objectives and contributions of the thesis are outlined.

Chapter 2: Gradient coil design considering field distortion effects

This chapter presents the proposed gradient coil design method, taking into account field distortion effects. The optimization results of the proposed method are compared with the conventional method. Additionally, the measurement and imaging results are analyzed to demonstrate the effectiveness of the proposed method.

Chapter 3: Z gradient coil design considering the eddy current effects

This chapter introduces the Z-gradient coil design method considering the effects of gradient eddy currents. The design results are discussed, and experimental eddy current responses and images are compared with those obtained using conventional coils to emphasize the advantages of the proposed method.

Chapter 4: Multi-fidelity topology optimization for permanent magnets and iron yoke design

The multi-fidelity method is introduced as a solution to address the issue of local optima in

complex topology optimization processes. The effectiveness of this method is demonstrated through its application to the design of permanent magnets and iron yokes in both two-dimensional and three-dimensional spaces. The optimization results are carefully analyzed and compared with those obtained using conventional single-fidelity methods.

Chapter 5: To achieve passive shimming for compensation of fabrication errors, a fast design method for determining the best distribution of shimming magnets is proposed. This method combines a simple field evaluation model by combining FEM and theoretical solutions, and utilizes LP to realize fast optimization. This method significantly improves the shimming efficiency and can compensate for the field error introduced by machining and assembly errors.

Chapter 6: Conclusion, to give a summary of the researches and future research directions.

Chapter 2 Gradient Coil Design Considering Field Distortion Effects

2.1 Structure of the Bipolar Magnet-type MRI Device

A detailed side view of the structure with corresponding sizes is presented in Fig. 2.1.

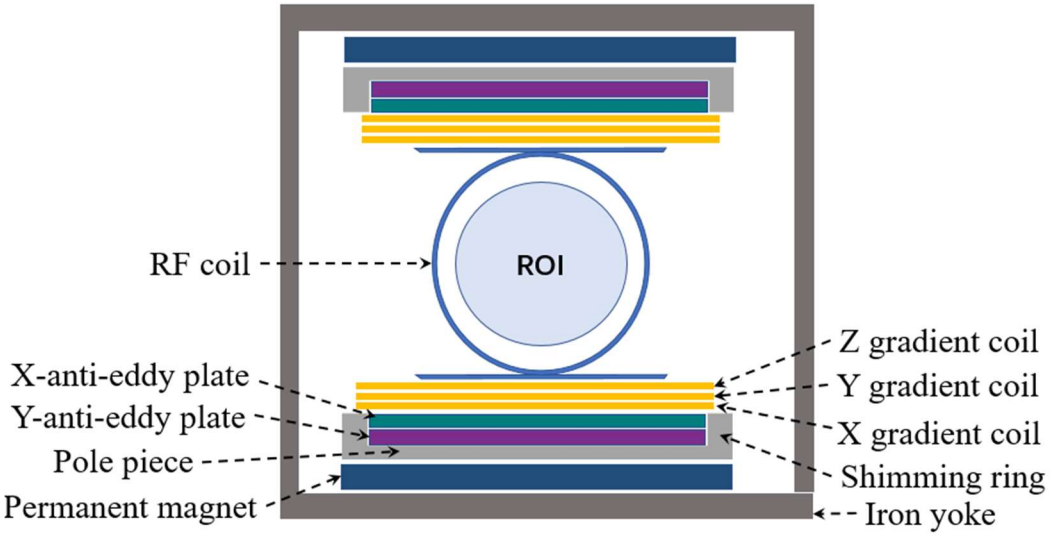

Fig. 2. 1 Representative types of portable low-field MRI devices

The functions of each part are as follows:

(i) The bipolar permanent magnets generate a vertically homogeneous magnetic field in the region of interest (ROI). (ii) The gradient coils produce linear gradient fields in three vertical directions (x, y, and z) within the ROI. These spatially varying magnetic fields enable image localization, phase encoding, and frequency encoding. (iii) The RF coils, including excitation and receive coils, generate alternating fields for magnetic resonance and receive RF signals from the samples. (iv) The laminated vertical silicon steel sheets used in the anti-eddy plates shield the gradient field and reduce eddy currents. (v) The stainless-steel iron yoke guides the static magnetic flux to form a closed loop. (vi) The pole piece, composed of non-alloy

quality steel, enhances the uniformity of the magnetic field. (vii) The shimming ring, made from a material similar to that of the pole piece, concentrates the magnetic flux at the target region. Due to the high permeability of the anti-eddy plates, pole piece, shimming ring, and iron yoke, their influence on the gradient field is significant. However, representing the entire complex structure analytically is impractical. Thus, a simplified model was introduced to capture and represent these effects effectively. The anti-eddy plate is the closest ferromagnetic structure to the gradient coils, as shown in Fig. 1 (b), with a higher permeability than that of other materials. This considerably affects the gradient field and image. The homogenized permeability of the anti-eddy plate needed for the proposed design method was evaluated.

2.1.1 Anti-eddy Plates Modeling

An anti-eddy plate, also called the shielding plate, is used to shield the permanent magnets and pole pieces from the gradient field to reduce the eddy current effect. It is made of multiple thin, high permeability silicon-steel sheets that are laminated together but insulate each other. Fig. 2.2 shows the structures of the X gradient coil and X anti-eddy plate, wherein the magnetic field is constrained in the anti-eddy plate owing to its high permeability in the *x*-direction. Moreover, the eddy current induced in the plate is cut off by the air gap (dotted blue circle) and is limited to the thin area of the steel sheets (blue circle). This special structure maintains high permeability but reduces electrical conductivity. The Y and X gradient coils generally have a similar structure. As for the Z gradient coil, the shielding effect is the superposition of that of the X and Y anti-eddy plates put together. Hence, the analyses that follow will only focus on the X gradient coil. Evaluating the laminated structure using the FEM is difficult; therefore, we employed a homogenized model by extracting the homogenized permeability using an analytical solution, as shown in Fig. 2.3. Their thicknesses are the same and defined as w. The homogenized permeability along the laminated direction $\mu_{\parallel}$ is greater than that in the perpendicular direction

$\mu_\perp$. Consequently, they must be evaluated separately. t_{steel} and t_{gap} represent the thicknesses of the steel sheets and air gap, and μ and μ_0 denote the permeability of the steel sheets and vacuum, respectively.

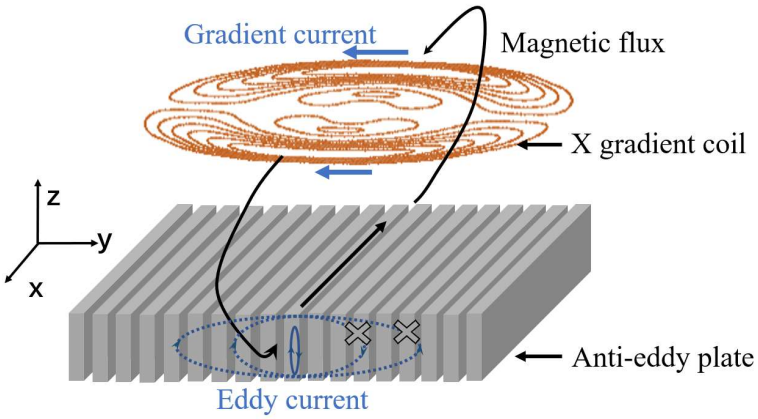

Fig. 2. 2 Structures of X gradient coil and corresponding X anti-eddy plate (in the X anti-eddy plate, the magnetic flux goes along the x-direction due to its high permeability).

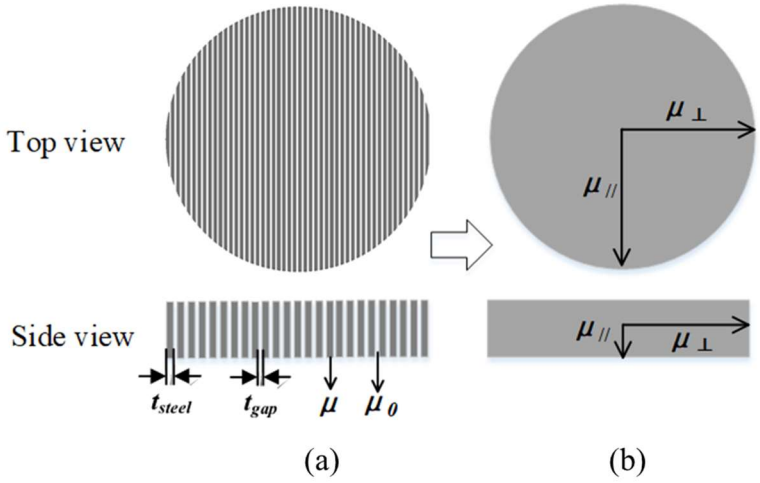

Fig. 2. 3 Top and side views of (a) the laminated steel sheets and (b) homogenized plates.

The homogenized permeability along the lamination and vertical directions $\mu_\parallel$ and $\mu_\perp$, respectively, can be obtained using equations (2.1) and (2.2). Detailed formulas are provided in Section 2.5.1.

$$\mu_\parallel = \alpha\mu + (1-\alpha)\mu_0. \tag{2.1}$$

$$\mu_{\perp} = \frac{\mu\mu_0}{\alpha\mu_0 + (1-\alpha)\mu} \tag{2.2}$$

where α is the filling rate (volume fraction) of the laminated structure, calculated as:

$$\alpha = \frac{t_{steel}}{t_{steel} + t_{gap}} \tag{2.3}$$

$\mu_{\parallel r}$ and $\mu_{\perp r}$ are defined as the relative homogenized permeability along the lamination and vertical directions.

$$\mu_{\parallel r} = \frac{\mu_{\parallel}}{\mu_0} \tag{2.4}$$

$$\mu_{\perp r} = \frac{\mu_{\perp}}{\mu_0} \tag{2.5}$$

In order to verify the accuracy of the homogenization method, four different anti-eddy plates were considered to compare the analytical results with the finite element calculations. The steel sheet used in this permanent-magnet-type MRI device is 27RK095 electrical steel produced by BAO STEEL, CHINA. It has a relative permeability μ_r of 40000 and a thickness t_{steel} of 0.27 mm. We set t_{steel} and μ_r as constants, then $\mu_{\parallel r}$ and $\mu_{\perp r}$ are determined by t_{gap}. Four cases have different t_{gap}, causing their homogenized permeability to vary. The parameters of these four cases are listed in Table 2.1

. In the lamination direction, the increase in t_{gap} leads to a decline in $\mu_{\parallel r}$. In the perpendicular direction, the $\mu_{\perp r}$ remained low, which is close to the vacuum.

Table 2. 1 Parameters of Four Cases

Case	t_{steel} (mm)	t_{gap} (mm)	α	$\mu_{//r}$	$\mu_{\perp r}$
1	0.27	2.43	0.1	4000	1.11
2	0.27	10.54	0.025	1000	1.02
3	0.27	21.37	0.0125	500	1.01
4	0.27	43.13	0.0062	250	1.01

Taking the X gradient coil as an example, the magnetic flux along the laminated direction (x-direction) is the absolute dominant component in the region of steel sheets. Hence, steel sheets were simplified by a homogenized plate that had isotropic permeability $\mu_{\parallel r}$, the permeability along the perpendicular direction $\mu_{\perp r}$ was neglected. The laminated and homogenized models shown in Fig. 2.4 were analyzed using the FEM to verify the homogenization. In the homogenized model, the laminated structure was replaced with a homogenized plate with an anisotropic permeability $\mu_{\parallel r}$.

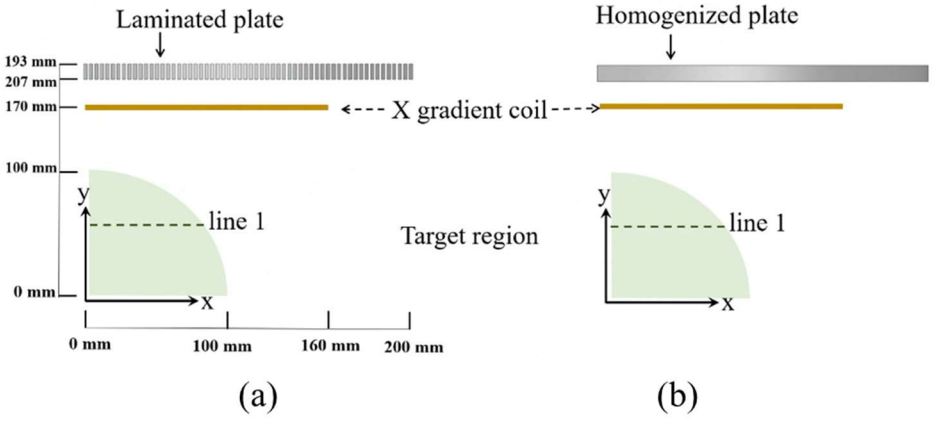

Fig. 2. 4 Models used to verify the homogenized permeability. (a) Laminated and (b) homogenized models

In our system, the static magnetic field is along the z-direction. For the X gradient coil, the z-component of gradient magnetic field induction (B_z) varies linearly along the x-direction. Superposing B_z to the static field causes a frequency variation of protons, a slice can be selected

perpendicular to the gradient direction. Thus, we here pay attention to B_z.

For the four cases with different permeability, the magnetic field B_z along line 1 was plotted in Fig. 2.5 to compare the B_z of homogenized and laminated models. The solid lines represent B_z in the homogenized models, while the dotted lines represent those of the laminated models. All the cases have good agreements with a maximum error lower than 1%. The curves in the blue dotted box are enlarged to see the discrepancies (located in the right lower side), which decrease from case 1 to case 4, wherein the t_{gap} gradually increases. This indicates that this homogenized model has higher accuracy when the steel sheets are more closely laminated.

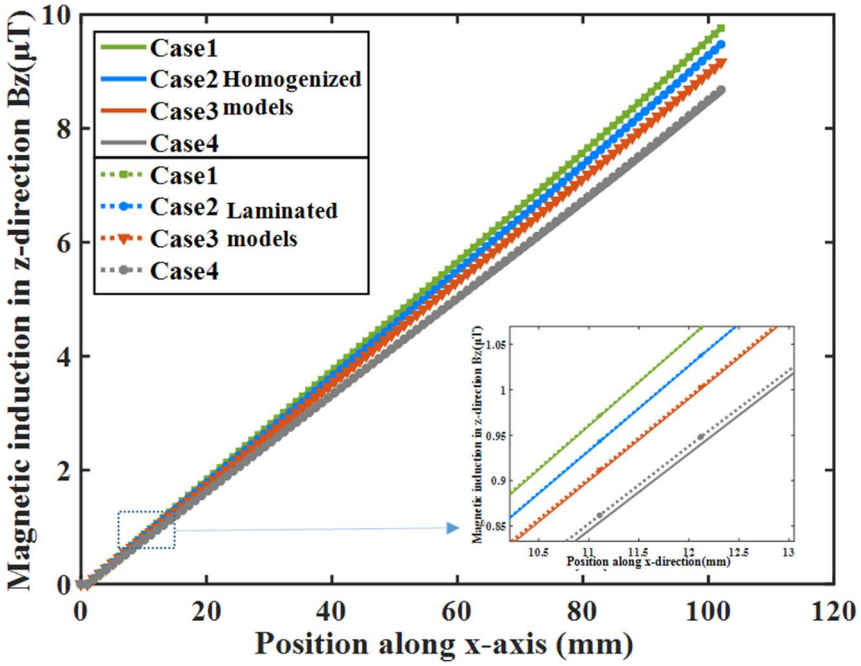

Fig. 2. 5 Simulated Bz comparison between laminated and homogenized models along line 1.

In the permanent-magnet-type MRI device, the permeability of the silicon-steel sheets is 0.05 H/m and the relative permeability μ_r is 40000. The thicknesses of steel sheets t_{steel} and air gap t_{gap} are 0.27 mm and 0.02 mm, respectively. Hence, the filling rate α was calculated to be 0.931. According to (4) and (5), the homogenized relative permeability in the lamination direction $\mu_{\parallel r}$ was 37200, whereas the relative permeability $\mu_{\perp r}$ is 14.5 in the perpendicular direction. For the X gradient coil, the magnetic flux mainly goes along the lamination direction,

and the anti-eddy plate can be replaced by a homogenized metal plate with an isotropic permeability of 37200.

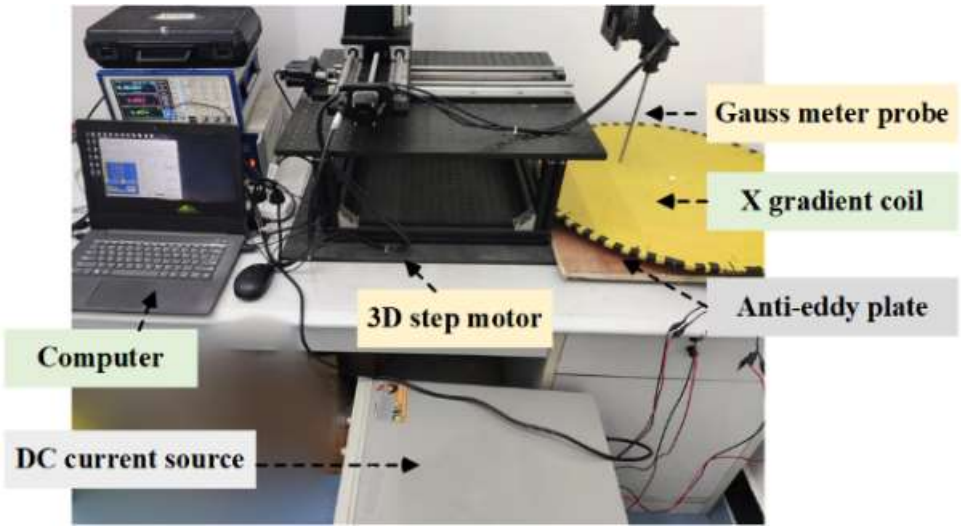

Fig. 2. 6 Magnetic field measurement platform.

To verify the calculation results, the measurement platform shown in Fig. 2.6 was established. A Gauss meter probe (FW. Bell 8030, resolution: 0.1 nT, accuracy: ±0.05 % of reading) was fixed on a three-dimensional (3D) step motor and the current in the X gradient coil was 1 A. B_z was measured on the observation surface and compared to simulation results. As illustrated in Fig. 2.7, the simulation model replaced the X anti-eddy plate with a homogenized plate and had an isotropic relative permeability of 37200.

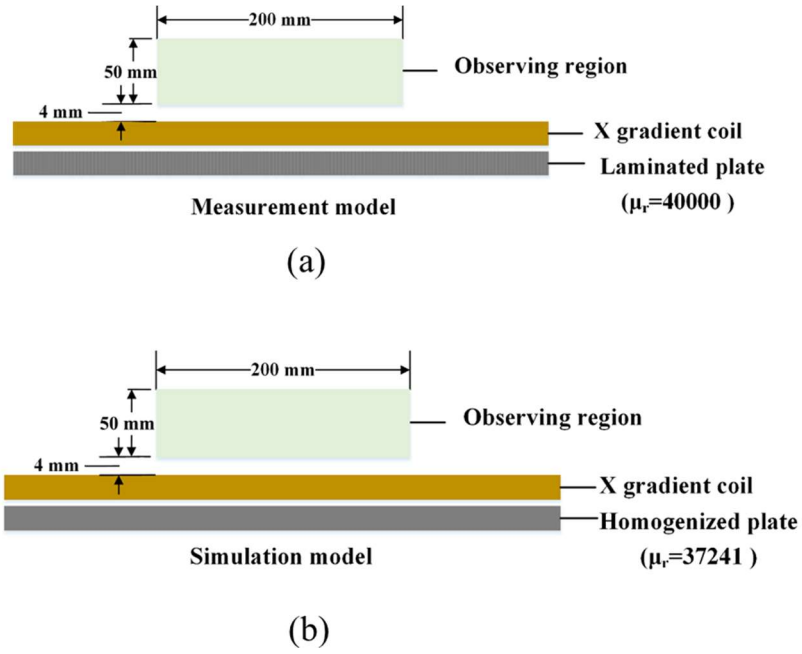

Fig. 2. 7 Model comparison between (a) measurement and (b) simulation models.

As shown in Fig. 2.8, B_z in the observed surface was compared and the measured magnetic field had a similar distribution to that of the simulation.

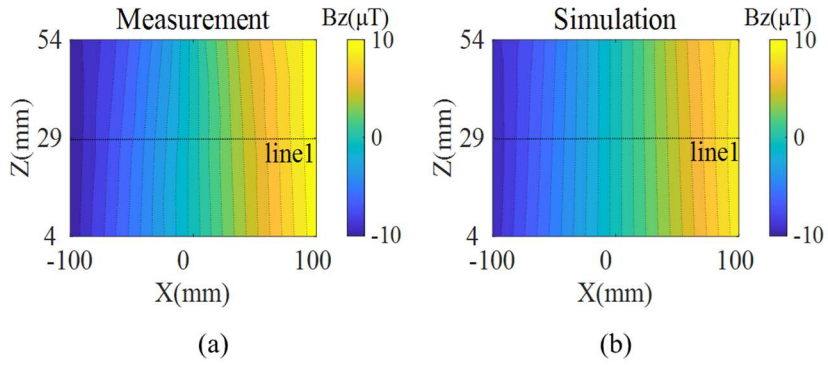

Fig. 2. 8 Magnetic field comparison between (a) measurement and (b) simulation results.

The normalized B_z of measurement and simulation, along with the absolute errors, are shown in Fig. 2.9. Overall, the measured and simulated magnetic fields have a good agreement. The absolute errors show a random distribution along the x-axis and are mainly caused by the errors in the real measurements. The majority of measurement points have an error less than 4%. This proved that the homogenized model is a good imitation for the original laminated model.

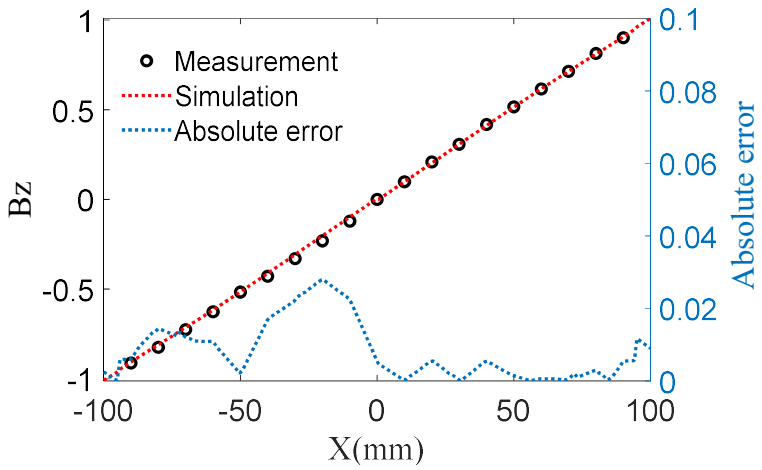

Fig. 2. 9 Magnetic field comparison between measurement and simulation along line 1 (normalized by the maximum Bz).

2.1.2 Model Simplification

In section 2.1.1, a homogenized model of the anti-eddy plate was established. Subsequently, the entire structure was evaluated. The permeability values were listed in Table 2.2.

Table 2. 2 Permeability of EM Structures

	Structure name	*Material type*	*Relative permeability*
1	Anti-eddy plate	Silicon steel sheets	37200
2	Shimming ring	Non-alloy quality steel	2000
3	Pole piece	Non-alloy quality steel	2000
4	Iron yoke	Stainless steel	1000
5	Permanent magnet	SmCo magnets	≈1

The relative permeability of the anti-eddy plate is higher than that of the other structures. Consequently, almost all the magnetic flux is confined in it. The complete magnetic structure can be simplified to a pair of homogenized plates, whose relative permeability equals that of anti-eddy plates $\mu_{\|r}$, and whose thickness and positions are same with those of the anti-eddy plates. Subsequently, the effects of the homogenized plates can be represented as image currents, based on the image current method [27], [28], as depicted in Fig. 2.10.

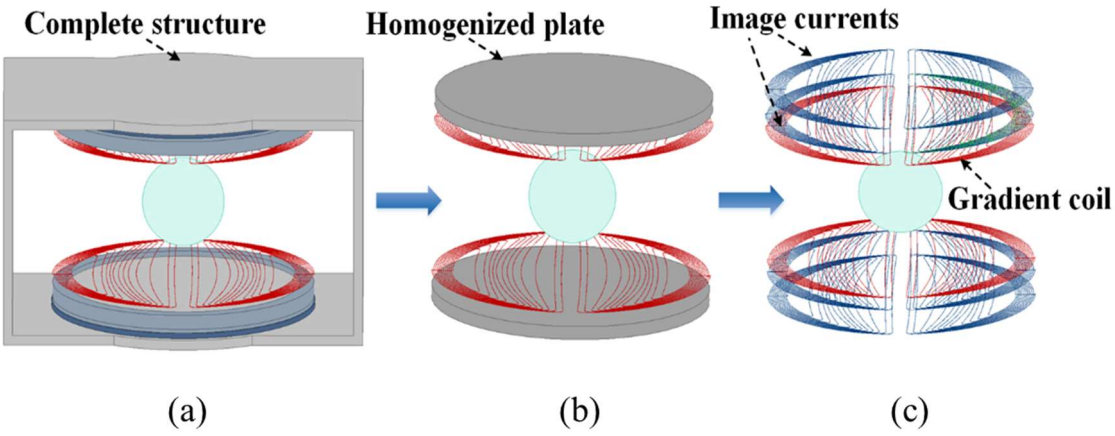

Fig. 2. 10 Simplification process: (a) complete, (b) simplified (parallel magnetic plates), and (c) image current models.

The first layer of the image current is located at a distance of $2z_0$ from the coil and carries a current of αI, where $\alpha = (\mu_{\parallel r} - 1)/(\mu_{\parallel r} + 1)$. The remaining image currents are located $2w$ apart and carry a current of $-\alpha^{i-3}(1-\alpha^2)I$. They are added to compensate for the error due to the finite thickness of the magnetic plate, where i is the number of layers, w is the thickness of the magnetic plate, and z_0 is the distance between the gradient coil and homogenized plate.

In conclusion, a simplified model for gradient coil design was defined, wherein the effects of the anti-eddy plates were represented as a pair of homogenized magnetic plates. These can be further presented as image currents. Based on this, a new gradient coil design method is described in chapter III.

2.2 Equivalent Image Magnetic Dipole Method

The proposed method is based on the conventional EMD method, which is summarized as follows: (i) the coil region is subdivided into Q small current loops (considered as magnetic dipoles); (ii) the loop currents, with width a and thickness h are determined such that the generated field matches the target field, and (iii) the coil path is obtained from the optimal current distribution. This procedure is schematically illustrated in Fig. 2.11.

The two-dimensional current field on the surface of the gradient coil region is represented by $\boldsymbol{J_s}$, which satisfies the following equation [23]:

$$\nabla \cdot \boldsymbol{J}_S = 0. \tag{2.6}$$

The stream function S[19] is defined to express $\boldsymbol{J_s}$ as follows:

$$\boldsymbol{J}_S = \nabla \times (S\boldsymbol{n}), \tag{2.7}$$

where $\boldsymbol{n}$ is a unit normal vector. The contour plot of S results in a winding pattern. The current density $\boldsymbol{J_s}$ is expressed by magnetization $\boldsymbol{M}$ of the magnetic dipole, as follows [23]:

$$\boldsymbol{J}_S = h\nabla \times \boldsymbol{M}. \tag{2.8}$$

where h represents the thickness of a single layer of the magnetic dipole. The relationship between S and $\boldsymbol{M}$ [22] is:

$$\boldsymbol{M} = \frac{S\boldsymbol{n}}{h}\ . \tag{2.9}$$

Moreover, $\boldsymbol{M}$ can be represented by the dipole moment as:

$$\boldsymbol{m} = \boldsymbol{M}a^2h = a^2S\boldsymbol{n}. \tag{2.10}$$

The magnetic flux density produced by the magnetic dipole is expressed by the following equation:

$$\boldsymbol{B}(\boldsymbol{r}) = -\frac{\mu_0}{4\pi}a^2S(\boldsymbol{r}_q)\nabla\frac{\boldsymbol{n}_q \cdot (\boldsymbol{r}-\boldsymbol{r}_q)}{|\boldsymbol{r}-\boldsymbol{r}_q|^3}\ , \tag{2.11}$$

where $\boldsymbol{r}$ is the position vector at the target point and the quantities relevant to the magnetic dipoles are indexed by q. The magnetic flux density in the target region is a superposition of the fields produced by all magnetic dipoles [22], that is:

$$\boldsymbol{B}(\boldsymbol{r}) = \frac{\mu_0 a^2}{4\pi}\sum_{q=1}^{Q}\boldsymbol{c}(\boldsymbol{r},\boldsymbol{r}_q)S(\boldsymbol{r}_q)\ , \tag{2.12}$$

where

$$\boldsymbol{c}(\boldsymbol{r},\boldsymbol{r}_q) = -\nabla \frac{\boldsymbol{n}_q \cdot (\boldsymbol{r}-\boldsymbol{r}_q)}{|\boldsymbol{r}-\boldsymbol{r}_q|^3}. \tag{2.13}$$

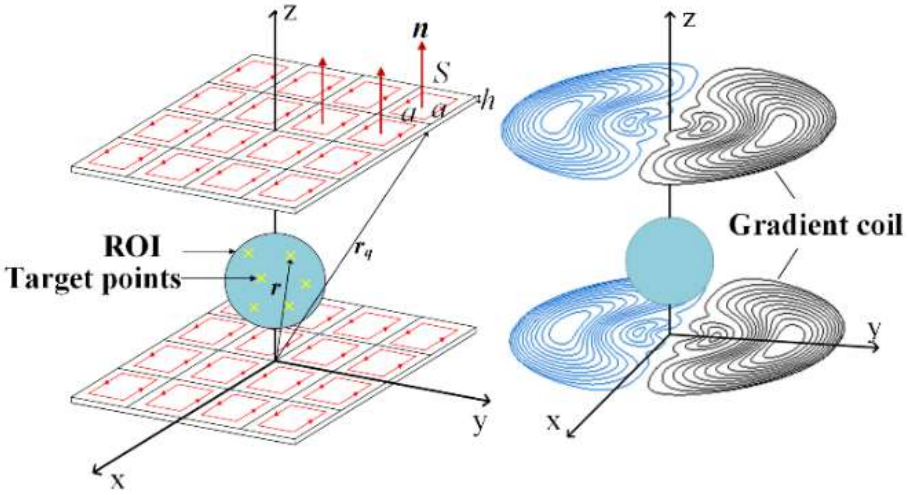

Fig. 2. 11 Schematic representation of EMD method.

As the loop currents in the gradient coil region are the only sources of the magnetic fields expressed in formulas (2.11) and (2.12), the conventional EMD method does not consider the influence of the magnetic material, as shown in Fig .2.11. To include this influence in the optimization model, the EIMD method was introduced.

According to the well-known image current method, the influence of the magnetic plate beneath the magnetic dipole can be represented as image current loops, as depicted in Fig.2.12, where we define the image current loops as equivalent image magnetic dipoles. To model the magnetic material, we place the first image magnetic dipole (represented using green solid lines) with equivalent current αI, where $\alpha = (\mu_{\|r} - 1)/(\mu_{\|r} + 1)$. To consider the finite thickness w of the magnetic plate, we place the image magnetic dipoles (represented using the green dotted line) with equivalent current, $-\alpha^{2i-3}(1-\alpha^2)I$ located $2w$ apart [27], [28]. When $\mu_{\|r}$ is sufficiently large, only the first image current must be considered. The magnetic moment located at the i-th layer is indicated by $\boldsymbol{m}_i$, where $\boldsymbol{m}_1$ has the same direction as that of $\boldsymbol{m}$, and others have the inverse direction.

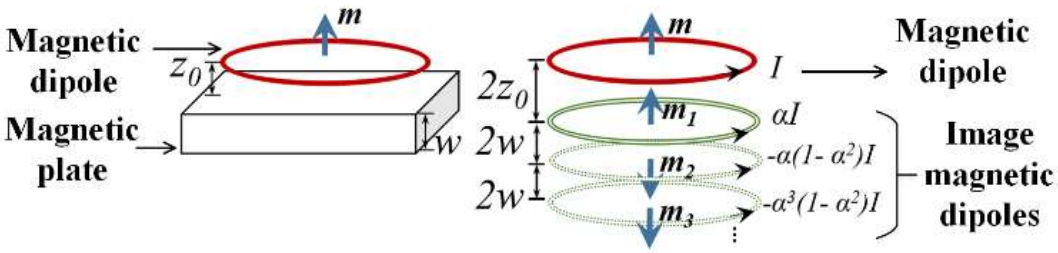

Fig. 2. 12 EIMD method.

Considering the image currents in the gradient coil design, the stream function S_i is introduced, corresponding to the *i*-th image current and defined by the following equation:

$$S_i = \begin{cases} \alpha S, i = 1 \\ -\alpha^{2i-3}(1-\alpha^2)S, \quad i = 2, 3, \ldots \end{cases} \tag{2.14}$$

Compared to the conventional EMD method depicted in Fig. 2.11, the effects of the magnetic plates are represented as image magnetic dipoles, in addition to the gradient coil, as depicted in Fig. 2.13.

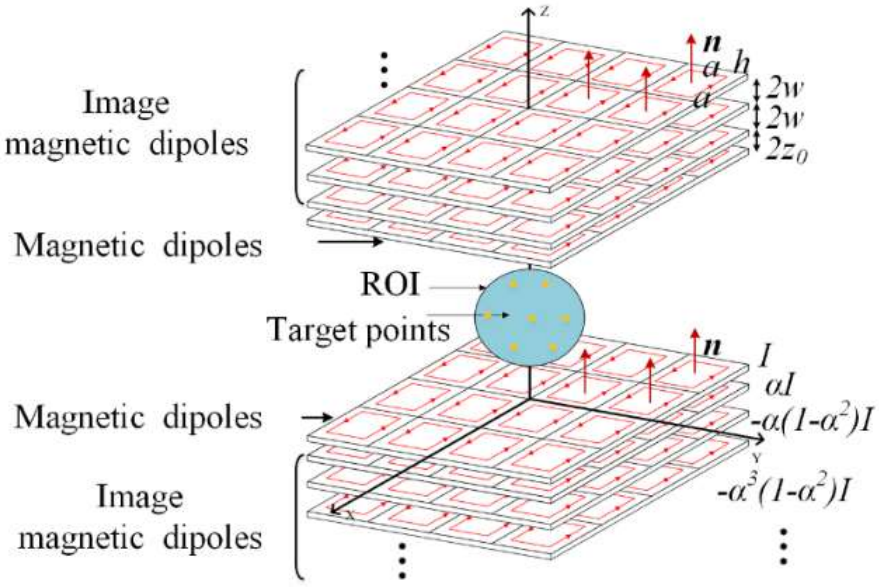

Fig. 2. 13 Schematic representation of the EIMD method.

The magnetic field in the target region is computed from the superposition of the fields produced by the current loops. At the target point ***r***, the magnetic flux density is expressed as:

$$\boldsymbol{B}(\boldsymbol{r}) = \frac{\mu_0 a^2}{4\pi}\left(\sum_{q=1}^{Q} \boldsymbol{c}(\boldsymbol{r}, \boldsymbol{r}_q) S_q(\boldsymbol{r}_q) + \sum_{i=1}^{L}\sum_{t=1}^{T} \boldsymbol{c}(\boldsymbol{r}, \boldsymbol{r}_{ti}) S_i(\boldsymbol{r}_{ti})\right), \tag{2.15}$$

where T and L denote the number of image magnetic dipoles for a single layer and the number of layers, respectively, and $\boldsymbol{r}_{ti}$ denotes the position vector of the t-th small loop on the i-th layer. The second term in formula (2.15) represents the influence of the magnetic plate.

The optimization problem is defined as:

$$F = \sum_{n=1}^{N} \left|\boldsymbol{B}_n - \boldsymbol{B}_{target}\right|^2 + \lambda W_M \rightarrow \min., \tag{2.16a}$$

$$W_M = \frac{1}{2}\int \boldsymbol{A} \cdot \boldsymbol{J}_s \, dV, \tag{2.16b}$$

$\boldsymbol{B}_{target}$ is the ideal X gradient field in the n-th target point, which can be expressed by

$$\boldsymbol{B}_{target} = x_n \boldsymbol{G}_x \tag{2.17}$$

where $\boldsymbol{G}_x$ is the required field gradient per meter in the x-direction, and x_n is the x-coordinate of n-th target point. W_M is the magnetic field energy of the current loops, λ is the regularization coefficient, and $\boldsymbol{A}$ is the vector magnetic potential relevant to the magnetic dipoles. When λ decreases, the magnetic field approaches the target field $\boldsymbol{B}_{target}$, whereas when it increases, the magnetic field energy decreases, thereby increasing the gradient switching speed. In formula (2.16), stream function S is the unknown function to be optimized. As presented in formula (2.7), the coil pattern can be obtained by drawing the contour line of S.

2.3 Design results

The X-gradient coil design process was considered as an example. The X-gradient coil generating the gradient field B_z with a linear spatial variation in the x-direction, was designed based on the proposed method. During the imaging process, the maximum gradient amplitude

exists in the slice-selection gradient. Based on the formulas from [56], the slice-selection gradient amplitude G_{slice} is determined by the RF pulse bandwidth Δf and the minimum excitation slice thickness Δz. Additionally, Δf is determined by the bandwidth product $T\Delta f$ and pulse width T. In our low-field MRI device, the time-bandwidth product (TBW) $\Delta f = 5$, the pulse width T=2 ms. Consequently, Δf is 2.5 kHz, Δz is 5 mm, and the maximum gradient amplitude should be larger than 11.74 mT/m. The efficiency is defined as the gradient amplitude generated by the unit current. Our gradient amplifier can provide up to a current of 60 A, thus, the objective of the design is to generate a field with an efficiency greater than 200 μT/(m·A). The non-linearity, defined as:

$$\delta = \left| \frac{\boldsymbol{B} - \boldsymbol{B}_{target}}{\boldsymbol{B}_{target}} \right| \times 100\%, \tag{2.18}$$

which should be less than 5% in a spherical ROI with a diameter of 200 mm. The X-gradient coil was wired on a circular plate with a radius of 300 mm. The distance between the pair of gradient coils was 320 mm. The relative permeability was set at 37200, and the thickness of the equivalent parallel magnetic plates was 10 mm (the same value as the thickness of the anti-eddy plate).

2.3.1 Determination of Image Magnetic Dipoles

Computing accuracy improves with an increase in the number of image layers L as well as the computation time. Consequently, L is determined based on the permeability and thickness of the magnetic plate. As the relative permeability of the magnetic plate is 37200 mm, one image layer would be sufficient to represent the real model because it has a relative error of less than 1%. When the relative permeability of the magnetic plates is lower, L must be increased.

2.3.2 Determination of Regularized Coefficient

The regularized coefficient λ is a key parameter that must be carefully determined by considering the design requirements for non-linearity and efficiency. The efficiency, non-linearity,

and inductance of the gradient coil as functions of λ are plotted, as seen in Fig. 14. There is a positive correlation between λ and efficiency as well as non-linearity and a negative correlation with the inductance. Moreover, the number of contour lines of stream function N_c, which equals the number of turns in the gradient coil, also influences those quantities; as N_c increases, the efficiency and inductance increase, and in contrast, the non-linearity decreases. Considering the design requirements for the efficiency and linearity, the regularized coefficient λ was chosen to be 10^{-20}, and the number of contour lines N_c was set to 40, with the possible smaller inductance value.

Q is the number of magnetic dipoles (current loops) in the gradient coil area, and T is the number of the image magnetic dipoles (image current loops) for a single image layer. T always holds the same value as Q. Fig. 2.14. (d) shows the dependence of nonlinearity and computation time on Q. With the increase of the Q, the non-linearity gradually stabilizes and the calculation time gradually increases. This indicates that a Q of 40 is sufficient for a design area with a diameter of 600 mm.

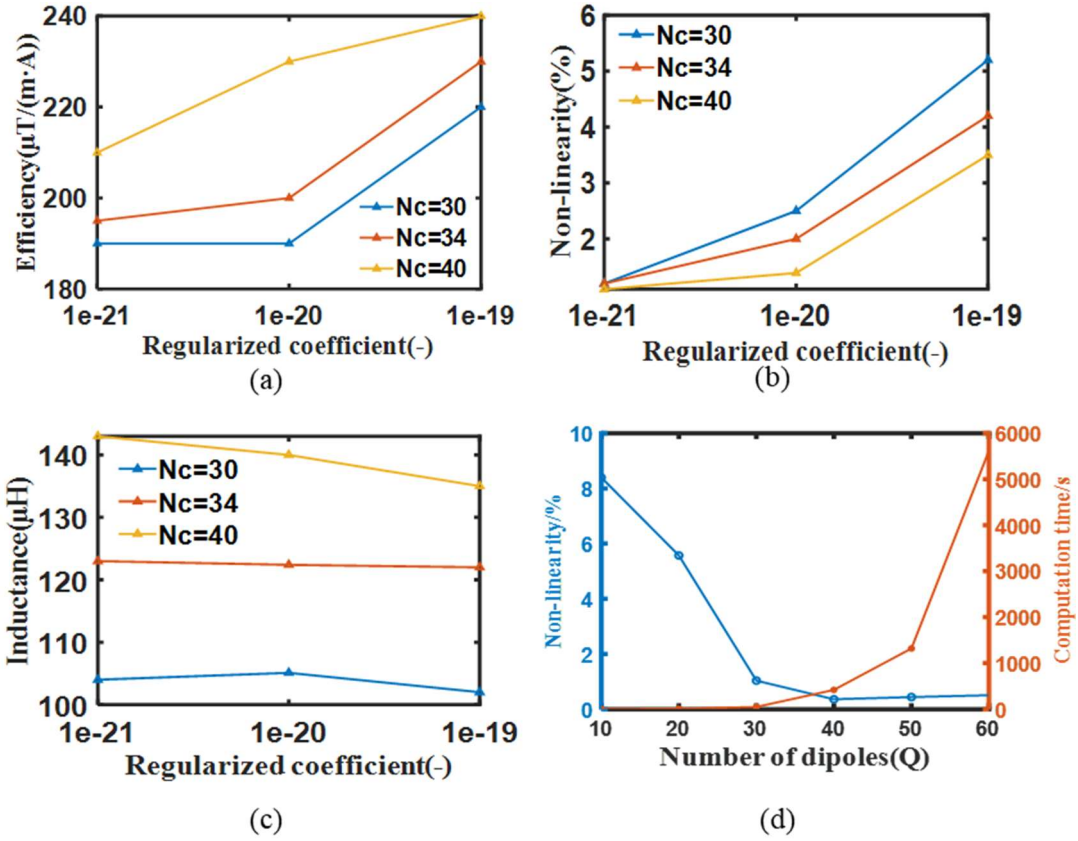

Fig. 2. 14 Dependence of (a) efficiency, (b) mean non-linearity, and (c) inductance on λ, and (d) dependence of nonlinearity and computation time on Q.

Figs. 2.15 (a) and (b) show the optimized profile of S and its coil pattern, respectively. Fig. 2.15 (c) shows B_z computed by the image method for the optimal design, which is sufficiently close to the fields shown in Figs. 2.15 (d) and (e), which are computed using simplified and full models. This indicates that other structures except the anti-eddy plate have negligible effects on the target field. In these three models, their maximum non-linearity of B_z is 3.2%, 3.3% and 3.3%, respectively, and their efficiency have the same value of 240 μT/(m·A). Their performances meet the design requirements [20].

To compare the proposed and conventional design methods, another X gradient coil was designed using the conventional method. The resulting optimal stream function and X gradient coil path are shown in Fig. 2.16 (a) and (b). It exhibits good linearity when no nearby magnetic

materials are present, as shown in Fig. 2.16 (c). The maximum non-linearity is 4.3%, however, when the gradient coil is placed in the complete model, the magnetic effects distort the gradient field in the target region, as shown in Fig. 2.16 (d), and the maximum non-linearity is greater than 10%. The comparison between Fig. 2.15 and Fig. 2.16 illustrates that the proposed method is well capable of taking into account the influence of ferromagnetic materials. Compared with the conventional method, the proposed method provides good linearity even under the effects of surrounding ferromagnetic materials.

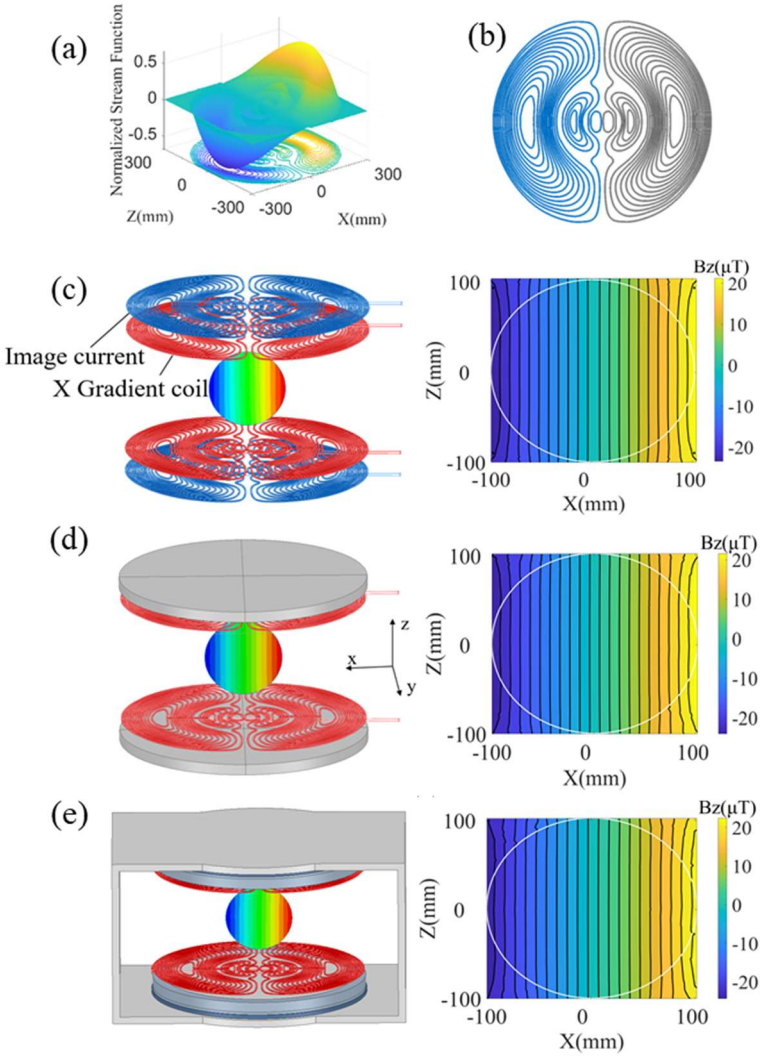

Fig. 2. 15 Design results of the proposed method. (a) and (b) are the optimal stream function and optimal X gradient coil path; (c) (d) and (e) are the simulation results of Bz in the

image current model, simplified model (parallel magnetic plates), and full model

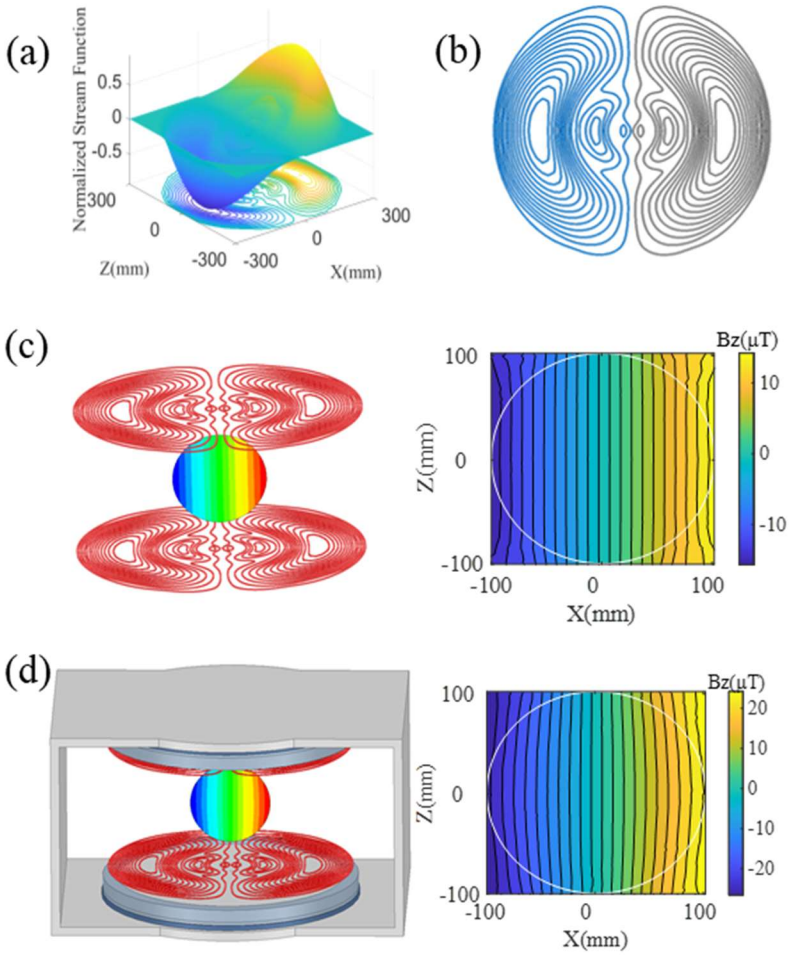

Fig. 2. 16 Design results of the conventional method. (a) and (b) are the optimal stream function and optimal X gradient coil path; (c) and (d) are the simulation results of Bz in the coil-only model and full model, respectively.

2.4 Experimental Verification

2.4.1 Gradient Coil Fabrication

A set of gradient coils were fabricated following the optimization results, as shown in Fig. 2.17. Regarding the actual winding of the gradient coil, a groove for the coil-winding trajectory was machined on an epoxy resin plate with a thickness of 4 mm and radius of 360 mm. A copper wire

was embedded in the groove to form a coil structure for the desired trajectory. The highest current required under normal operating conditions is 60 A. As 1 mm^2 of copper wire can carry a 10 A current and the required cross-section of the wire is 6 mm^2, two copper wires with a cross-section of 2 mm × 1.5 mm were used, which were in parallel winding for easy fabrication.

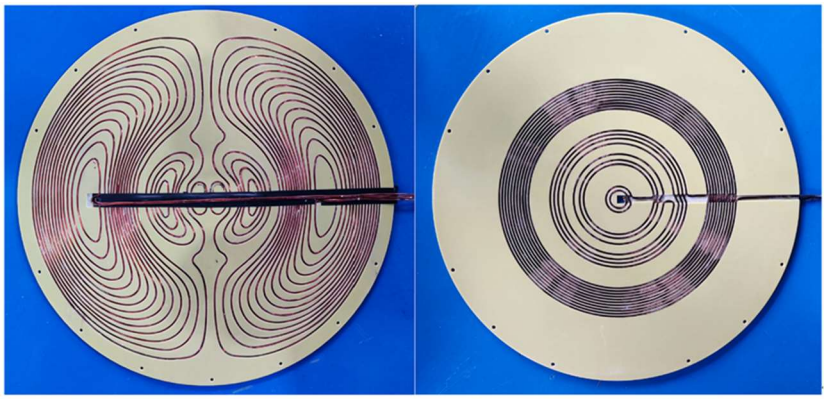

Fig. 2. 17 Real model of (a) X gradient coil and (b) Z gradient coil (the Y gradient coil has a similar pattern as that of the X gradient coil).

2.4.2 Gradient Field Measurement

The gradient coils were powered by a DC source (6233A, Agilent) with a current of 1 A. B_z in the ROI was measured using the platform depicted in Fig. 2.18. The field test device was controlled using a Metrolab Precision Nuclear Magnetic Resonance (NMR) Tesla meter (PT2026, resolution: 0.01 ppm in uniform 3 T field, accuracy: ± 5 ppm of field strength). Since there was a strong static magnetic field in the z-direction produced by the magnets, the gradient field was obtained by subtracting the static magnetic field from the total magnetic field.

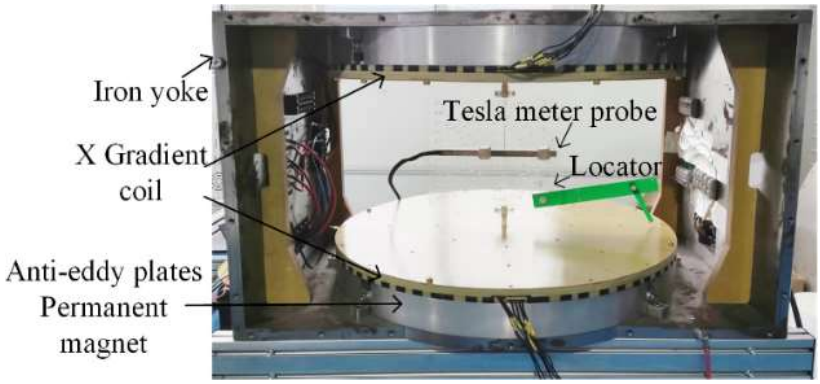

Fig. 2. 18 Magnetic field test platform.

The performance of the proposed method was compared to that of the conventional method. Figs. 2.19 (a) and (b) show the flux density on the spherical surface of the ROI. Figs. 2.19(c) and (d) show the distribution of B_z on the central surface of the ROI, where the dotted lines are the reference lines. Here, evident distortions in Figs. 1.9(b) and 2.19(d2) are noticed, caused by the magnetic effects of the anti-eddy plates. The distortions are corrected using the proposed method, as shown in Figs. 2.19(a) and (c). Figs. 2.19(e) and (f) show B_z on the central line of the ROI generated by the coils designed using the proposed and conventional methods. Here, the proposed method has smeller error with ideal gradient field, which means it improves the linearity. In the entire region of the ROI sphere, for the coils obtained using the proposed and conventional methods, the maximum non-linearity of the gradient coil and the efficiency are approximately 4.5%, 242 μT/(m·A) and 10%, 215 μT/(m·A), respectively.

The performance of the Z-gradient coil using measurements was evaluated. Similarly, the Z-gradient field in the ROI produced by the Z-gradient coil designed using the proposed and conventional method was compared. Unlike the X and Y gradient coils, the Z gradient coil had good linearity, even when it is designed using the conventional method. This is because of the symmetrical effects of the anti-eddy plates on the Z gradient field.

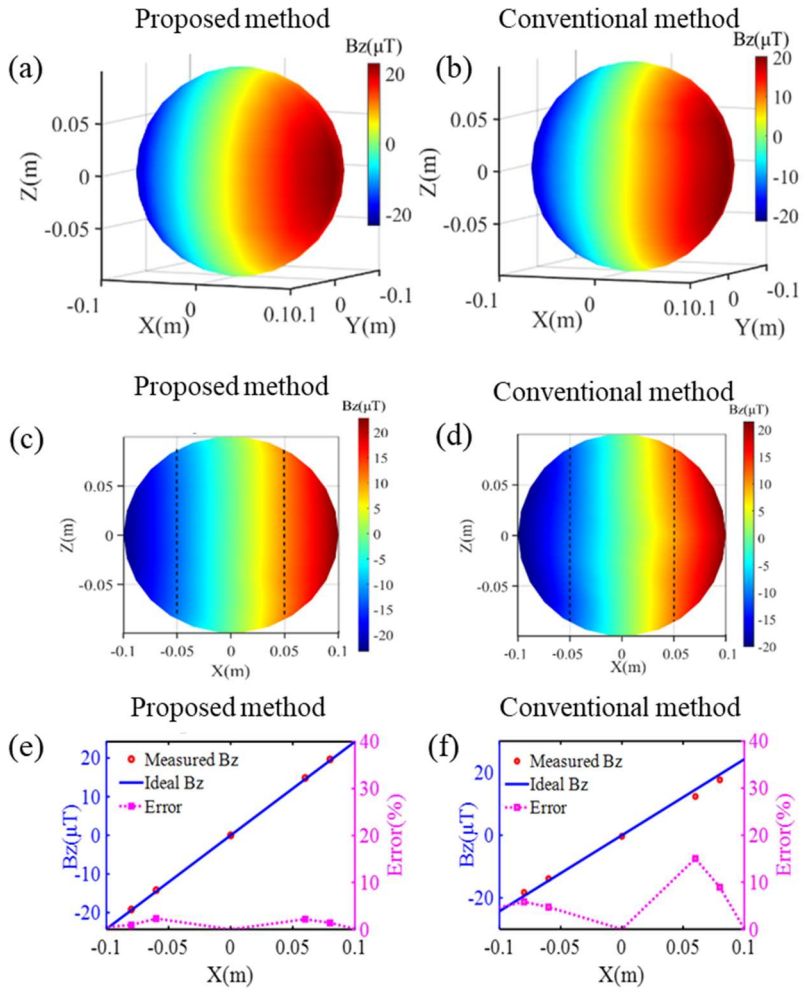

Fig. 2. 19 Comparison of the performances X gradients designed by the proposed method and conventional method. (a) and (b) show the distribution of Bz on the spherical surface of ROI; (c) and (d) show the distribution of Bz on the central surface of the ROI; (e) a

Figs. 2.20(a) and (b) show the flux density on the spherical surface of the ROI for the proposed and conventional methods, respectively. Figs. 2.20(c) and (d) show the distribution of B_z on the central surface of the ROI for the proposed and conventional methods, respectively, where the dotted lines represent the reference lines. Fig. 2.20(e) portrays B_z on the central line of the ROI generated by the coils designed using the proposed and conventional methods. From the above figures, both the proposed and conventional coils have good linearity. In the entire region of the ROI sphere, for the Z gradient coil designed using the proposed and conventional methods, the

maximum non-linearity and efficiency are approximately 3.2%, 274 μT/(m·A) and 4.7%, 244 μT/(m·A), respectively. The proposed and conventional methods do not reveal any considerable magnetic field distortion. Owing to the rotationally symmetrical effects of the anti-eddy plates on the Z gradient field, the Z gradient field is less vulnerable to the influence of ferromagnetic materials than the X and Y gradient fields.

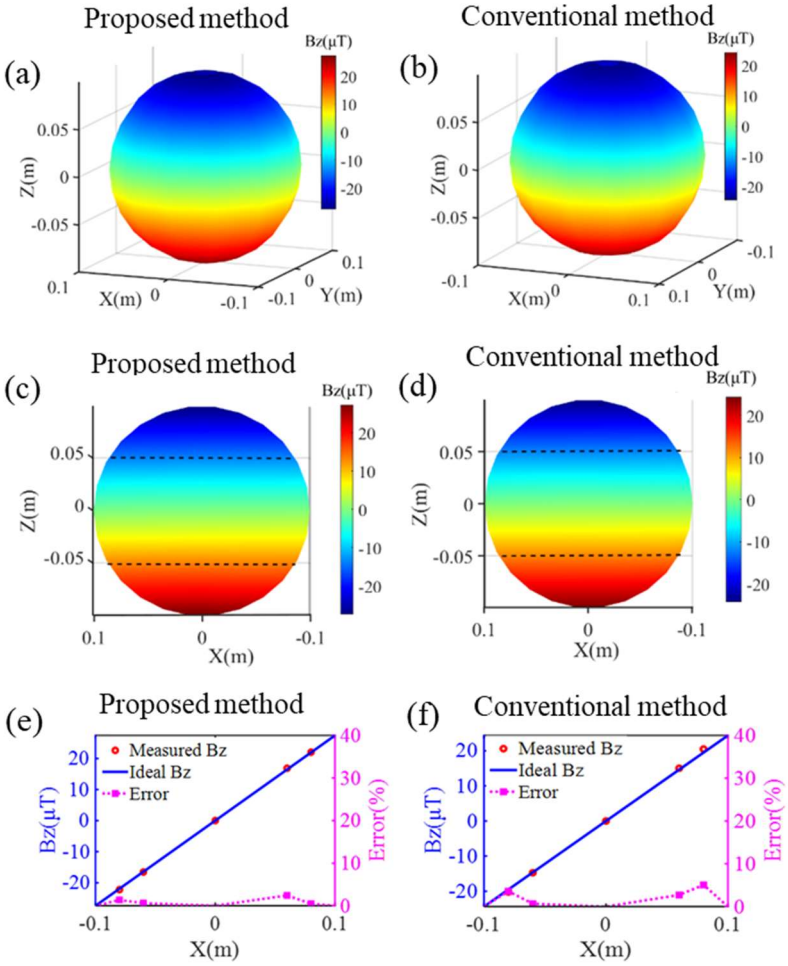

Fig. 2. 20 Comparison of the performances Z gradients deigned by the proposed method and conventional method. (a) and (b) show the distribution of Bz on the spherical surface of ROI; (c) and (d) show the distribution of Bz on the central surface of the ROI; (e) and (f) show B_z along the central line of ROI.

Table 2.3 lists the detailed parameters of the gradient coils designed using the proposed

method when the coils were installed in the devices. The experimental results reveal that the X- and Z-gradient coils designed using the proposed method produce gradient field with good linearity, even under the influence of nearby magnetic materials. Negligible distinctions are observed between the measurements and calculations owing to fabrication and measurement errors. Thus, the measurement results meet the design requirements. This indicates the validity and feasibility of the proposed method.

Table 2. 3 Measured Parameters of Gradient Coils by the Proposed Method

	X	*Y*	*Z*
Resistance (mΩ)	101.0	101.2	56.6
Inductance (μH)	141.3	141.5	87.5
Efficiency (μT/(m·A))	242	242	274
Average non-linearity (%)	2.3	2.2	1.6
Maximum non-linearity (%)	4.5	4.2	3.2

2.4.3 Imaging Results Comparison

The coils designed using the conventional and proposed methods were installed on similar low-field NMR equipment, and phantom imaging experiments were performed. The 50 mT low-field MRI device was placed on the shielding open area and the active denoising method [4] was utilized to reduce the environmental noise, as shown in Fig. 2.21. Phantom (CuSO4·5H2O, 1.95 g/L) and human brain images are shown in Fig. 2.22. With the gradient coils designed using the proposed method, image distortion was considerably reduced in the target area compared to that of the conventional method.

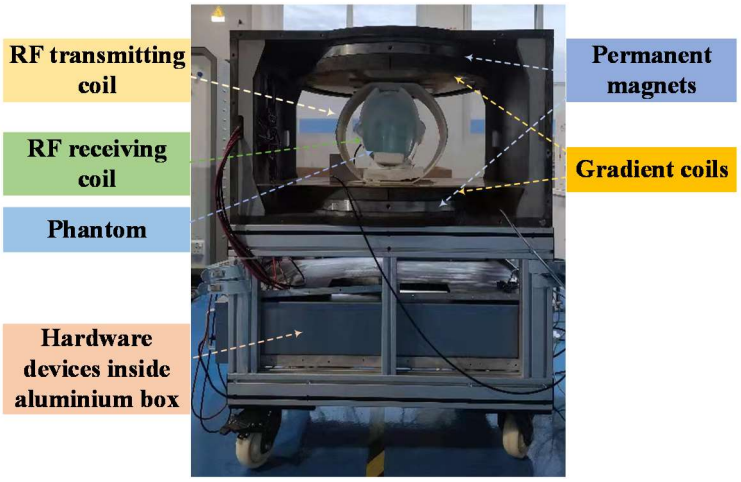

Fig. 2. 21 Unshielded 50 mT low-field MRI device.

In Fig. 2.22, 3D Gradient Recalled Echo (GRE) sequence was utilized for T1-weighted imaging. These images were acquired in 1 min 3 s, with a slice thickness of 10 mm. Number slices = 4, echo time [TE] = 21 ms, repetition time [TR] = 46 ms, number of averages = 1, resolution = 1.5 × 1.5 × 10 mm^3, and field of view: 250 mm × 250 mm.

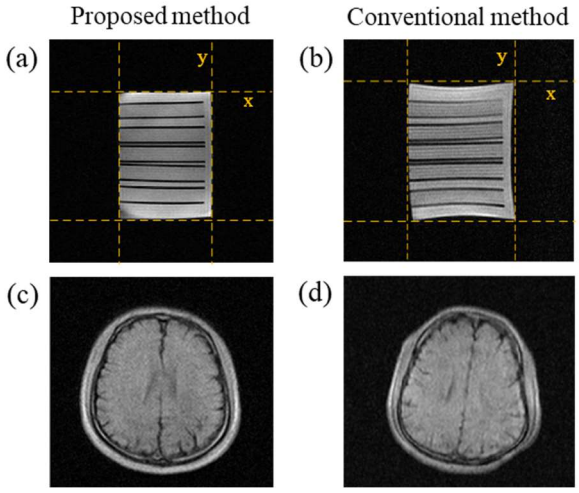

Fig. 2. 22 Imaging results comparison between the proposed method and the conventional method. (a) and (b) show the T1-weighted images in the x-y plane of the phantom (CuSO4·5H2O, 1.95 g/L) with cylindrical tubes. The yellow dotted lines are reference lines. (c) and (d) show the T1-weighted images in the x-z plane (transverse) of the human brain.

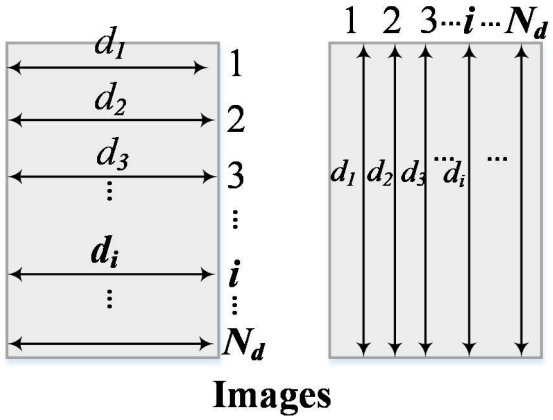

Fig. 2. 23 Schematic picture of the image distortion evaluation method.

To quantify the imaging distortion, the geometric distortion δ and aberration geometric distortion σ_δ [57] were evaluated as follows:

$$\delta = \left(1 - \frac{\bar{d}}{D}\right) * 100\%, \tag{2.19}$$

$$\sigma_\delta = \frac{1}{D}\sqrt{\frac{\sum_{i=1}^{Nd}\left(d_i - \bar{d}\right)^2}{N_d - 1}} * 100\%, \tag{2.20}$$

where N_d represents the number of measured lines, D is the real length of the test phantom, d_i is the measured length, and $\bar{d}$ is the mean value of the measured length, as shown in Fig. 2.23. Table 2.4 summarizes the geometric distortion and aberration geometric distortion in the *x*- and *y*-directions.

Table 2. 4 Distortion Evaluation

	δ (%) (x-direction)	δ (%) (y-direction)	σ_δ (%) (x-direction)	σ_δ (%) (y-direction)
Proposed	1.1	0.8	1.2	0.9
Conventional	4.3	4.7	5.0	5.8

For the conventional method, the geometric distortion δ in the x- and y-directions is more than 4% and the aberration geometric distortion is more than 5%. For the proposed method, the geometric distortion δ and aberration geometric distortion are both less than 1.2%, suggesting that the image distortion is effectively mitigated by the proposed design method.

2.5 Homogenization Method

2.5.1 Analytical Solution of Homogenized Permeability

This part describes the analytical method used for the homogenized model of laminated structures. The solenoid model is portrayed in Figs. 2.24 and 2.25.

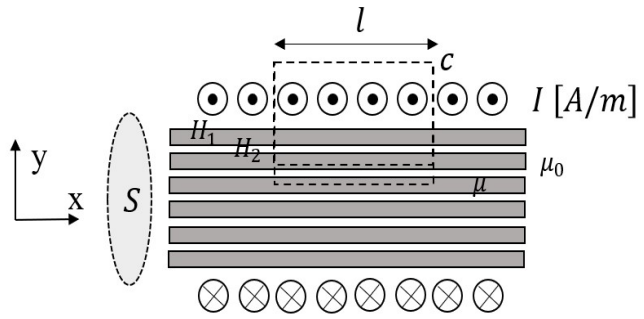

Fig. 2. 24 Solenoid model (Model A) used to calculate the homogenized permeability in the laminated direction.

As shown in Fig. 2.24, the laminated structure (gray) has a permeability of μ, which is inside the infinite-long solenoid, with each wire carrying a similar current I. On the solenoid, the

magnetic field is nearly homogeneous and parallel to the *x*-direction, whereas the field is negligibly small outside the solenoid. The magnetic fields in the steel sheet and air gap are denoted as H_1 and H_2. The filling rate (volume fraction) of the laminated structure is expressed as α and calculated as:

$$\alpha = \frac{t_{steel}}{t_{steel} + t_{gap}}. \tag{2.21}$$

Model A is used to calculate the homogenized permeability along the laminated direction (*x*-direction) $\mu_{\parallel}$. Applying Ampere's Law to a closed-loop *c* with length *l*, we obtained:

$$\oint_c \boldsymbol{H} \cdot d\boldsymbol{s} = lI. \tag{2.22}$$

We had:

$$lH_1 = lI, lH_2 = lI. \tag{2.23}$$

Evidently:

$$H_1 = I, H_2 = I. \tag{2.24}$$

The total magnetic flux along the *x*-direction inside the coil:

$$\begin{aligned} \Phi = SB &= S\{\alpha\mu H_1 + (1-\alpha)\mu_0 H_2\} \\ &= SI\{\alpha\mu + (1-\alpha)\mu_0\} \end{aligned}, \tag{2.25}$$

where *S* is the cross-sectional area of the solenoid. Assuming homogenized parallel permeability$\mu_{\parallel}$, the total flux is as follows:

$$\Phi = SB = \mu_{\parallel} SI. \tag{2.26}$$

From formulas (2.25) and (2.26), the homogenized permeability along the lamination direction $\mu_{\parallel}$ is represented as follows:

$$\mu_{\parallel} = \alpha\mu + (1-\alpha)\mu_0. \tag{2.27}$$

The homogenized relative permeability along the laminated direction is defined as $\mu_{\parallel r}$, which can be obtained from:

$$\mu_{\parallel r} = \frac{\mu_{\parallel}}{\mu_0}. \tag{2.28}$$

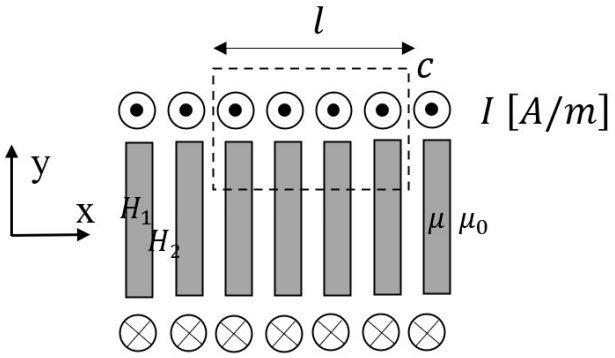

Fig. 2. 25 Solenoid model (Model B) used to calculate the homogenized permeability in the perpendicular direction.

Model B, as depicted in Fig. 2.25, is used to calculate the homogenized permeability in the perpendicular direction $\mu_{\perp}$. The following is derived from Ampere's law:

$$\alpha H_1 + (1-\alpha)H_2 = I. \tag{2.29}$$

Equation (2.30) is obtained as the magnetic flux density *B* inside the solenoid coil along the x-direction is constant:

$$B = \mu H_1 = \mu_0 H_2. \tag{2.30}$$

Combining formulas (2.29) and (2.30), the following is obtained:

$$\left(\frac{\alpha}{\mu} + \frac{1-\alpha}{\mu_0}\right) B = I. \tag{2.31}$$

The magnetic flux density *B* is represented as:

$$B = \frac{\mu\mu_0 I}{\alpha\mu_0 + (1-\alpha)\mu}. \tag{2.32}$$

When the homogenized material with permeability $\mu_{\perp}$ is considered, the magnetic flux density is:

$$B = \mu_{\perp} I. \tag{2.33}$$

From formulas (2.32) and (2.33), the homogenized permeability in the perpendicular direction $\mu_{\perp}$ is expressed as:

$$\mu_{\perp} = \frac{\mu\mu_0}{\alpha\mu_0 + (1-\alpha)\mu}. \tag{2.34}$$

Similarly, the relative permeability along the perpendicular direction is defined as $\mu_{\perp r}$, which is obtained from:

$$\mu_{\perp r} = \frac{\mu_{\perp}}{\mu_0} \tag{2.35}$$

2.5.2 Weight Reduction of the Anti-eddy Plate

The conventional structure of the anti-eddy plate was designed based on experience and incorporated a significant margin of safety. In other words, when achieving the same shielding effect, this structure possesses substantial potential for weight reduction. Therefore, we can increase the air gap between the laminated silicon steel sheets, effectively reducing the number of layers, to assess its influence on the shielding effect. The analytical method for the homogenized permeability of the anti-eddy plate is provided in the preceding section, enabling the fast assessment of the shielding effect using the simplified model. The accuracy of the simplified model has been validated earlier (Section 2.1.1), hence we have directly substituted the simplified eddy current shield model for the actual layered eddy current shield structure. As shown in the 1/8 model given in Fig. 2.26, the anti-eddy plate is modeled as a homogenized plate (Fig. 2.26 (a)), the model complexity is greatly reduced, compared with the real structure shown in Fig. 2.26 (b).

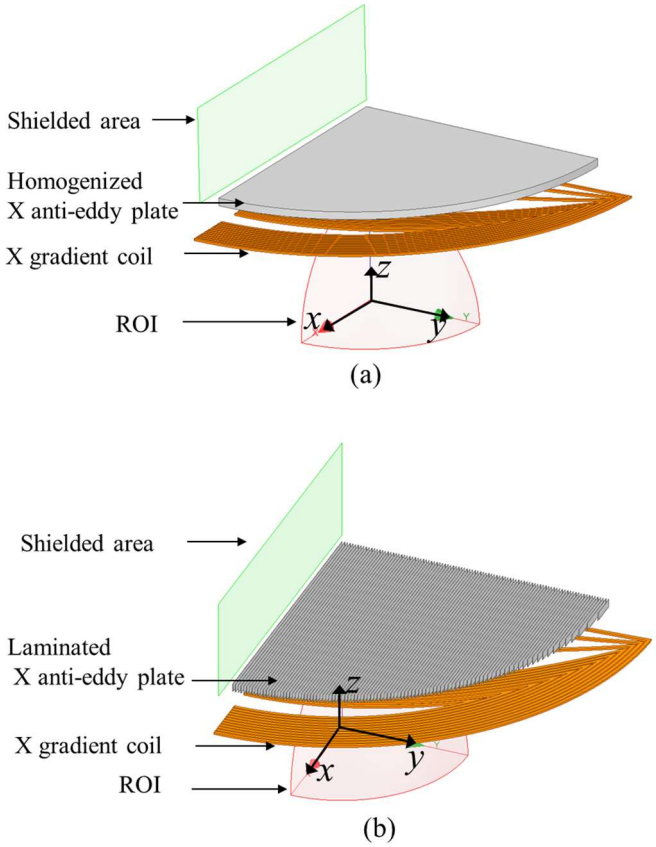

Fig. 2. 26 Assessment model for the shielding effect. (a) Simplified, and (b) real model.

The currently used anti-eddy plate is composed of silicon steel sheets with a thickness of 0.27 mm, separated by an air gap of 0.02 mm. According to the above analytical formula, its homogenized permeability is determined to be 37200. For the evaluation of the shielding effect, we utilize the simplified model depicted in Fig. 2.26 (a). In this model, the X-gradient coil is placed upon the X-eddy current shield. As compared to the scenario without the anti-eddy plate, the introduction of the shield alters the distribution of the gradient magnetic field, confining the gradient magnetic field almost entirely within it, thereby reducing the magnitude of the gradient magnetic field in the green region. The green region above the model represents the area where the magnet and other conductive structures exist; we refer to it as the shielded region. The magnitude of the gradient magnetic field within this region serves as an indicator of the eddy

current shield's shielding effect. We extract magnetic field values along a straight line and plot curves for different eddy current shield configurations for comparison, as shown in Fig. 2.27.

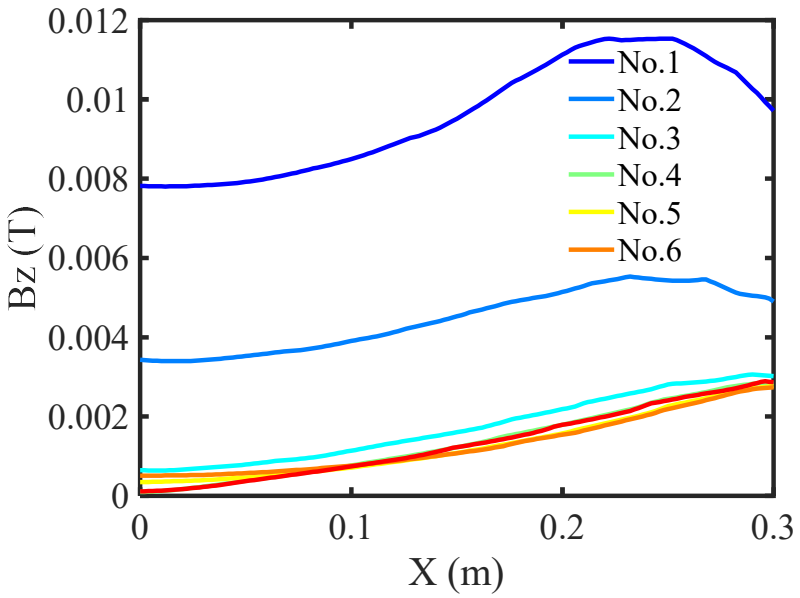

Fig. 2. 27 Field comparison in the shielded area, with anti-eddy plates in different homogenized permeability.

From Fig. 2.27, it can be observed that the shielding effectiveness of the anti-eddy plates improves as we move from No.1 to No.6. The coil of No.3 achieves the same shielding effect with the least amount of silicon steel sheets compared to the other plates. Therefore, it is recommended to adopt this structure. The structural parameters of the anti-eddy plates in Fig. 2.27 are given in Table 2.5.

The comparison between this new structure and the original structure is depicted in Fig. 2.28. The number of silicon steel sheets has been reduced from 917 to 98, resulting in a weight reduction of approximately one-tenth of the original weight. This provides an effective solution for reducing the equipment's weight.

Table 2. 5 Structural Parameters

No.	1	2	3	4	5	6
t_{air} (mm)	0.290	0.289	0.286	0.283	0.260	0.020
μ_r	1	100	500	1000	4000	37000

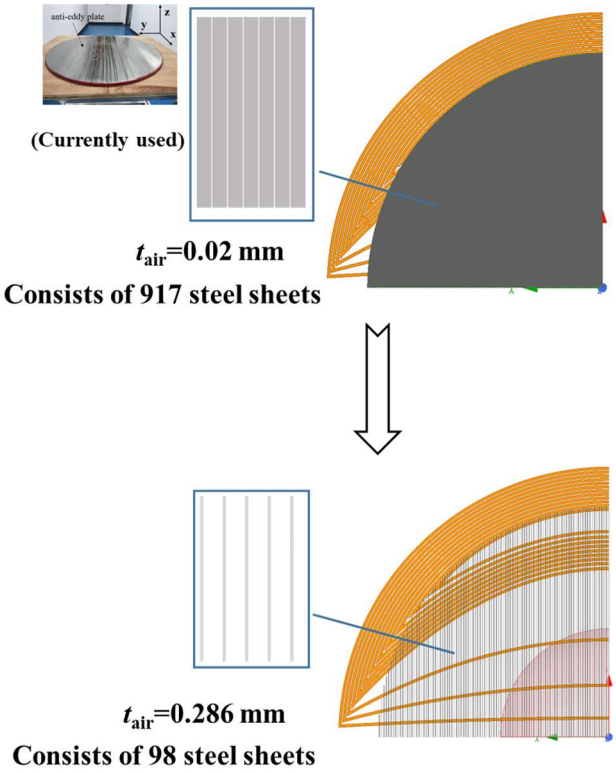

Fig. 2. 28 Structure comparison of anti-eddy plates (before and after weight reduction).

Chapter 3 Gradient Coil Design Considering Anti-eddy Performance

3.1 Model Simplification for Evaluation of Gradient Eddy Current

When the gradient magnetic field is rapidly switched on or off, there will be induced eddy current in the surrounding conducting materials. However, the overall 3-D model for FEM requires a high computing cost to evaluate the eddy current. The complexity of the FEM model should be reduced to shorten the calculation time. First of all, the anti-eddy plate laminated with silicon steel sheets can be simplified to a homogenized model, as illustrated in Chapter 2. The anti-eddy plate is with an overall thickness w of 8 mm, a material relative permeability of 40000, and a sheet thickness t_{steel} of 0.27 mm. The silicon steel sheets were separated by an air gap t_{air} of 0.02 mm. Because the air gap cuts off the eddy currents inside the anti-eddy plate, the magnetic field they produce has a negligible effect on the gradient field [58].

The process of simplifying the FEM model for evaluating eddy currents is depicted in Fig. 31. Initially, the 3-D FEM simulation model (1/8 model) is shown in Fig. 3.1(a), where the X-anti-eddy plate and Y-anti-eddy plate are installed vertically. To simplify the model, the iron yoke and permanent magnet are omitted in Fig. 3.1(b) because their contribution to eddy current losses is insignificant compared to the pole piece, as indicated in Table 3.1. Further simplification occurs in Fig. 3.1(c), where the X and Y anti-eddy plates are treated as a homogenized magnetic plate with a relative permeability of $\mu_{\parallel}$. This results in a 3-D symmetric model that can naturally be reduced to a 2-D axisymmetric model, as shown in Fig. 3.1(d). This highly simplified 2-D model is then used to assess the effects of eddy currents, significantly reducing the computational effort required. To demonstrate the advantages of this simplification, we provide the computation times

and mesh conditions for Model (a) and Model (d) in Table 3.2. These values were obtained while ensuring that both models achieve the same level of computational accuracy.

The eddy current losses in the surrounding structures are calculated using magnetic quasi-static analysis with a unit gradient current at a frequency of 2000 Hz. Table 3.1 presents the eddy current losses of four models in the pole piece and the entire structure (excluding the gradient coil). Based on the table, it is evident that the pole piece has the most significant impact on the eddy current loss. Therefore, the simplified model only includes the pole piece and a simplified anti-eddy plate to capture the essential effects of eddy currents.

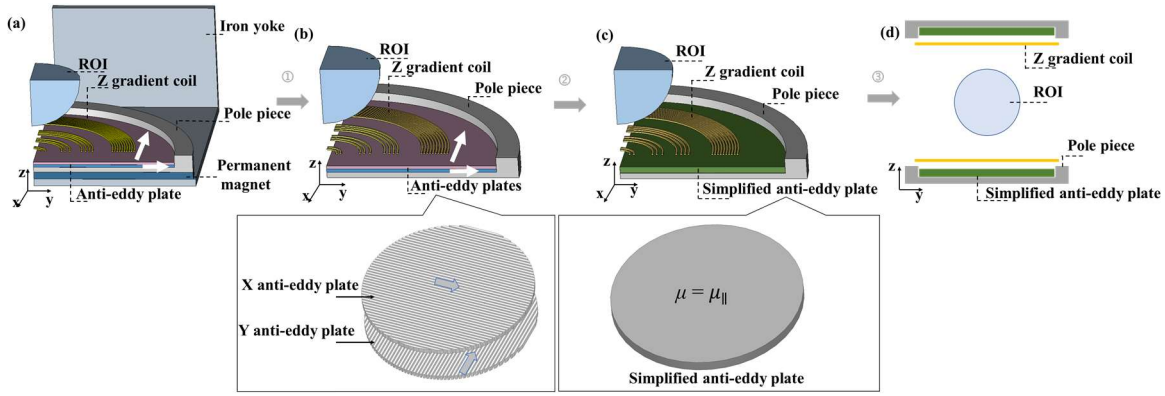

Fig. 3. 1 Simplification process of FEM simulation model. (a) Complete model. (b)Model without iron yoke and permanent magnet. (c) Model with simplified anti-eddy plate. (d) Axisymmetric 2-D model.

Table 3. 1 Eddy Current Loss In Four Models (Under Unit Current)

Models	*Eddy current loss in the pole piece* (mW)	*Total eddy current loss (Except gradient coil)* (mW)
(a)	6.10	6.19
(b)	6.11	6.11
(c)	6.10	6.10
(d)	6.09	6.09

Table 3. 2 Calculation Time Comparison

Model	*Number of mesh elements*	*Simulation Time*
Model (a)	1396000	3 hours
Model (d)	33400	2.5 mins

3.2 Z Gradient Coil Design Method Considering Gradient Eddy Current

We first give the definitions of nonlinearity and gradient efficiency. The nonlinearity of the Z-gradient coil in the i_{th} target point is defined as:

$$\delta_i = \left| \frac{B^i - B^i_{target}}{B^i_{target}} \right| \times 100\% \tag{3.1}$$

where B^i is the Z-component of the magnetic induction in the i_{th} target point, and B^i_{target} represents that for the perfectly linear gradient field. The maximum nonlinearity is generally an important index to evaluate the linearity of the gradient field, which is simply calculated by selecting the maximum value of δ_i in all the target points. The definition of the gradient efficiency of the Z-gradient coil is given by:

$$\eta = \frac{dB_z}{dz \cdot I}, \tag{3.2}$$

where I is the current flowing in the Z-gradient coil.

Fig. 3.2 outlines the design procedure for the Z-gradient coil. Initially, the 1-D image stream function (ISF) method is proposed to determine the coil pattern. This method considers parameters such as regularization coefficient, outer diameter and the number of coil turns, which collectively influence the coil's performance. Based on the approximated solution of MOP, a set of non-dominated points is obtained from the Pareto optimal front. These points represent combinations of coil parameters that achieve a trade-off between nonlinearity, gradient efficiency, and inductance. Subsequently, stricter performance constraints are applied to identify qualified non-dominated points. This step helps reduce the number of candidate solutions for further

evaluation. Finally, the anti-eddy performances of the qualified non-dominated points are evaluated using a 2-D asymmetrical FEM model presented in Fig. 3.1(d). By evaluating the anti-eddy performance, the coil with the best performance in suppressing eddy currents is selected as the optimal coil design.

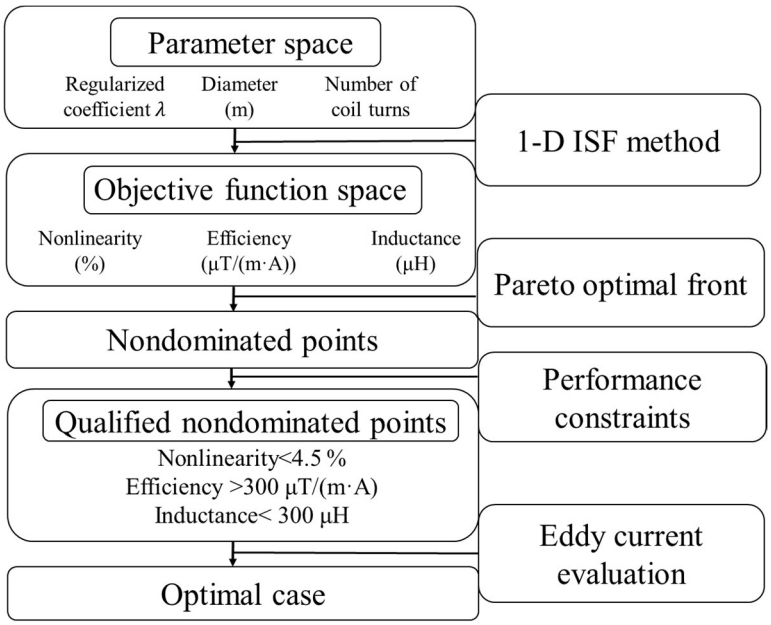

Fig. 3. 2 Flowchart of the Z-gradient coil optimization procedure.

3.2.1 1-D Image Stream Function (ISF) Method

The proposed 1-D image stream function (ISF) method has two main advantages. First, the rotationally symmetrical feature of Z-gradient coils can reduce the number of basic meshing units. As shown in Fig. 3.3(a), only the stream function values along the radius must be determined. Second, the effects of surrounding structures on the static gradient field are represented by image currents [23].

The following section describes the basic principles of the 1-D ISF method. Generally, there is a two-dimensional current field on the surface of the gradient coil region, which can be represented by $\boldsymbol{J}_s$ in a cylindrical coordinate system as follows:

$$\boldsymbol{J}_S = J_\emptyset \boldsymbol{e}_\emptyset + J_r \boldsymbol{e}_\boldsymbol{r}, \tag{3.3}$$

where $J_\emptyset$ and J_r indicate the azimuthal and radial components. $\boldsymbol{J_s}$ satisfies the following equation:

$$\nabla \cdot \boldsymbol{J}_\mathrm{S} = 0. \tag{3.4}$$

The stream function S[17] is defined to express $\boldsymbol{J_s}$ as follows:

$$\boldsymbol{J}_S = \nabla \times (S\boldsymbol{e_n}), \tag{3.5}$$

where $\boldsymbol{e_n}$denotes the unit normal vector. The spatial change in the value of S corresponds to an equivalent change in the current value, such that discrete wire positions carrying equal currents are directly given by contour plots of S. As for the Z-gradient coil composed of Maxwell pairs, only the azimuthal component $J_\emptyset$ exists, $\boldsymbol{J}_S = J_\emptyset \boldsymbol{e}_\emptyset$ **.** Hence, equation (3.5) can be reduced to

$$J_\emptyset = \frac{\partial S}{\partial r}. \tag{3.6}$$

When we assume a 1-D stream function along the radial direction, the contour positions represent discrete wires carrying equal currents along the azimuthal direction. Consider a narrow strip along the radial direction, as shown in Fig. 3.3(a). The strip meshes into N units with a width of d. Every unit has a discrete stream function value S_n (n=1…N) (Fig. 3.3(b)), which is an unknown parameter that needs to be optimized. All the current directions were along the azimuthal direction. After obtaining the optimal S_n, we fit the discrete stream function value to a smooth curve *S(x)* and then find the 1-D contour positions, as shown in Fig. 3.3(c), h is the contour interval. Corresponding to the 2-D gradient coil structure shown in Fig. 3.3(d), C_i represents the position of each turn of the coil in the radial direction, and the contour interval h determines the number of coil turns. The current direction in each turn is determined by the derivative values *d(S(x))/dx*. Positive derivative corresponds to a positive current, and correspondingly, a negative derivative represents for a negative current

Based on the simplified model given in Fig. 3.2(a), the image current [8, 23] loops are used to represent the effects of the magnetic plate. As shown in Fig. 3.4, L is the number of image layers, w is the thickness of the magnetic plate, and z_0 is the distance between the gradient coil and the magnetic plate. The first layer of the image current was located at a distance of $2z_0$ from the coil and carried a current of αI, where $\alpha = (\mu_{\parallel} - 1)/(\mu_{\parallel} + 1)$. The remaining image currents are 2 w apart, and the i-th image layer carries a current of $-\alpha^{i-3}(1-\alpha^2)I$. They were added to compensate for the error caused by the finite thickness of the magnetic plate. When $\mu_{\parallel}$ was sufficiently large, it was sufficient to consider only the first image current.

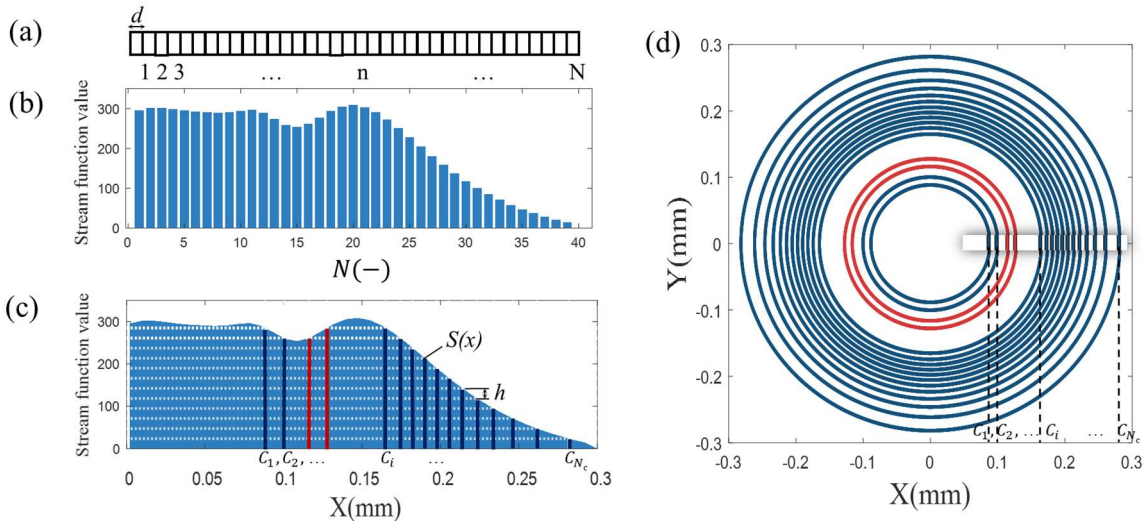

Fig. 3. 3 Z-gradient coil design process of 1-D ISF method.

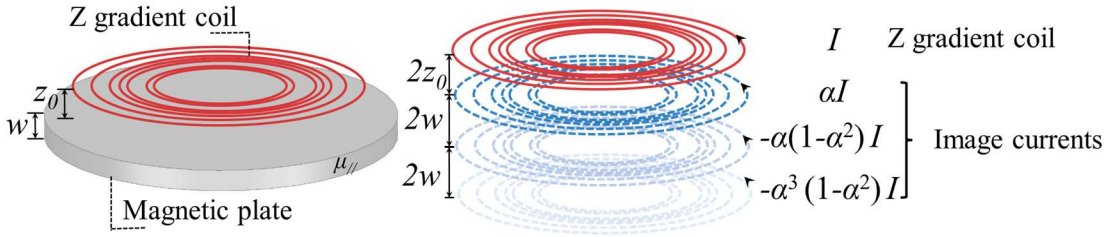

Fig. 3. 4 Image current method. Z-gradient coil over the magnetic plate(left), and equivalent image current loops that represent the effects of magnetic plate(right), where L is the number of image layers, and L=3 in this example.

On the target point (ρ, R, Z) in cylindrical coordinates, the z-component of the magnetic induction produced by the *n*-th gradient loop and its image loop of *i*-th layer are defined as ${B_Z}^n$and ${B_Z}^{ni}$. They can be obtained using the Biot–Savart law [24] as follows:

$$ {B_Z}^n = \frac{\mu_0 I_n}{2\pi\sqrt{Z^2 + (R+\rho)^2}}\left[K(k) - \frac{Z^2 - R^2 + \rho^2}{Z^2 + (R-\rho)^2}E(k)\right], \tag{3.7} $$

$$ {B_Z}^{ni} = \frac{\mu_0 I_{ni}}{2\pi\sqrt{Z^2 + (R+\rho)^2}}\left[K(k) - \frac{Z^2 - R^2 + \rho^2}{Z^2 + (R-\rho)^2}E(k)\right], \tag{3.8} $$

where *K*(*k*) and *E*(*k*) are the complete elliptic integrals of the first and second types, respectively.I_n is the discrete current value of the basic unit, and I_{ni} is the corresponding image current value, which has the following relations:

$$ I_{ni} = \begin{cases} \alpha I_n, i = 1 \\ -\alpha^{2i-3}(1-\alpha^2)I_n, i = 2, 3, \ldots \end{cases} \tag{3.9} $$

The discrete current density j_n (n=1…N) can be obtained from the difference in the stream function as follows:

$$ \begin{gathered} j_n = \frac{S_n - S_{n-1}}{w}, n = 1 \ldots N, \\ S_0 = 0, \end{gathered} \tag{3.10} $$

where *w* denotes the width of the basic unit. I_n is the integral of the current density over the unit width *w*

$$ \begin{gathered} I_n = j_n w, \\ I_n = S_n - S_{n-1}, n = 1 \ldots N, \end{gathered} \tag{3.11} $$

The magnetic field in the ROI is the superposition of the *N* basic unit loops and the corresponding *N***L* image loops, which are expressed as

$$ B_Z = \sum_{n=1}^{N}\left({B_Z}^n + \sum_{i=1}^{L}{B_Z}^{ni}\right), \tag{3.12} $$

where *L* is the total number of layers in the image loops. As the target points, select *K* points

distributed equally across the ROI. The target function is used to obtain the smallest deviation between the magnetic field at the target point B_{zk} and the ideal gradient field B_{zk_target}:

$$F = \sum_{k=1}^{K} \left| B_{zk} - B_{zk\_target} \right|^2 \rightarrow min., \tag{3.13}$$

where K is the number of target points. However, this formula results in over-fitted results, and a unique solution can be obtained using the Tikhonov regularization approach, given by

$$F = \sum_{k=1}^{K} \left| B_{zk} - B_{zk\_target} \right|^2 + \lambda W \rightarrow \min . \tag{3.14}$$

where W is the magnetic field energy of the current loops, λ is the regularization coefficient. As λ decreases, the magnetic field approaches the target field B_{target}, whereas when it increases, the magnetic field energy decreases, decreasing the inductance. The discrete stream function S_n is an unknown function to be optimized.

The magnetic-field energy is expressed as follows:

$$W = \frac{1}{2} \boldsymbol{J}^t \boldsymbol{M} \boldsymbol{J} \tag{3.15}$$

where $\boldsymbol{J}$ is the matrix of the discrete current density of basic units

$$\boldsymbol{J} = [j_1; j_2; \cdots j_n; \ldots j_N] \tag{3.16}$$

$\boldsymbol{M}$ is the mutual inductance matrix between every gradient loop, and the mutual inductance M_{ij} between the two loops is calculated as [25].

$$\boldsymbol{M} = \begin{bmatrix} \boldsymbol{L_{11}} & \cdots & \boldsymbol{M_{1n}} & \cdots & \boldsymbol{M_{1N}} \\ \vdots & \ddots & \vdots & \ddots & \vdots \\ \boldsymbol{M_{n1}} & \cdots & \boldsymbol{L_{nn}} & \cdots & \boldsymbol{M_{nN}} \\ \vdots & \ddots & \vdots & \ddots & \vdots \\ \boldsymbol{M_{N1}} & \cdots & \boldsymbol{M_{Nn}} & \cdots & \boldsymbol{L_{NN}} \end{bmatrix} \tag{3.17}$$

3.2.2 Pareto Dominance Principle

The MOP problem for the Z-gradient coil design has three objectives to be minimized:

$$Minimize\ f_m(\boldsymbol{X}), m = 1,2,3 \tag{3.18}$$

where $\boldsymbol{X}$= [x_1, x_2, x_3] is a vector of decision parameters: the regularization coefficient λ, outer diameter d, and the number of turns t, respectively. The cross combinations consist of the parameter space. Moreover, $\boldsymbol{F}$= [f_1, f_2, f_3] are three objective functions to be minimized: gradient nonlinearity, a derivative of efficiency, and inductance, respectively. Their cross-combinations comprise the objective function space. The judgement criteria for the non-dominated points are shown in Fig. 3.5.

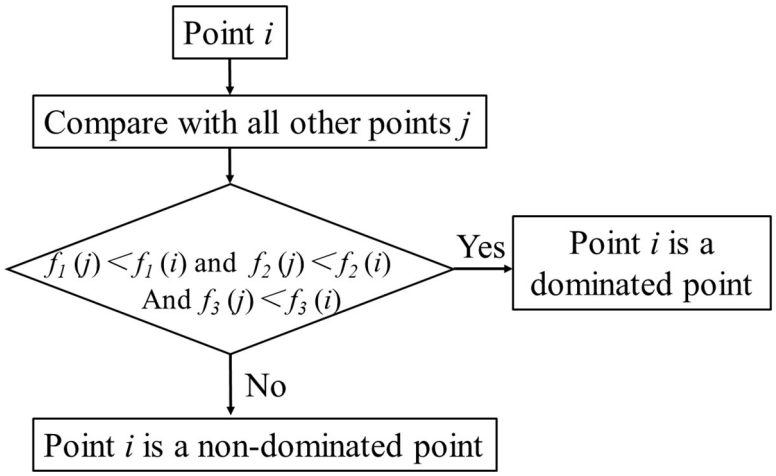

Fig. 3. 5 Judgement criteria of non-dominated solutions.

The non-dominated point has at least one aspect of performance that is better than the other points. The set of all non-dominated points is known as the Pareto front. The purpose of MOP is to find the Pareto front in the objective space. To narrow the range of optimal solutions, stricter constraints must be imposed to filter for better structures, after which qualified non-dominated points can be obtained.

3.2.3 Evaluation of Gradient Eddy Current

The generation of gradient eddy currents is related to the variations in the gradient magnetic fields within the sequences. During imaging process, the gradient magnetic fields are additional fields superimposed onto the main magnetic field to facilitate localization and spatial encoding. The changes in these gradient magnetic fields (*Gx*, *Gy* and *Gz*) are produced by different pulses within the imaging sequences, as shown in Fig. 3.6.

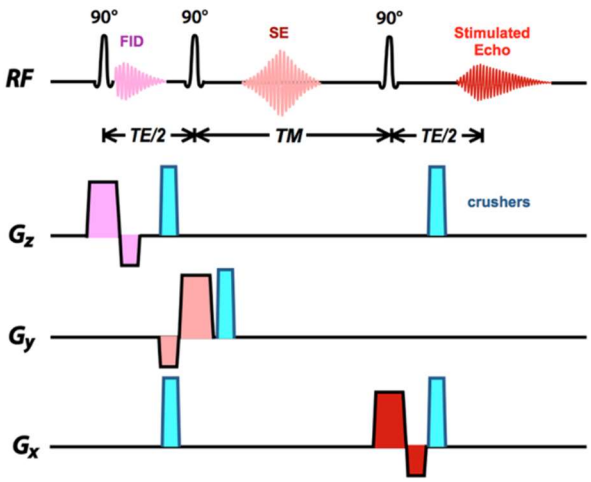

Fig. 3. 6 Sequence of MRI

The presence of gradient eddy currents alters the waveform of gradient pulses. Under the influence of eddy currents, the rising edge of the gradient magnetic field becomes slower, leading to decreased positional accuracy of the gradient magnetic field and resulting in artifacts in the image. To assess the impact of gradient eddy currents, it is necessary to calculate the response curve of the gradient magnetic field. We comprehend the impact of gradient eddy currents from the perspective of an equivalent circuit. The schematic in Fig. 3.7 illustrates the coupling relationship between the gradient coil circuit and the eddy current loop within conductive materials. The current and voltage within the gradient coil are denoted as $i(t)$ and $u(t)$, while the resistance and inductance are represented by R and L, respectively. On the right-hand side, L_1 and R_1 signify the inductance and resistance within the eddy current loop, where $i_1(t)$ represents the

eddy current in that loop. In practice, there isn't just a single eddy current loop; we begin with this simple circuit and extend the findings to scenarios involving multiple eddy current loops.

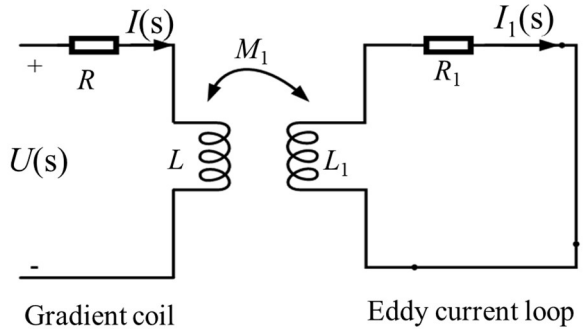

Fig. 3. 7 Simplified equivalent circuit of gradient eddy current.

From the Biot-Savart Law, the total magnetic field $G(s)$ produced by I and I_1:

$$G(s) = a\left(I(s) + \frac{a_1 M_1}{L_1}\frac{-sI(s)}{(R_1/L_1 + s)}\right), \tag{3.19}$$

then define $c_1 = a_1 M_1 / aL_1$ and $w_1 = R_1/L_1$, we have:

$$G(s) = a\left(1 + c_1\frac{-\mathrm{s}}{(w_1 + \mathrm{s})}\right)I(s). \tag{3.20}$$

To observe the effects of eddy current clearly, we assume there is a perfect step current in the gradient coil, the current is expressed as:

$$I(\mathrm{s}) = \frac{1}{s}. \tag{3.21}$$

The gradient field response is:

$$G(s) = a\left(1 + c_1\frac{-\mathrm{s}}{(w_1 + \mathrm{s})}\right)\frac{1}{s}. \tag{3.22}$$

The inverse Laplace transform of the above equation yields:

$$g(t) = a(1 - c_1 \mathrm{e}^{-w_1 t}), t \geq 0\ s\ . \tag{3.23}$$

Extend this formula to n eddy current loops as shown in Fig. 3.8 and we have:

$$g(t) = a\left(1 - \sum_{i=1}^{n} c_i\, \mathrm{e}^{-w_i t}\right), t \geq 0\ s. \tag{3.24}$$

where $c_i = a_i M_\mathrm{i} / aL_\mathrm{i}$ and $w_i = R_\mathrm{i}/L_\mathrm{i}$.

Under the influence of gradient eddy currents, the response of the gradient magnetic field is a summation of multiple exponential decay components. Each component's amplitude is denoted as c_i, and its time constant is represented by w_i.

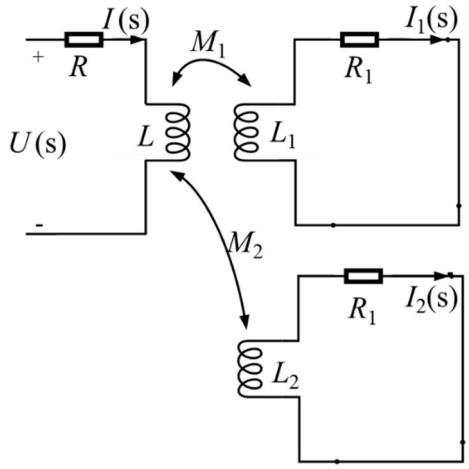

Fig. 3. 8 Equivalent circuit of gradient coil and eddy current loops.

From equation (3.24), the gradient field response is determined by R, L, R_i, L_i, M_i, a, and a_i, these parameters cannot be determined directly from analytical solution. The FEM calculation is necessary to evaluate the gradient eddy currents. Thus, a transient FEM simulation using the simplified 2-D model in Fig. 3.1(d) were performed to evaluate the eddy current effects.

To approximate the actual working situation, the gradient current has a delay time t_{delay} of 4.5 ms, slope width t_{slope} of 0.5 ms, and pulse width t_{pulse} of 30 ms, as shown in Fig. 3.9(a). The gradient field's eddy current losses and transient response after switching off the excitation will reflect eddy current effects.

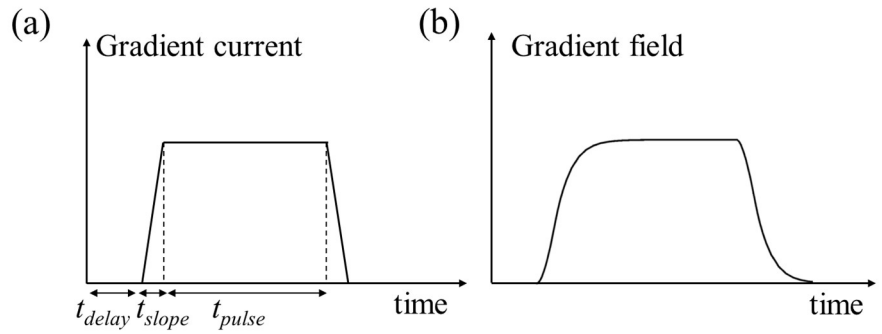

Fig. 3. 9 Simulation settings. (a) Gradient excitation current, and (b) corresponding gradient field transient response under the eddy current effects.

3.3 Design Results

The Z-gradient coil was mounted on a circular plate with a radius of 350 mm. The separation between the gradient coil pairs was 320 mm. The decision parameters for the multi-objective optimization (MOP) problem are shown in Fig. 3.10(a). These parameters were chosen equally along each axis. A filtering process was applied to eliminate impractical points, resulting in a total of 158 valid cases. Fig. 3.10(b) illustrates the corresponding objective function space, showing the results of the MOP problem for the selected cases.

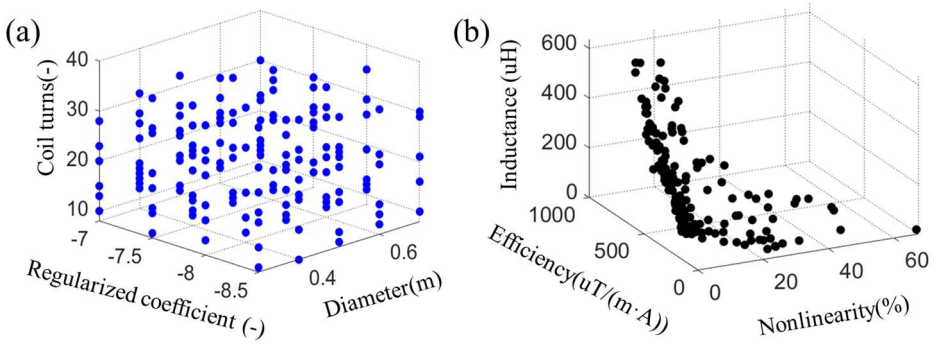

Fig. 3. 10 Parameter and objective function spaces for the MOP problem. (a) Parameter space. (b)Objective function space.

The Pareto front criterion was applied to the objective function space to obtain 84 non-dominated

points, represented by red points, as shown in Fig. 3.11(a).

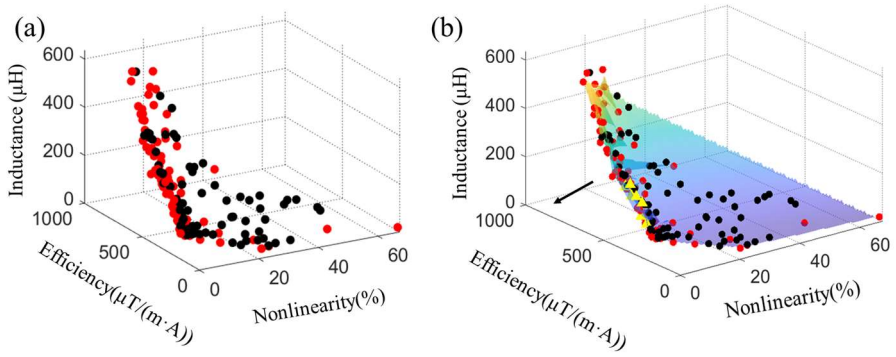

Fig. 3. 11 Objective function spaces. (a) Red points represent the non-dominated points, and black points are the dominated points. (b)Objective function space after adding restricted constraints, where qualified non-dominated points are yellow triangular points.

In Fig. 3.11(b), the Pareto front surface is drawn in the objective function space, and all red points representing the non-dominated points are located on this surface. The black arrows indicate the direction of the optimal solution. There were 86 non-dominated points. To filter them, we choose the points that meet the more restricted constraints by adding three constraints: nonlinearity <4.5%, gradient efficiency >300 μT/(m·A), and inductance <300 μH. The yellow triangular points represent qualified non-dominated points. There are nine qualified non-dominated points, and their structures are given in Fig. 3.12. Their objective function values and corresponding parameters are summarized in Table 3.3, in which *d,* λ, and *t* stand for outer diameter, regularization coefficient, and the number of turns, respectively.

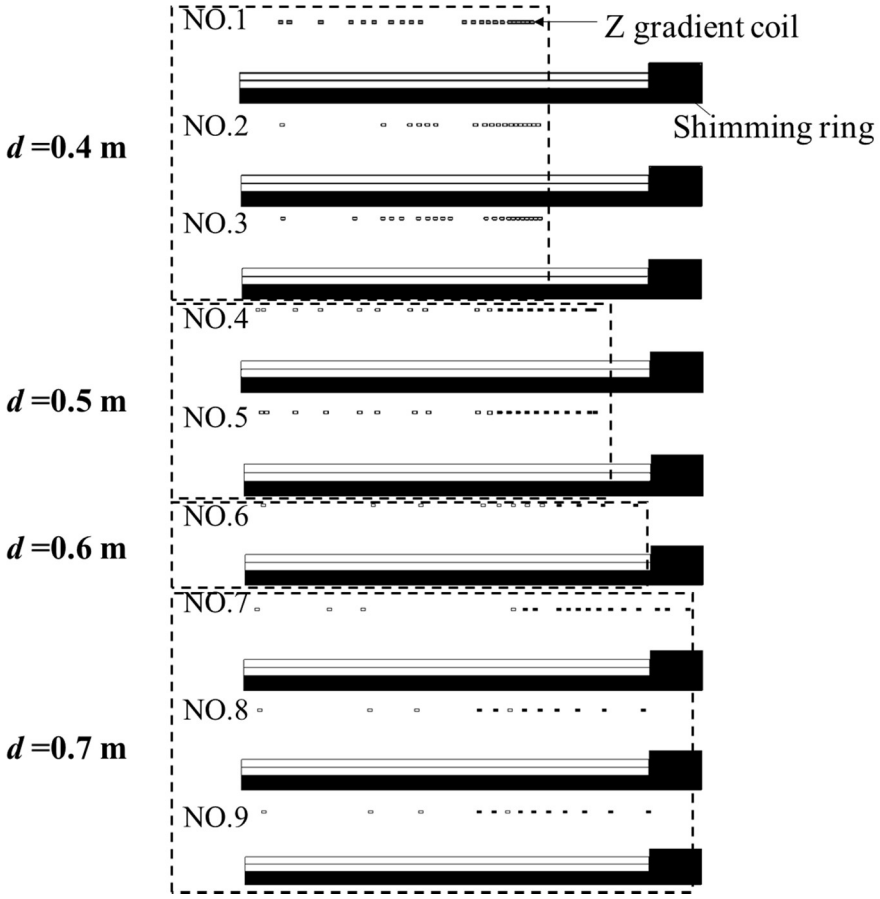

Fig. 3. 12 Structures of gradient coil

Table 3. 3 Qualified Non-dominated Cases

	d(m)	λ	*t*	*Nonlinearity* (%)	*Gradient efficiency* (μT/(m·A))	*Inductance* (μH)
No.1	0.40	-7.5	22	4.28	397	197.90
No.2	0.40	-8	19	3.80	310	168.00
No.3	0.40	-8.5	21	3.86	321	193.00
No.4	0.50	-8	20	4.50	405	194.20
No.5	0.50	-8	21	4.30	438	225.90
No.6	0.60	-8	12	4.50	305	109.00
No.7	0.70	-7.5	23	4.07	402	290.00
No.8	0.70	-8	12	4.50	304	107.60
No.9	0.70	-8	13	4.40	339	130.80

The coils in Table 3.3 are considered on equal footing in terms of MOP criteria, as no single coil performance surpasses the others in all three aspects. The anti-eddy performance of the nine coils will be then evaluated and used as the final evaluation factor. This ensures that we select the coil with the best anti-eddy performance while meeting the conventional performance requirements (Nonlinearity, gradient efficiency and inductance).

A 2-D simplified FEM model, depicted in Fig. 3.1(d), was utilized for anti-eddy performance evaluation. The gradient coils were subjected to a current excitation as depicted in Fig. 3.9(a). The time-dependent behavior of eddy current loss and eddy field response is illustrated in Fig. 3.13. The coil with shorter decay times demonstrates superior anti-eddy performance. We have shown from Table 3.3 and Fig. 3.14 that, although gradient efficiency and inductance are correlated with the anti-eddy performance, the outer diameter of the coil exhibits a more pronounced correlation with the anti-eddy performance. The No. 1, No. 2, No. 3 coils with diameters of 0.4 m have the least eddy current effects. Finally, coil No. 2 was chosen as the optimal coil, whose locations in the parameter and objective function spaces are shown in Fig. 3.14. In the parameter space, it has an outer diameter of 0.4 m, coil turns of 19, and a regularization coefficient of 10^{-8}. In the objective function space, it has a nonlinearity of 3.8%, gradient efficiency of 310 μT/(m·A), and inductance of 168 μH. The optimal coil pattern is depicted in Fig. 3.15(a), and the simulated gradient field B_z in the ROI from the full model is shown in Fig. 3.15(b). The radial positions and current directions of the optimal coil are given in Table 3.4.

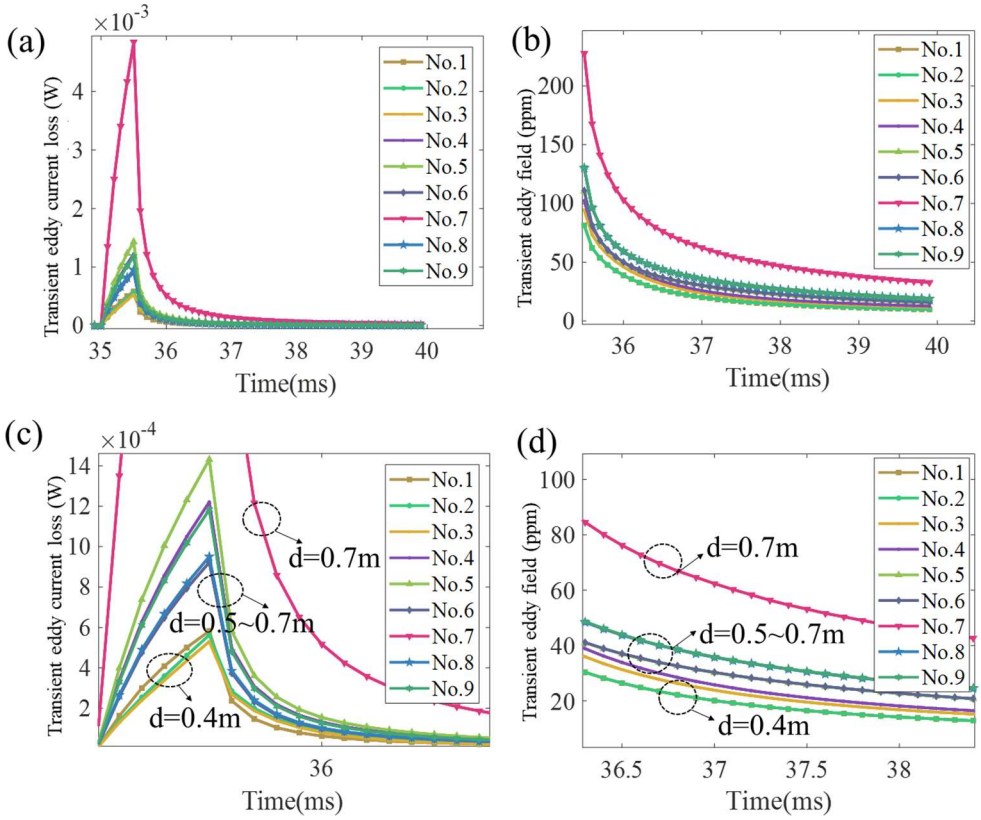

Fig. 3. 13 Eddy current losses and field responses. (a) Eddy current losses and (b)Gradient field transient response of the nine coils with different outer diameters d varies from 0.4m~0.7m；(c) and (d) are enlarged versions of (a) and (b). The vertical axis Gz rep resents the magnetic induction, its unit (ppm) means the value of parts per million of the original field.

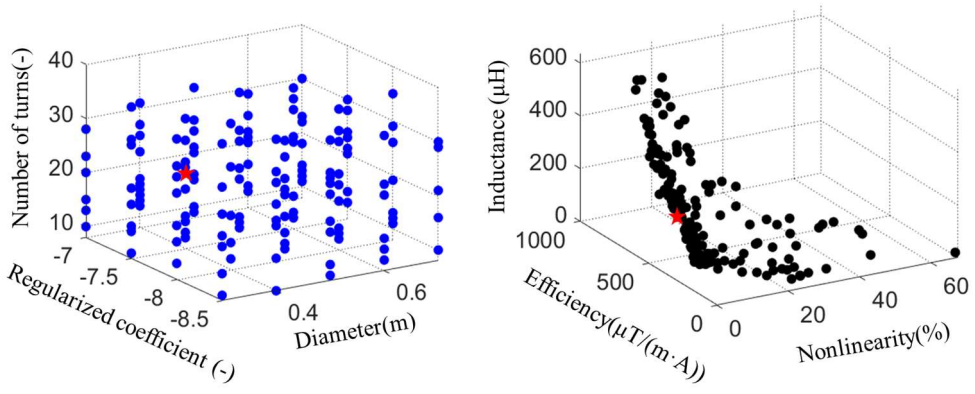

Fig. 3. 14 Locations of optimal coil in (a)Parameter space and (b)objective function space, the optimum coil is marked by red.

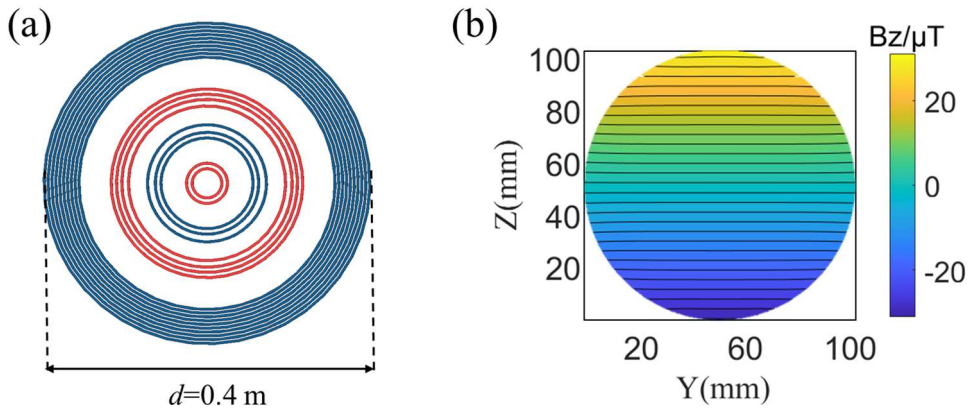

Fig. 3. 15 Optimal coil and corresponding field distribution in ROI (a) Optimal coil pattern. (b) Simulated field from the full model.

Table 3. 4 Parameters of the Designed Gradient Coil

Turn No.	1	2	3	4	5	6	7	8	9	10
Current Direction	-	-	+	+	+	-	-	-	-	+
Radial Position (mm)	15	22	60	67	77	95	103	110	116	152
Turn No.	11	12	13	14	15	16	17	18	19	20
Current Direction	+	+	+	+	+	+	+	+	+	+
Radial Position (mm)	157	162	167	172	176	181	186	191	196	200

3.4 Experimental Validation

The optimal coil designed by the proposed and conventional coil (without consideration of the anti-eddy performance) were fabricated, as shown in Fig. 3.16. Here we define the conventional method as any other method without considering anti-eddy performance. The conventional coil shown in Fig. 3.16(b) was designed from the particle swarm algorithm, and the optimization objectives include only the coil nonlinearity, gradient efficiency, and inductance value.

The static magnetic field was tested in the 50 mT low-field MRI device, and the gradient

coil was powered by a DC current source (SPD3303X, Siglent). The field test device used was a Metrolab Precision NMR Tesla meter (PT2026, resolution: 0.01 ppm, accuracy: ± 5 ppm). The field test platform is shown in Fig. 3.17. There was a strong static magnetic field in the z-direction produced by the permanent magnets, the gradient field was obtained by subtracting the static magnetic field from the total magnetic field.

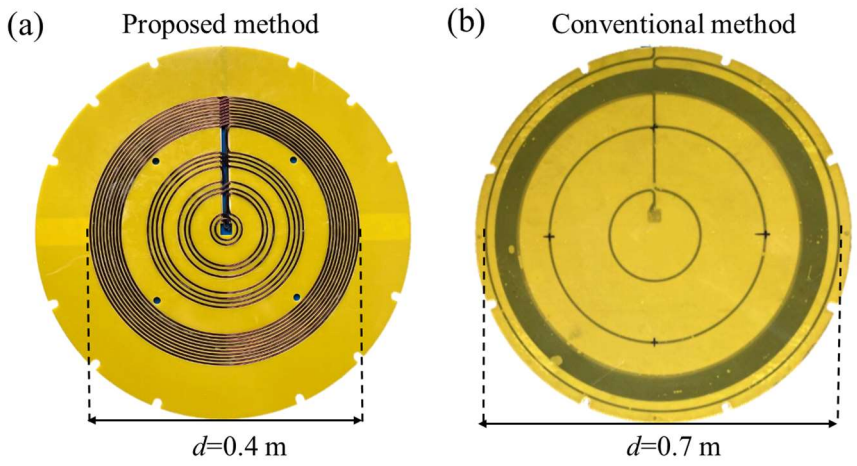

Fig. 3. 16 Fabricated gradient coils. (a)Optimal coil by the proposed method, outer diameter=0.4 m and (b) Coil by the conventional method, diameter=0.7 m.

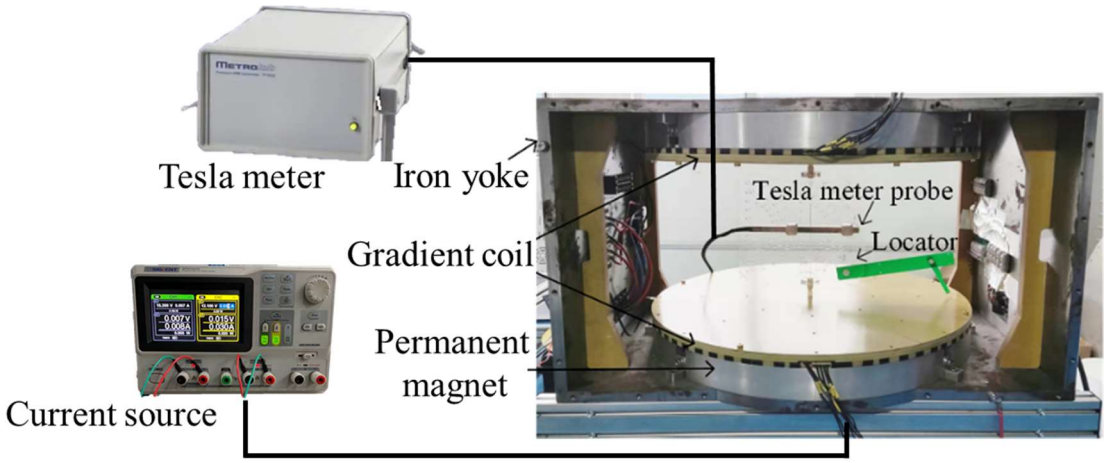

Fig. 3. 17 Field measurement platform inside the low-field MRI device (50 mT).

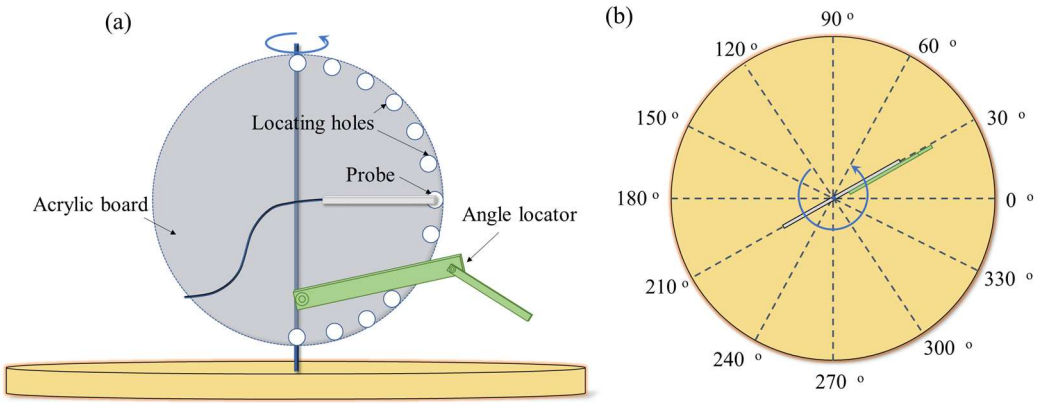

Fig. 3. 18 Schematic diagram of locator for probe positioning. (a) Front view, and (b) side view.

Fig. 3.18 shows the schematic diagram for the locator in Fig. 3.17. The probe can be embedded into the locating holes distributed around the circumference, and the acrylic plate can be rotated from 0 to 360 degrees. When the angle locator is positioned at the angle to be measured (for example, 30° in Fig. 3.18(b)), the probe measures the magnetic field value once in each locating hole. Target points on the surface of the ROI, as shown in Fig. 3.19(a), can be measured sequentially. Only the surface points are measured because the most severe field distortions are always on the surface. The magnetic induction (B_z) was measured at the target points shown in Fig. 3.19(a), and the comparison of the performance of the proposed coil and the conventional coil is shown in Table 3.5.

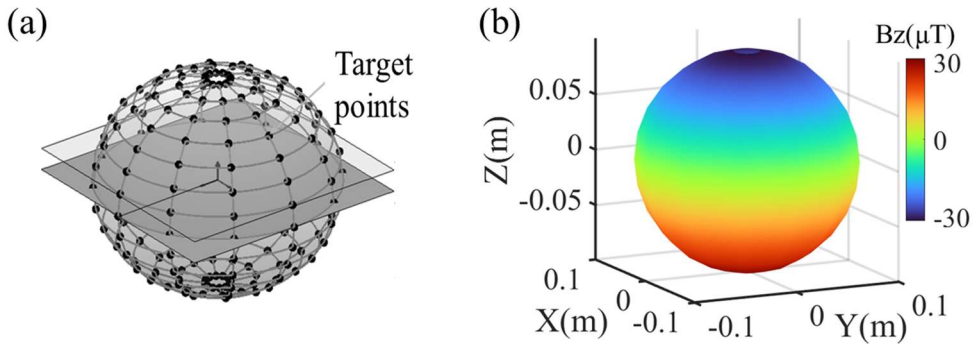

Fig. 3. 19 Measurement points and results. (a) Measured target points, and (b) measured gradient field from the proposed method.

Table 3. 5 Performance Comparison of the Proposed and Conventional Coil

	d(m)	*Nonlinearity* (%)	*Gradient efficiency* (μT/(m·A))	*Inductance* (μH)
Proposed	0.40	4.20	314	170
Conventional	0.70	3.50	272	210

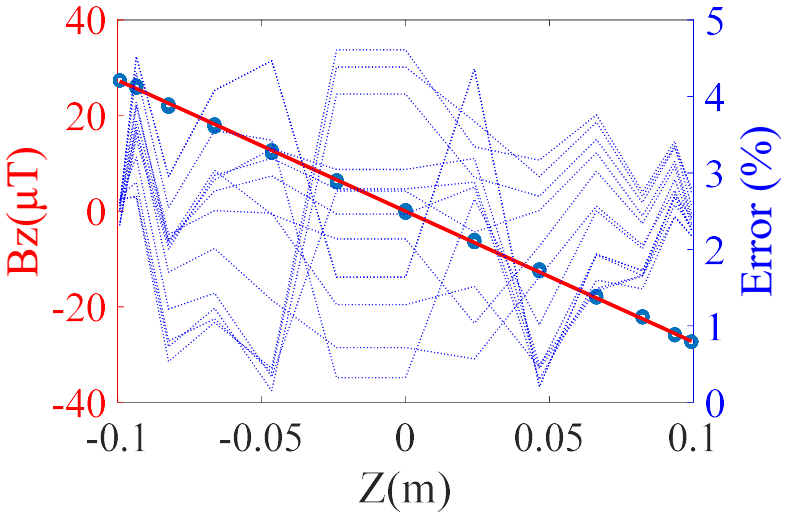

Fig. 3. 20 Field in target points and relative errors.

Fig. 3.20 is given to show the measured gradient field at each target point. In Fig. 3.20, the hollow dots represent the magnetic field of the target points, and the red line represents the ideal gradient field. The field error with the ideal field represents the nonlinearity, as shown by the blue dotted line in Fig. 3.20. The maximum nonlinearity is less than 5%, which meets the design requirement well.

To show the effectiveness of the proposed method, a comparison was made between the gradient eddy effects of two coils shown in Fig. 3.16. The magnitudes of the eddy currents were estimated at various delay times after the test gradient pulse, allowing for the evaluation of anti-eddy performance in the experiment [9]. The testing results, as depicted in Fig. 3.21, demonstrate that the Z-gradient coil designed using the proposed method exhibited a faster field response

compared to the conventional coil. This indicates that the proposed method effectively reduces the eddy current effects. The reduction in eddy current effects can primarily be attributed to the smaller diameter employed in the proposed method (0.4 m compared to 0.7 m in the conventional coil). Based on these findings, it can be concluded that the outer diameter of the coil primarily influences the eddy current effects. Therefore, in order to minimize such effects, it is advisable to use smaller coil diameters.

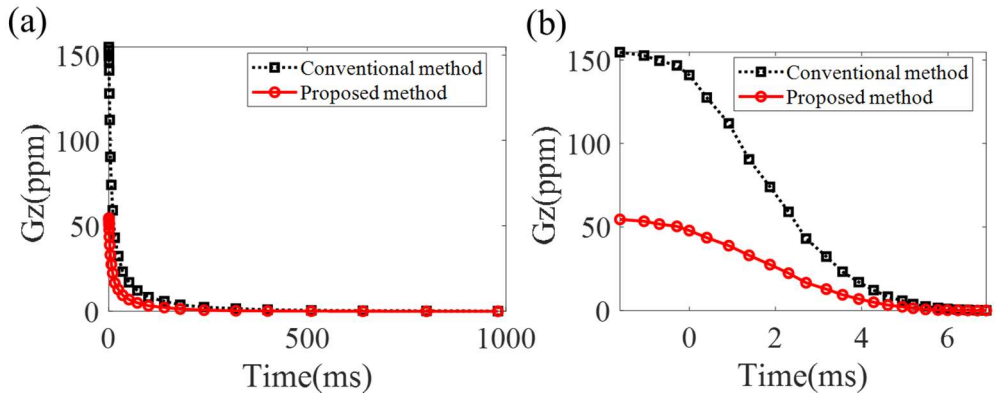

Fig. 3. 21 Magnitudes of the eddy currents at various delay times after the test gradient pulse. (a) Original and (b) enlarged version. The vertical axis Gz represents the magnetic induction, its unit (ppm) means the value of parts per million of the original field.

The platform of the low-field MRI device is shown in Fig. 3.22. The water phantom was placed inside the RF receiving coil. With the gradient coil from the proposed and conventional methods, T2-weighted images of the water phantom were obtained as shown in Fig. 3.23, respectively. T2-weighted images are used here for comparison instead of T1-weighted images because T2-weighted images are more susceptible to gradient eddy currents. The z-direction was chosen as the phase-encoding direction to emphasize the eddy-current effects of the Z-gradient coil. The image blurring in the encoding direction is a symptom of artifacts, which is obvious in Fig. 3.23(b) and improved in Fig. 3.23(a), especially inside the red box. The suggested gradient coil designed using the proposed approach can reduce image-level artifacts.

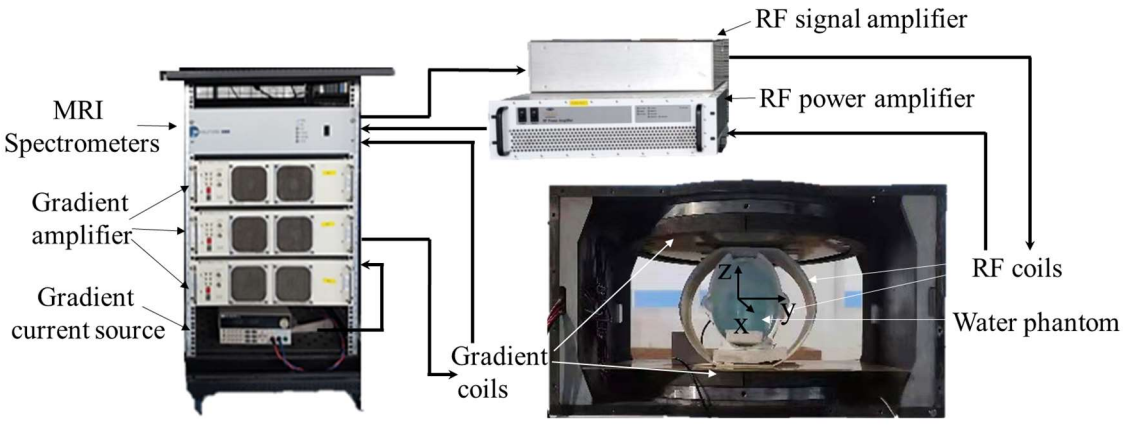

Fig. 3. 22 Imaging platform: the low-field MRI device (50 mT).

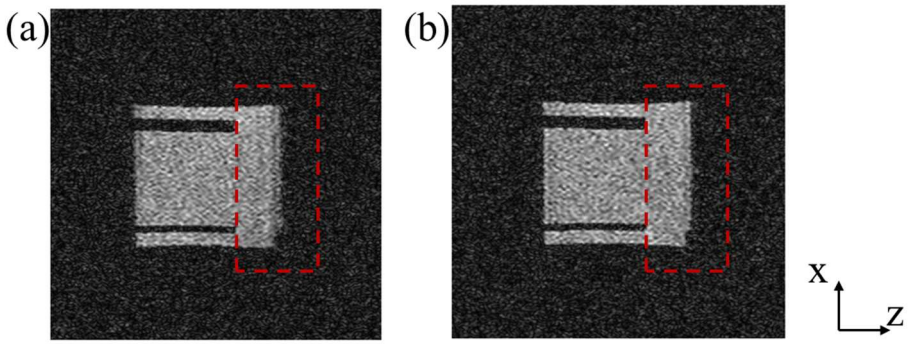

Fig. 3. 23 T2-weighted images in the x-z plane of the cylindrical phantom (CuSO4·5H2O, 1.95 g/L). The Z-gradient coil was designed using (a) the proposed method and (b) the conventional method. The Z-direction was the coding direction, and the imaging sequence was a fast spin echo (FSE). Echo time [TE] = 140 ms, repetition time [TR] = 3200 ms. dwell time =160 μs, and band width is 6.25 kHz.

Chapter 4 Topology Design of the Permanent Magnets and Iron Yoke

4.1 Multi-fidelity Topology Optimization Method

We begin with a typical topology optimization problem using the NGnet method [43]. In this section, we consider an electromagnetic structure consisting of two functionally distinct components, denoted as C_1 and C_2. The topologies of these components are represented by shape functions as

$$y_k(\boldsymbol{x}, \boldsymbol{w}^k) = \sum_{i=1}^{N_k} w_i^k \, b_i(\boldsymbol{x}), (k = 1,2), \tag{4.1}$$

where $w_i^k \in [-1, 1]$, N_k, and $\boldsymbol{x}$ denote the weighting coefficient, number of Gaussian base functions (also referred as Gaussian bases) for the k-th shape function y_k, and constant position vector, respectively. $\boldsymbol{w}^k$ is the weighting coefficient vector and $\boldsymbol{w}^k = [w_1^k, w_2^k, \cdots w_{N_k}^k]$. Moreover, $b_i(\boldsymbol{x})$ is a normalized Gaussian function given by

$$b_i(\boldsymbol{x}) = G_i(\boldsymbol{x}) / \sum_{j=1}^{N_k} G_j(\boldsymbol{x}), \tag{4.2}$$

$$G_i = \frac{1}{2\pi\sigma^2} \exp\left\{-\frac{1}{2\sigma^2} |\boldsymbol{x} - \boldsymbol{x}_i|^2\right\}, \tag{4.3}$$

where σ and $\boldsymbol{x}i$ denote the standard deviation and center of the Gaussian base function, respectively. Fig. 4.1 illustrates the schematic diagram of the NGnet method.

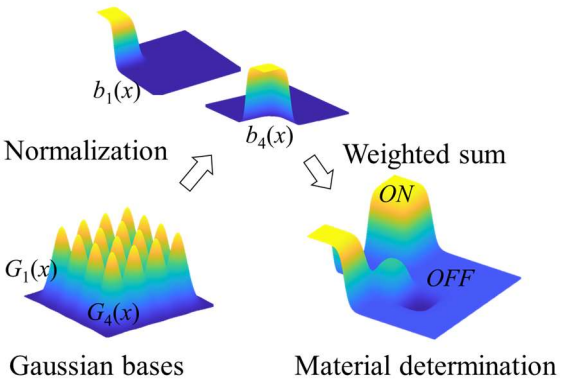

Fig. 4. 1 NGnet method.

Taking the iron design as an example, the material attribute *me* of finite element *e* in the design region is determined from the shape function $y(\boldsymbol{x})$ as

$$m_e \leftarrow \begin{cases} iron & y(\boldsymbol{x}) \geq 0 \\ air & y(\boldsymbol{x}) < 0. \end{cases} \tag{4.4}$$

We determine proper N_k and σ to cover all parts of the design region.

The design variables in the form of a weighting coefficient vector $\boldsymbol{w}^k$ are determined using the covariance matrix adaptation evolution strategy (CMA-ES). We define a single-fidelity optimization problem as

$$\min_{\boldsymbol{w}^1, \boldsymbol{w}^2} F(\boldsymbol{w}^1, \boldsymbol{w}^2), \tag{4.5}$$

where $\boldsymbol{w}^1$ and $\boldsymbol{w}^2$ represent the weighting coefficient vectors determining the structures of C_1 and C_2, respectively. However, in practical scenarios, the function $F(\boldsymbol{w}^1, \boldsymbol{w}^2)$ tends to be a high-dimensional, nonconvex, and nonlinear function, making it difficult to find the global optimal solution. To address this complexity, we propose a multi-fidelity topology optimization method that simplifies the objective function as

$$F(\boldsymbol{w}^1, \boldsymbol{w}^2) = F_1(\boldsymbol{w}^1, \boldsymbol{w}^2) + F_2(\boldsymbol{w}^1, \boldsymbol{w}^2). \tag{4.6}$$

Based on the knowledge at the physical level, it is assumed that F_1 is strongly correlated with $\boldsymbol{w}^1$ and weakly correlated with $\boldsymbol{w}^2$, and vice versa for F_2. The correlation map is shown in Fig. 4.2.

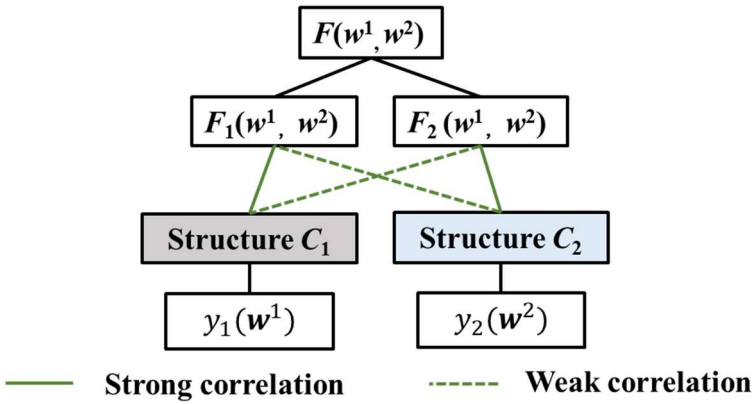

Fig. 4. 2 Correlation map.

We then consider a two-step optimization defined by

$$\min_{\boldsymbol{w}^1} F_1(\boldsymbol{w}^1, \boldsymbol{w}_0^2), \text{ with } \boldsymbol{w}_0^2 = \text{const.}, \tag{4.7}$$

$$\min_{\boldsymbol{w}^2} F_2(\boldsymbol{w}_*^1, \boldsymbol{w}^2), \text{ with } \boldsymbol{w}_*^1 = \arg\min_{\boldsymbol{w}^1} F(\boldsymbol{w}^1, \boldsymbol{w}_0^2), \tag{4.8}$$

where $\boldsymbol{w}_0^2$ represents the initial weighting coefficient vectors that determine the initial structure for C_1; setting it to fully negative values indicates that its influence is not considered in the first step. $\boldsymbol{w}_*^1$ represents the weighting coefficient vectors corresponding to the optimal structure in the first step of optimization.

Suppose that sub-problems F_1 and F_2 require different levels of resolution in the modeling and performance evaluation. As shown in Fig. 4.3, F_1 is a low-fidelity optimization problem that employs larger Gaussian bases and a less precise performance evaluation, whereas F_2 is a high-fidelity problem that employs smaller Gaussian bases and a more precise performance evaluation.

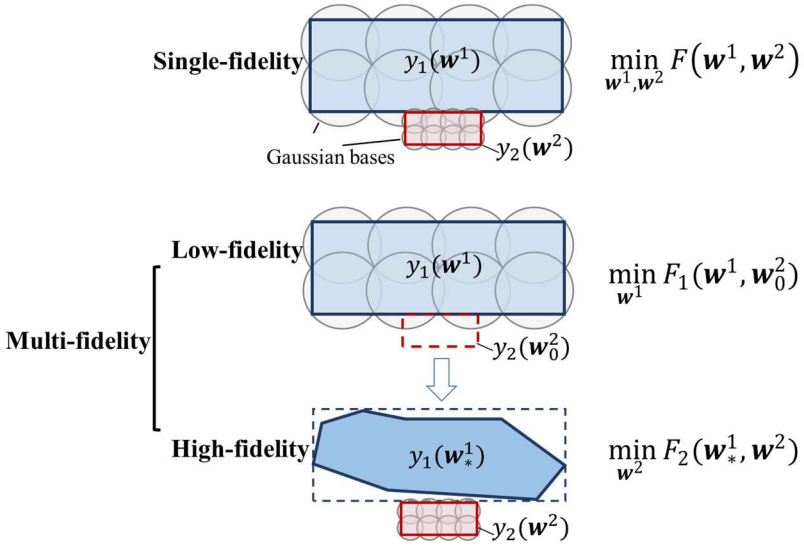

Fig. 4. 3 Schematic for single- and multi-fidelity methods.

4.2 Mathematical Model

A benchmark problem was constructed to demonstrate the effects of the multi-fidelity method. Assume that $\boldsymbol{w}^1$=$[x_1,\ x_2]$, $\boldsymbol{w}^2 = [x_3, x_4]$. $F_1(\boldsymbol{w}^1, \boldsymbol{w}_0^2)$ and $F_2(\boldsymbol{w}_0^1, \boldsymbol{w}^2)$ are defined as

$$F_k = \sum_{i=1}^{N_k} h_i\, e^{-\frac{\left(x_{(2k-1)}-p_{i1}\right)^2+\left(x_{(2k)}-p_{i2}\right)^2}{v_i}}, (k = 1,2) \tag{4.9}$$

where the parameters for F_1 and F_2 are given in Table 4.1.

When $x \in [-1,1]$, both $F_1(\boldsymbol{w}^1, \boldsymbol{w}_0^2)$ and $F_2(\boldsymbol{w}_0^1, \boldsymbol{w}^2)$ exhibit multiple peaks, with $F_2(\boldsymbol{w}_0^1, \boldsymbol{w}^2)$ having sharp peaks, as shown in Fig. 4.4.

Table 4. 1 Parameters of functions F1 and F2

Parameter	F_1	F_2
N_k	3	5
h	[1.0, 1.2, 1.5]	[1.0, 1.2, 1.5, 3, 2.0]
p_1	[0.3, 0.4, -0.4]	[0.4, -0.4, 0.4, -0.4, 0.0]
p_2	[0.4, 0.3, 0.4]	[0.4, -0.4, -0.4, 0.4, 0.0]
v	[0.01, 0.05, 0.3]	[0.001, 0.005, 0.03, 0.0006, 0.3]

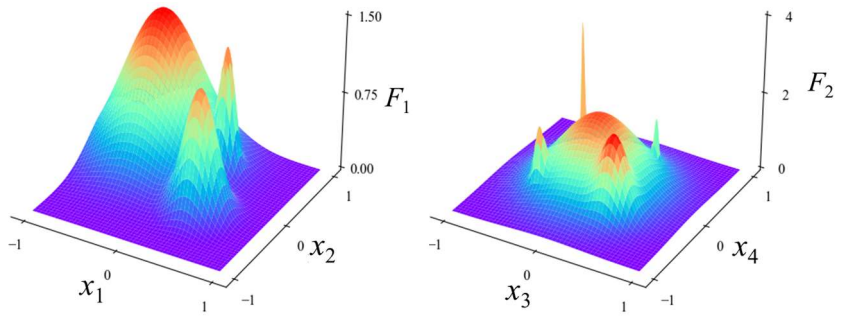

Fig. 4. 4 Function values of F_1 (x_1, x_2) and F_2 (x_3, x_4).

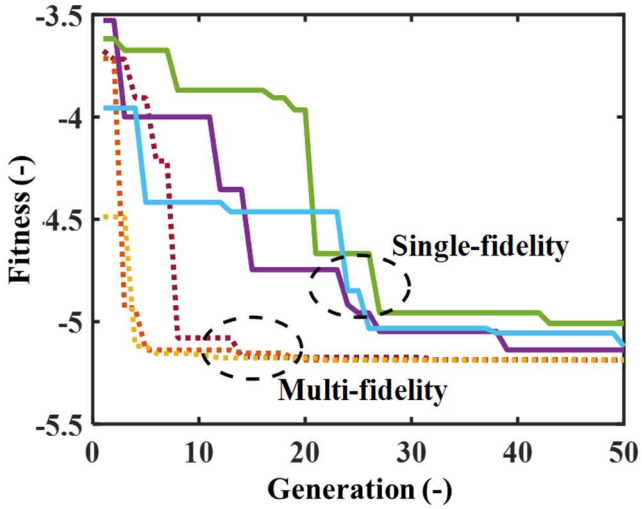

Fig. 4. 5 Convergence histories of single- and multi-fidelity optimizations.

We compared the performances of the single- and multi-fidelity methods by repeating each

type of optimization thrice. The convergence plots in Fig. 4.5 highlight the superior performance of the multi-fidelity method in this scenario. The parameters used for the CMA-ES algorithm in this case are listed in Table 4.2.

Table 4. 2 Parameters of optimization based on CMS-ES

Parameter	Value
Population size	3,200
Number of Generations	50
Initial standard deviation	0.7
Cumulation of step-size	0.3
Damping for step-size	0.6

4.3 Design Results

4.3.1 Two-dimensional(2-D) Case

For the low-field MRI device, the structures of the iron yoke and the shimming magnet must be determined. Fig. 4.6 shows the design model. A pair of bipolar magnets is used to generate a vertical magnetic field in the target region. The design region for the iron yoke and shimming magnet is covered by circles that represent the influence region of the Gaussian bases. The structure is mirror-symmetric, allowing us to focus only on one-fourth of the model during the design process.

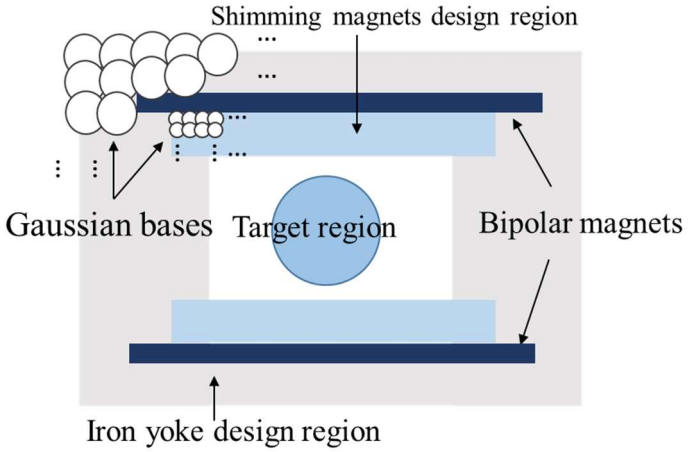

Fig. 4. 6 Optimization model.

The design aims to maximize the average magnetic flux density (B_{ave}), minimize the field non-uniformity (ΔB) in the target region, and minimize the total weight of the device (W). The single-fidelity optimization problem is defined as

$$\min_{\boldsymbol{w}^1} F(\boldsymbol{w}^1, \boldsymbol{w}^2)$$

$$\min_{\boldsymbol{w}^1} F(\boldsymbol{w}^1, \boldsymbol{w}^2) = \min_{\boldsymbol{w}^1} \left\{ -\frac{B_{ave}(\boldsymbol{w}^1, \boldsymbol{w}^2)}{B_{ave}^{ref}} + \frac{\Delta B(\boldsymbol{w}^1, \boldsymbol{w}^2)}{\Delta B^{ref}} + \frac{0.1W(\boldsymbol{w}^1, \boldsymbol{w}^2)}{W^{ref}} \right\}, \quad (4.10)$$

where $\boldsymbol{w}^1$ and $\boldsymbol{w}^2$ are the weighting coefficient vectors in the iron yoke and magnet design regions, respectively. The simultaneous design of these two structures often results in local optima because non-uniformity is sensitive to structural changes, which results in a complex solution space with multiple sharp peaks. Designing both structures simultaneously requires searching for a sharp optimum value in a higher-dimensional (e.g., 50-dimensional) space, which is almost impossible.

We can use the multi-fidelity topology optimization method proposed in Section 4.1 to simplify the problem. Practical experience has shown that the primary function of the yoke is to create a magnetic loop to increase the field strength, whereas the shimming magnet is responsible for reducing non-uniformity. The correlations between the target functions and these structures are shown in Fig. 4.7. The iron yoke exhibits a close relationship with B_{ave}, whereas the shimming magnet is closely related to ΔB. The W were determined using both the iron yoke and the shimming magnet.

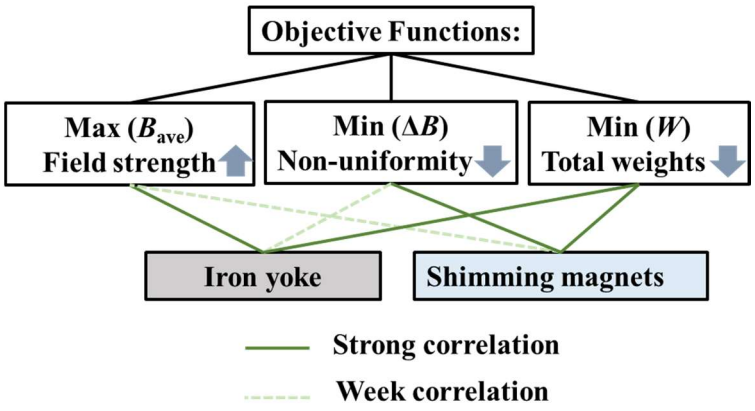

Fig. 4. 7 Correlation map for low-field MRI devices' design.

According to the correlation map, the iron yoke and the shimming magnet can be designed in sequence by defining the multi-fidelity objective function as

$$F(\boldsymbol{w}^1, \boldsymbol{w}^2) = F_1(\boldsymbol{w}^1, \boldsymbol{w}^2) + F_2(\boldsymbol{w}^1, \boldsymbol{w}^2), \tag{4.11}$$

and the two-step optimization is defined as

$$\begin{aligned} \min_{\boldsymbol{w}^1} F_1(\boldsymbol{w}^1, \boldsymbol{w}_0^2) &= \min_{\boldsymbol{w}^1} \left\{ -\frac{B_{ave}(\boldsymbol{w}^1, \boldsymbol{w}_0^2)}{B_{ave}^{ref}} + \frac{0.1W(\boldsymbol{w}^1, \boldsymbol{w}_0^2)}{W^{ref}} \right\}, \\ \min_{\boldsymbol{w}^2} F_2(\boldsymbol{w}_*^1, \boldsymbol{w}^2) &= \min_{w^2} \left\{ \frac{\Delta B(\boldsymbol{w}_*^1, \boldsymbol{w}^2)}{\Delta B^{ref}} + \frac{0.1W(\boldsymbol{w}_*^1, \boldsymbol{w}^2)}{W^{ref}} \right\}, \end{aligned} \tag{4.12}$$

W is the weight of the 3-D model (obtained by stretching 2-D model by 660 mm), $B_{ave}^{ref} = 0.1\,\mathrm{T}$, and $W^{ref} = 200\,\mathrm{kg}$. ΔB is defined as $\Delta B = 10^6(B_{max} - B_{min})/B_{max}$, $\Delta B^{ref} = 1{,}000$ ppm. F_1 and F_2 are treated as low- and high-fidelity optimization problems, respectively. We employed different sizes of Gaussian bases (represented by their standard deviation σ), and varied the precision of the performance evaluation in these two steps. The design parameters are given in Table 4.3.

Table 4. 3 Parameters of the low and high-fidelity designs

Parameters	Low-fidelity	High-fidelity

Standard deviation (mm)	100	30
Number of Gaussian bases	30	20
Field precision (ppm)	1,000	100
Material type	Iron (Q235)	Magnet (NdFeB)

The field evaluation is realized using the FEM. Fig. 4.8 shows the optimal structures and corresponding magnetic flux maps obtained using the single- and multi-fidelity design methods.

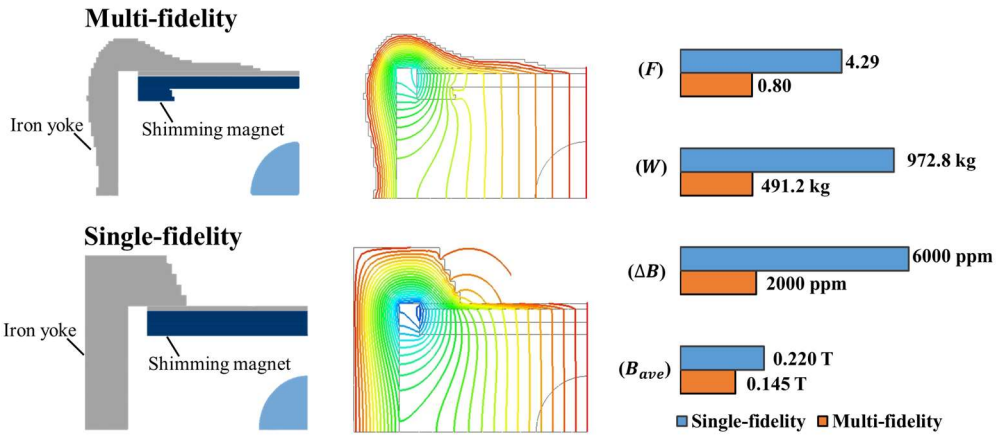

Fig. 4. 8 Optimal structures and flux map of single- and multi-fidelity designs and optimal performance comparison.

The convergence histories of objective function and performance are compared in Fig. 4.9. The single-fidelity method quickly converged to a local optimum (F=4.29), whereas the multi-fidelity method achieved better fitness (F=0.80) after two steps of optimization. The single-fidelity optimal structure produces a comparatively high B_{ave}; however, it suffers from high ΔB and W. In contrast, the optimal structure designed using the multi-fidelity method achieves a more rational balance between multiple design objectives.

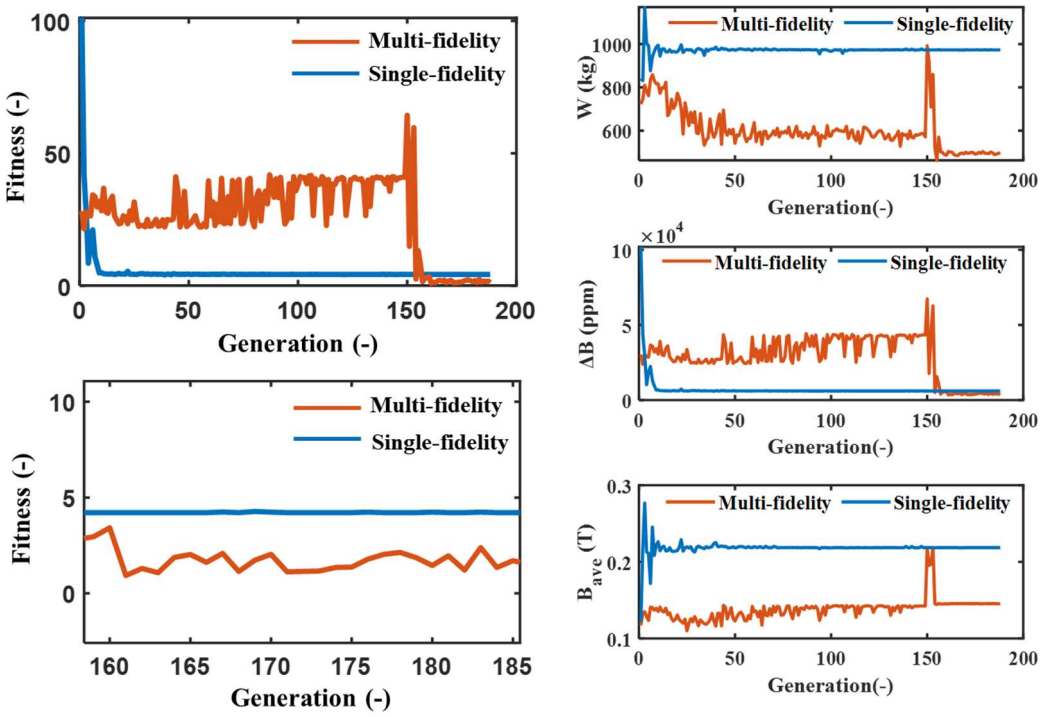

Fig. 4. 9 Convergence histories of fitness and performances.

4.3.2 Three-dimensional(3-D) Case

The proposed method is also applicable to the 3-D model, and the objective functions were the same for the 2-D one. Fig. 4.10 shows the optimization model (1/8 model) for the iron yoke design. A pair of bipolar permanent magnets are used to produce vertical magnetic field in ROI. The design region for iron yoke is covered by spheres representing the influence region of the Gaussian bases. The standard deviation σ of the three-dimensional normalized Gaussian basis function is set to 100 mm to cover the entire design region.

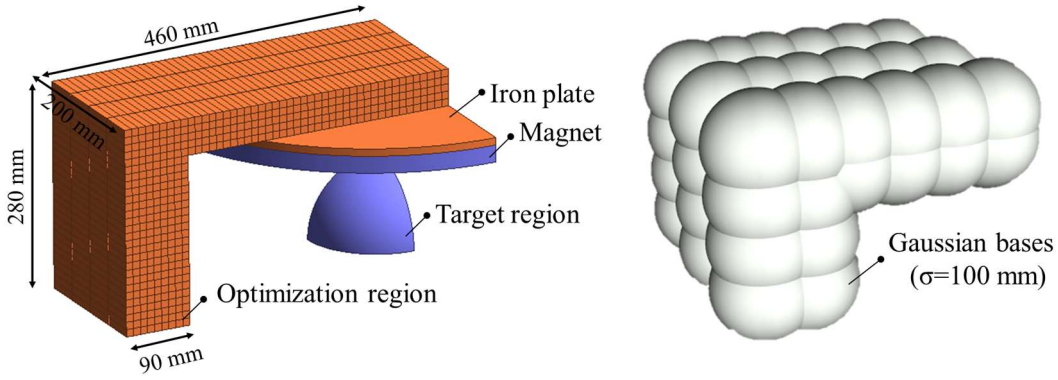

Fig. 4. 10 Design model and Gaussian bases distribution.

As for the multi-fidelity optimization, Fig. 4.11 show several representing structures during the optimization process. As the optimization progresses, the weight of the iron yoke gradually converges to a minimum while maintaining no significant reduction in magnetic field strength.

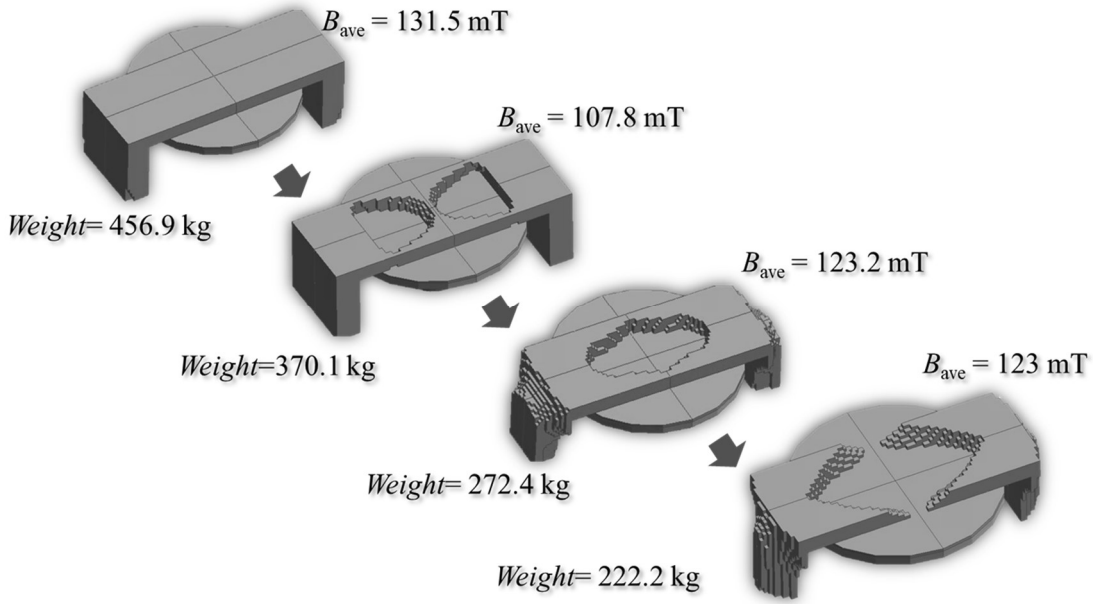

Fig. 4. 11 Optimization process for the iron yoke.

Fig. 4.12 shows the optimal designs obtained from the single- and multi-fidelity methods. Their performances are listed in Table 4.4. The design results show that the multi-fidelity method has better performance in both 2-D and 3-D spatial designs. The significant difference between the optimal structures in 3-D and 2-D models arises from the fact that the 2-D model didn't

consider the influence of edge effects on the magnetic field distribution.

Table 4. 4 Performances comparison

	B_{ave} (T)	W(kg)	ΔB(ppm)	F(-)
Single-fidelity	0.183	448.2	24,000	22.39
Multi-fidelity	0.123	222.2	5,000	3.88

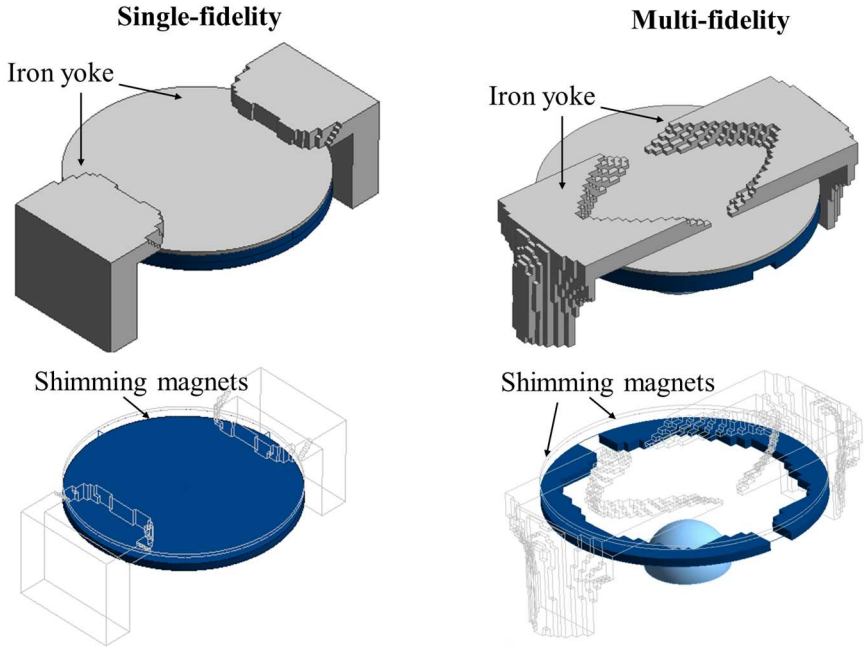

Fig. 4. 12 Optimal 3-D structures from single- and multi-fidelity methods.

Chapter 5 Passive Shimming of Static Magnetic Field

5.1 Evaluation Model for the Single Shimming Magnet

First, we consider the situation without the effects of the iron yoke. We can use the equivalent magnetizing current method [59] to calculate the magnetic field of a cylindrical magnet. This method models the magnetization distribution of the permanent magnet as a set of equivalent current loops and then applies Ampère's Circuital Law to calculate the magnetic field it generates.

The magnetic field produced at any point outside the permanent magnet is the result of the super-positioning of all the magnetizing current loops on the surface of the permanent magnet. For a single cylindrical magnet, establish a coordinate system as shown in Fig. 5.1 (a), with the magnet's axis aligned along the z-axis, the upper surface of the magnet located at $z = z_2$, and the lower surface of the magnet located at $z = z_1$. The magnet has a radius of a, and its remanent magnetization is B_r. The magnet can be represented by an equivalent magnetizing surface current, with current density uniformly distributed on the cylindrical surface, and the differential length is dz_0, as shown in Fig. 5.1 (b). The modeling of each current loop is depicted in Fig. 5.1 (c).

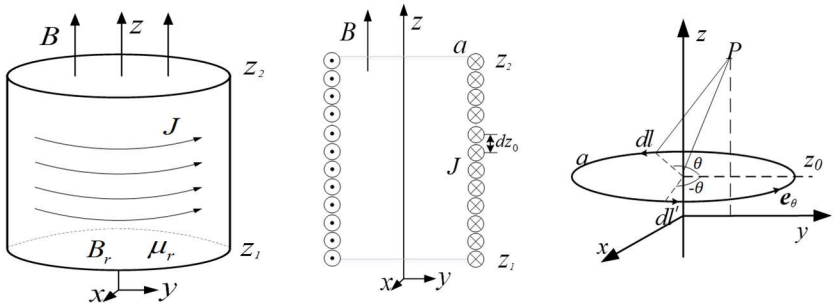

(a) (b) (c)

Fig. 5. 1 Principle of the magnetizing current.(a) Magnetizing currents in a cylindrical magnet, and (b) the cross-section, (c) single current loop.

The equivalent magnetizing current density can be expressed as

$$\boldsymbol{J} = \frac{B_r}{\mu_0}\boldsymbol{e}_\theta, \tag{5.1}$$

where B_r is remanence of the magnet, μ_0 is the permeability of vacuum, $\boldsymbol{e}_\theta$ is the unit vector in the circumferential direction. Assume a current *I* in the circular loop model, according to Biot-Savart's Law, the vector magnetic potential ***A*** can be expressed as

$$\boldsymbol{A} = \frac{\mu_0}{4\pi}\oint_l \frac{I d\boldsymbol{l}}{r}. \tag{5.2}$$

Since the computational model is a circularly symmetric structure, we establish a cylindrical coordinate system. By symmetry, the vector potential is azimuthal,

$$A_\theta = A_p = \frac{\mu_0 I}{4\pi}\int_0^{2\pi} \frac{a d\theta \cdot \cos\theta}{\sqrt{a^2+\rho^2+(z-z_0)^2-2a\rho\cos\theta}}. \tag{5.3}$$

Assume that

$$\alpha = \frac{1}{2}(\theta - \pi), \tag{5.4}$$

Then,

$$\frac{1}{2}\cos\theta\, d\theta = (2\sin^2\alpha - 1)d\alpha. \tag{5.5}$$

So, equation (5.3) can be expressed as:

$$A_\theta = \frac{\mu_0 I a}{\pi}\int_0^{\pi} \frac{(2\sin^2\alpha - 1)d\alpha}{\sqrt{(a+\rho)^2+(z-z_0)^2-4a\rho\sin^2\alpha}}. \tag{5.6}$$

Assume that

$$k^2 = \frac{4a\rho}{\sqrt{(a+\rho)^2 + (z-z_0)^2}}, \tag{5.7}$$

formula (5.6) can be expressed as:

$$A_\theta = \frac{\mu_0 I}{\pi k}\sqrt{\frac{a}{\rho}}\left[\left(1-\frac{k^2}{2}\right)K(k) - E(k)\right], \tag{5.8}$$

where $K(k)$ is the complete elliptic integral of the first kind:

$$K(k) = \int_0^{\frac{\pi}{2}} \frac{d\alpha}{\sqrt{1-k^2\,sin^2\,\alpha}}, \tag{5.9}$$

and $E(k)$ is the complete elliptic integral of the second kind:

$$E(k) = \int_0^{\frac{\pi}{2}} \sqrt{1-k^2\,sin^2\,\alpha}\,d\alpha\,. \tag{5.10}$$

According to $\boldsymbol{B} = \nabla \times \boldsymbol{A}$, the magnetic flux density generated by the circular loop current at point P can be calculated as follows:

$$B_\rho = \frac{\mu_0 I}{2\pi}\frac{z-z_0}{\rho\sqrt{(a+\rho)^2+(z-z_0)^2}}\left[-K(k) + \frac{a^2+\rho^2+(z-z_0)^2}{(a-\rho)^2+(z-z_0)^2}E(k)\right] \tag{5.11}$$

$$B_z = \frac{\mu_0 I}{2\pi}\frac{1}{\sqrt{(a+\rho)^2+(z-z_0)^2}}\left[K(k) + \frac{a^2-\rho^2-(z-z_0)^2}{(a-\rho)^2+(z-z_0)^2}E(k)\right] \tag{5.12}$$

Replace I with $B_r/\mu_0\,dz_0$, and integrate z_0 within the range $[z_1, z_2]$, we can obtain the magnetic field produced by a single cylindrical magnet:

$$B_\rho = \frac{B_r}{2\pi}\int_{z_1}^{z_2}\frac{z-z_0}{\rho\sqrt{(a+\rho)^2+(z-z_0)^2}}\left[-K(k) + \frac{a^2+\rho^2+(z-z_0)^2}{(a-\rho)^2+(z-z_0)^2}E(k)\right]dz_0 \tag{5.13}$$

$$B_z = \frac{B_r}{2\pi}\int_{z_1}^{z_2}\frac{1}{\sqrt{(a+\rho)^2+(z-z_0)^2}}\left[K(k) + \frac{a^2-\rho^2-(z-z_0)^2}{(a-\rho)^2+(z-z_0)^2}E(k)\right]dz_0 \tag{5.14}$$

Since the static magnetic field is along the z-direction, we are only concerned with the z-component of the magnetic field. Equation 5.14 can be used to calculate the magnetic field of a cylindrical magnet in air. In practice, however, we need to consider the influence of the iron yoke because the iron yoke forms a magnetic flux path that enhances the magnetic field generated by the shimming magnet.

For FEM calculation, the saturation magnetization resulting from adding the shimming magnets can be neglected. Therefore, In Fig. 5.2, the super-position of the field of ROI from model (b) and (c) is equivalent to that of model (a). When altering the distribution of the shimming magnets, the model in Fig. 5.2 (b) remains unchanged. Therefore, the magnetic field within the ROI in Fig. 5.2 (b) serves as the base field, and can be obtained from FEM calculation. We here define the magnetic field in ROI of Fig. 5.2 (b) and Fig. 5.2 (c) as base field and shimming field.

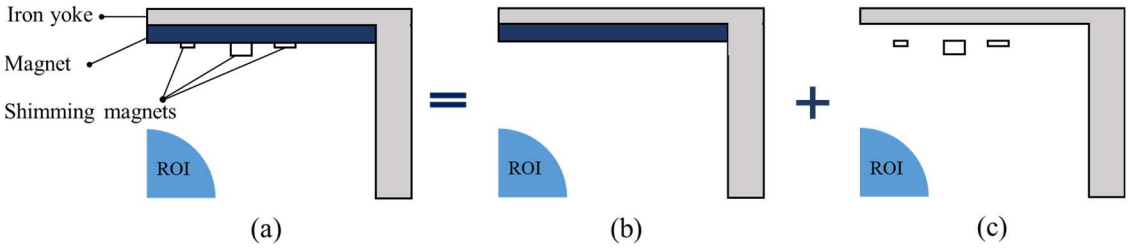

Fig. 5. 2 FEM calculation model for the shimming magnet.

As depicted in Fig. 5.3, we further simplify the model. The magnetic field produced by the shimming magnet shown in Fig. 5.3(b) can be calculated by equivalent magnetizing current method [59] and image current method [27]. The influence of the iron yoke can be effectively modeled as an infinitely large magnetic plate since the shimming magnet is significantly smaller relative to the iron yoke. According to the image current theory, the influence of an infinitely large magnetic plate can be further simplified as image currents. Therefore, the model composed of the shimming magnet and the iron yoke can be simplified to a combination of magnetization currents and mirror currents, allowing for the calculation of the shimming field using theoretical methods.

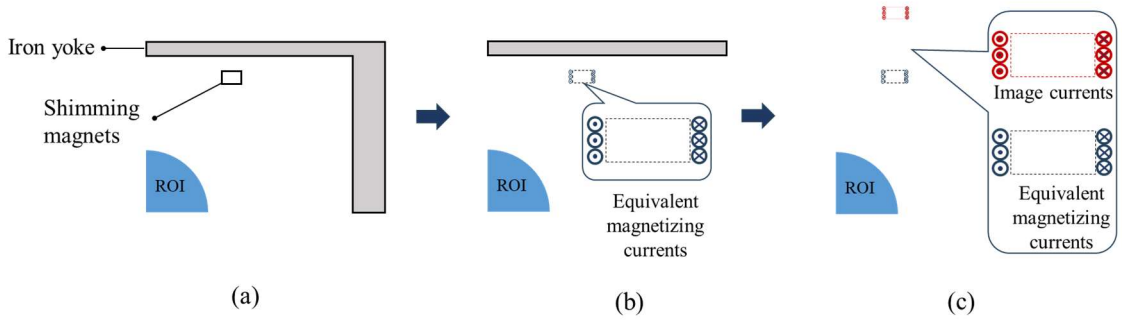

Fig. 5. 3 Theoretical model for the shimming PMs design.

Finally, the field produced by the whole model (Fig. 5.4(a)) can be obtained by super-positioning the base magnetic field (from FEM calculation, as shown in Fig. 5.4(b)) and the shimming field (from theoretical model, as shown in Fig. 5.4(c)). We define the combination of model Fig. 5.4(b) and Fig. 5.4(c) as a FEM-theoretical model.

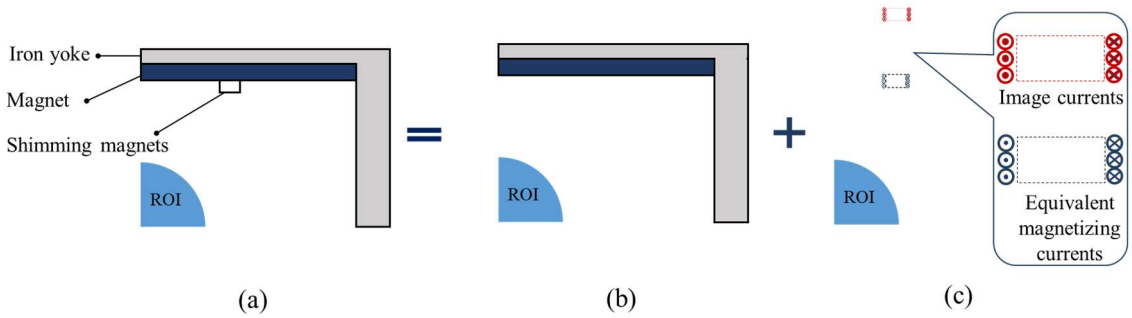

Fig. 5. 4 FEM-theoretical model for the shimming magnets design.

5.2 FEM-theoretical Model Verification

In order to verify the accuracy of the FEM-theoretical model, we compared the magnetic field from FEM model and FEM-theoretical model. Take a real case for example, as shown in Fig. 5.5. The contour plot of the magnetic field distribution within the ROI is depicted in Fig. 5.6, while a comparison of the numerical values along the dashed line is presented in Fig. 5.7. The maximum relative error between FEM model and FEM-theoretical model is smaller than 0.025% (250 ppm).

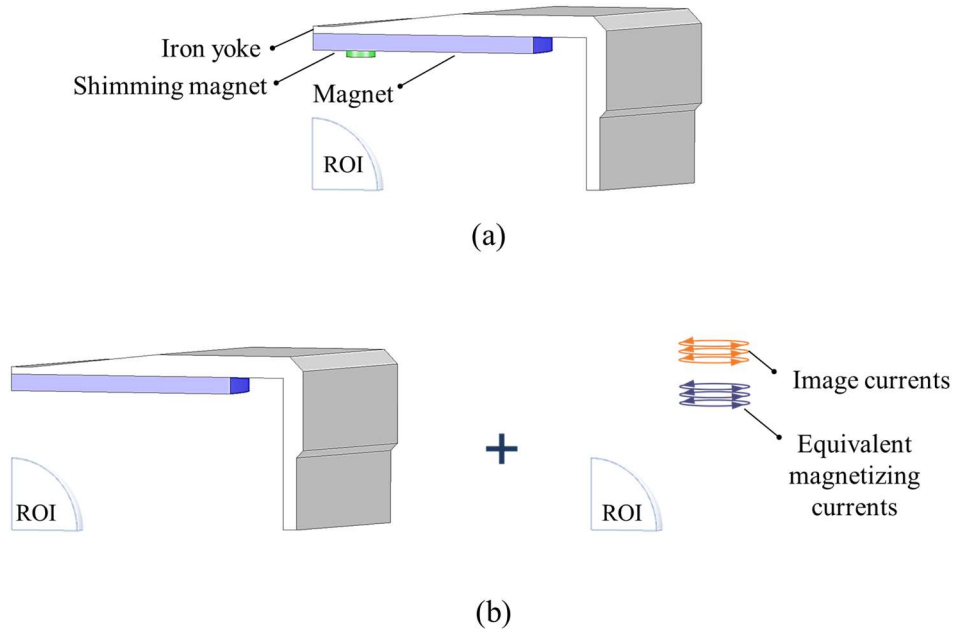

Fig. 5. 5 Calculation models. (a) FEM model, and (b) FEM-theoretical model.

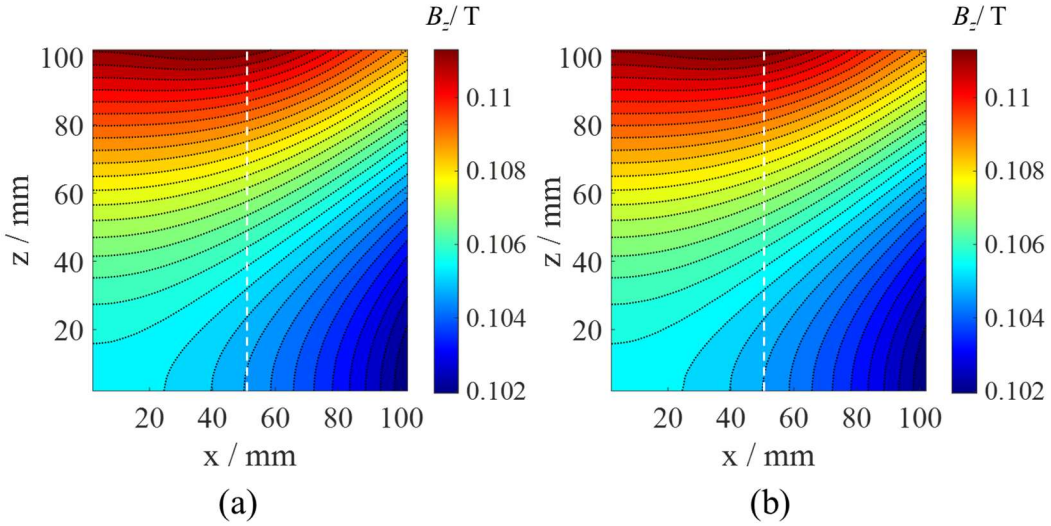

Fig. 5. 6 Magnetic field comparison, Bz in (a) FEM-theoretical model, and (b) FEM model

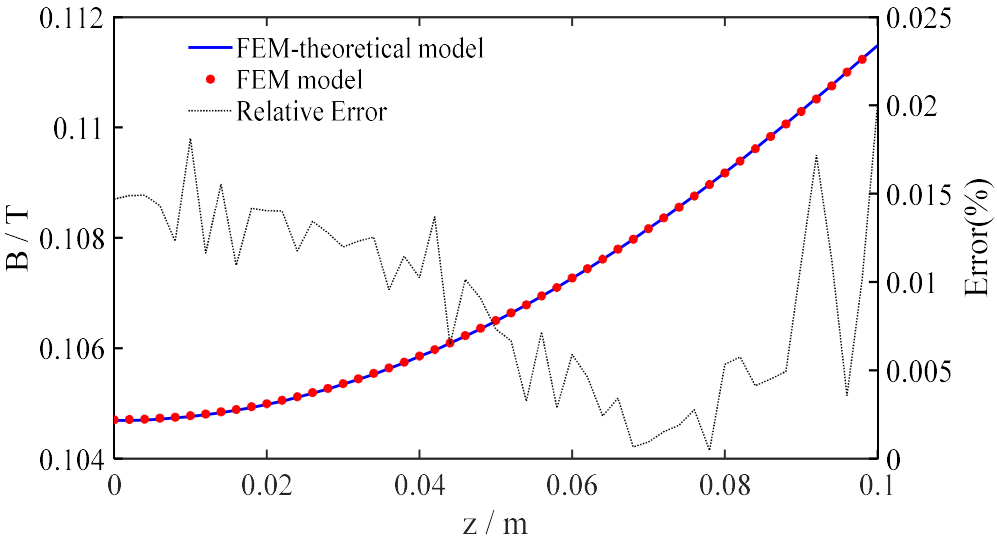

Fig. 5. 7 Magnetic field comparison between FEM-theoretical and FEM model (Bz along dotted lines)

5.3 Optimization Method

Based on the proposed FEM-theoretical model, we further adopt the linear optimization to optimize the distribution of shimming magnets. First, the magnetic field produced by all the shimming magnets is calculated by super-positioning the field given by

$$\boldsymbol{B}_{mp} = \boldsymbol{AX}, \tag{5.15}$$

where

$$\boldsymbol{A} = \begin{bmatrix} A_{11} & \cdots & A_{1k} \\ \vdots & \ddots & \vdots \\ A_{n1} & \cdots & A_{nk} \end{bmatrix}, \tag{5.16}$$

$$\boldsymbol{X} = [x_1, \cdots, x_j, \cdots, x_n]^T, \tag{5.17}$$

where A_{ij} depicts the magnetic induction in the i-th target point produced by the j-th shimming magnet, which can be calculated using the proposed FEM-theoretical model. x_j depicts the thickness of the j-th shimming magnet, which is the unknown variable need to be optimized.

The optimization objective is to minimize the total thickness of all shimming magnets while ensuring required non-uniformity. The optimization problem is defined as follows:

$$\begin{aligned} \min: F &= \sum_{j=0}^{n} |x_i|, \\ \text{sub. to } B_{ave}(1-\sigma_f) &< AX + B_{base} < B_{ave}(1+\sigma_f), \end{aligned} \tag{5.18}$$

where σ_f denotes the field error between ideal field and optimized field, B_{base} is obtained from FEM model of Fig. 5.4 (b). Moreover, B_{ave} denotes the desired average magnetic density in ROI. Linear programming is used to solve this optimization problem because of its fast convergence speed. Due to the strict non-uniformity requirements (for example, below 150 ppm), the accuracy of the FEM-analytical model may introduce some errors. Therefore, we propose the use of a multi-step method for optimizing the shim magnets. The shimmed field derived from the initial iteration serves as the base magnetic field for subsequent iterations, and this process continues iteratively. The iterative process continues until the desired level of non-uniformity is achieved.

5.4 Design Results

In the first optimization iteration, the value of σ_f is set to be 0.04 % (400 ppm). The results of the first shimming are shown in Fig. 5.8, with red and blue representing shimming magnets magnetized in the same or opposite direction to the main magnetic field, respectively. The value of U_{non} in the target region is 10000 ppm when there are no shimming magnets, and that decreases to 558 ppm after the first iteration.

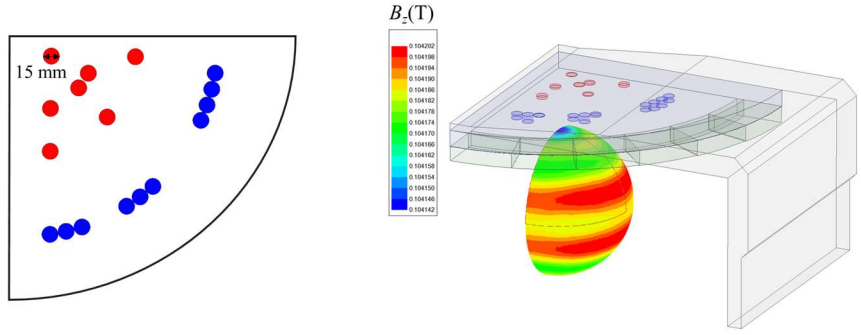

(a) (b)

Fig. 5. 8 Optimized shimming magnets and simulation results of the first step. (a) Distribution of optimized shimming magnets, and (b) simulated field.

In order to further improve the uniformity, the second iteration was carried out. The second step is based on the field results of the first step, and the value of σ_f is set to be 0.01% (100 ppm). As shown in Fig. 5.9, the thicknesses of shimming magnets are adjusted based on the optimal results from the first step, which reduces U_{non} from 558 ppm to 215 ppm.

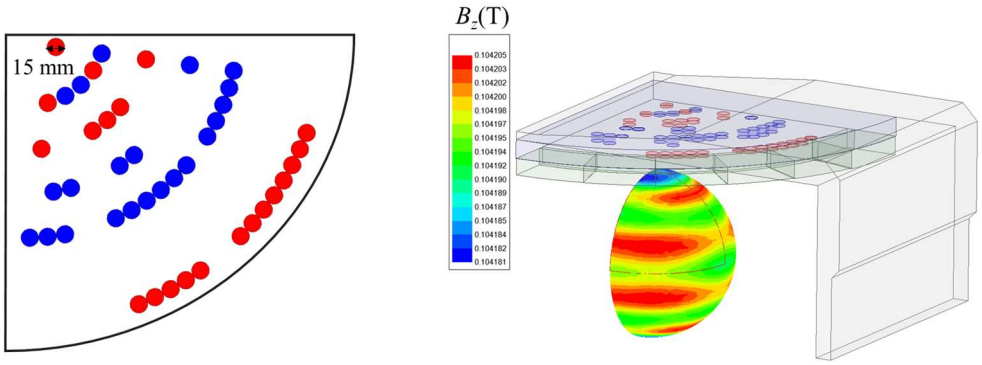

(a) (b)

Fig. 5. 9 Optimized shimming magnets and simulation results of the second step. (a) Distribution of optimized shimming magnets, and (b) simulated field.

Similarly, based on the results of the second optimization, a third optimization iteration was conducted. In the third step, the desired non-uniformity was set to be 100 ppm again, and the non-uniformity calculated by FEM model was 125 ppm, as illustrated in the Fig. 5.10. The optimized results of these three steps are summarized in Table 4.5. After three times optimizations, the U_{non} reaches 125 ppm, which is an acceptable non-uniformity.

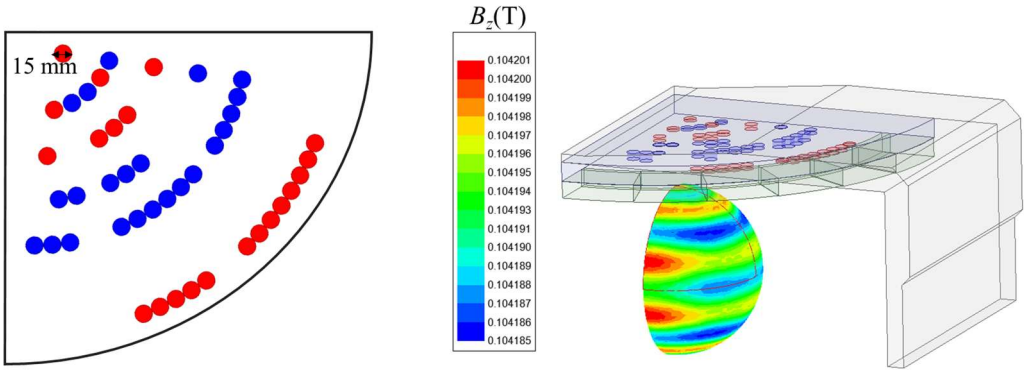

(a) (b)

Fig. 5. 10 Optimized shimming magnets and simulation results of the third step. (a) Distribution of optimized shimming magnets, and (b) simulated field.

Table 5. 1 Non-uniformity of Optimized Results

Step	U_{non} (ppm)	
	Before shimming	After shimming
1st	10000	558
2nd	558	215
3rd	215	125

Chapter 6 Conclusion

6.1 Gradient Coil Design Considering Field Distortion Effects.

A novel method for designing gradient coils for low-field MRI devices was proposed. The proposed method considered the effect of magnetic materials, particularly anti-eddy plates, by introducing image dipole currents. In the optimal design of gradient coils, the effect of ferromagnetic materials was minimized to obtain highly linear fields. The magnetic field measurement results and phantom images revealed the validity of the proposed method.

In future work, more effort should be devoted to designing the structure of anti-eddy plates. Existing anti-eddy plates are not the optimal structure and there is room for optimization. Apart from reducing weight, we can use discrete anti-eddy units placed in positions where they are needed to guide gradient magnetic fields. Meanwhile, we also need to consider the impact of discrete anti-eddy units on the gradient magnetic field.

6.2 Gradient Coil Design Considering Field Distortion Effects

In this study, a design method for Z-gradient coils in low-field MRI systems was proposed, focusing on enhancing anti-eddy performance. The newly introduced design procedure significantly improves the anti-eddy performance of the coils. The study presented simplified 2-D FEM models for both transient and static FEM calculations. A fast 1-D ISF method was employed to enhance gradient efficiency and generate 158 coil patterns. The approximated MOP method considered nonlinearity, gradient efficiency, and inductance simultaneously, selecting candidate coils based on the Pareto optimal front. Anti-eddy performance was evaluated by analyzing transient responses of eddy current loss and eddy field. Ultimately, the anti-eddy performance served as the primary criterion for determining the optimal coil design. Measurement

and imaging results demonstrated that the optimal coil exhibited superior anti-eddy performance compared to conventional coils.

The potential improvements using evolutionary method are possible to improve the optimization efficiency and find better solutions, and this is what we will do in future work. Instead of using the pre-sampled parameter space, we can find a continuous Pareto front using an algorithm such as NSGA (Non-dominated Sorting Genetic Algorithm).

6.3 Topology Design of the Permanent Magnets and Iron yoke

A multi-fidelity topology optimization method has been proposed to alleviate the local optima problem. This method simplifies the design difficulty by dividing the optimization into sub-problems at the physical level. The proposed method showed a better performance than the conventional method in the design of low-field MRI devices. This method can be applied to other complex topology optimization problems, and the definition of multi-fidelity objective functions should consider the actual functions of the structures to be designed.

In future work, we will incorporate the optimization of bipolar magnets, taking into account the interaction between the magnets and the iron yoke through iterative optimization.

6.4 Passive Shimming of Static Magnetic Field

We propose a passive shimming method for adjusting the static magnetic field in the low-field MRI device. Initially, we created a straightforward evaluation model for the shimming magnet by combining a FEM model with a theoretical model. Subsequently, LP was employed to swiftly design the distribution of shimming magnets. A test case validated the effectiveness of this approach, reducing non-uniformity from 10,000 ppm to 125 ppm after three iterations.

In future work, we can explore the application of deep learning-based neural networks to design shimming magnets, aiming to achieve even more accurate predictions.

References

[1] Y. Liu, Y. Shi, F. Mu, J. Cheng, C. Li and X. Chen. "Multimodal MRI Volumetric Data Fusion With Convolutional Neural Networks," IEEE *Trans. Instrum. Meas.*, vol. 71, pp. 1-15, Jun.2022, doi: 10.1109/TIM.2022.3184360.

[2] G. Andria, F. Attivissimo, G. Cavone and A. M. L. Lanzolla, "Acquisition Times in Magnetic Resonance Imaging: Optimization in Clinical Use," IEEE *Trans. Instrum. Meas.*, vol. 58, no. 9, pp. 3140-3148, Sep. 2009, doi: 10.1109/TIM.2009.2016888.

[3] M. H. Mazurek, B. A. Cahn, M. M. Yuen, et al. "Portable, bedside, low-field magnetic resonance imaging for evaluation of intracerebral hemorrhage," *Nat. Commun.,* vol. 12, no. 1*,* pp. 5119, Aug.2021, doi: https://doi.org/10.1038/s41467-021-25441-6.

[4] L. Yang, W. He, Y. He, J. Wu, S. Shen, and Z. Xu. "Active EMI Suppression System for a 50 mT Unshielded Portable MRI Scanner," *IEEE Transactions on Biomedical Engineering.,* vol. 1, no. 1*,* Apr. 2022, doi: 10.1109/TBME.2022.3170450.

[5] Liu, Y., Leong, A.T.L., Zhao, Y. et al. "A low-cost and shielding-free ultra-low-field brain MRI scanner," *Nat Commun.,* vol. 12, no. 1*,* pp. 7238, Dec. 2021, doi: https://doi.org/10.1038/s41467-021-27317-1.

[6] Huang, X. et al. "Adaptive suppression of power line interference in ultra-low field magnetic resonance imaging in an unshielded environment," *J. Magn. Reson.,* vol. 286, pp. 52-59, Jan. 2018, doi: https://doi.org/10.1016/j.jmr.2017.11.009.

[7] Campbell-Washburn, A. E., Ramasawmy, R., Restivo, M. C. et al. "Opportunities in interventional and diagnostic imaging by using high-performance low-field-strength MRI," *RADIOLOGY*, vol. 293, no. 2, pp. 384-393, Oct. 2019, doi: https://doi.org/10.1148/radiol.2019190452.

[8] Sarracenia, M. et al. "Low-cost high-performance MRI," *Sci. Rep*., vol. 15, no. 5, pp. 15177, Oct. 2015, doi: https://doi.org/10.1038/srep15177.

[9] Lother S, Schiff SJ, Neuberger T, Jakob PM, Fidler F. "Design of a mobile, homogeneous, and efficient electromagnet with a large field of view for neonatal low-field MRI," *MAGMA*. vol. 29, no. 4, pp. 691-8, Aug. 2016, doi: 10.1007/s10334-016-0525-8

[10] Choquet P, Breton E, Goetz C, Marin C, Constantinesco A. "Dedicated low-field MRI in mice," *Phys Med Biol*., vol.54, no. 17, pp. 5287-99, Aug.2009, doi: 10.1088/0031-9155/54/17/014.

[11] Cooley, C. Z. et al. “A portable scanner for magnetic resonance imaging of the brain,” *Nat. Biomed. Eng*., vol. 5, no. 3, pp. 229–239, Mar. 2021, doi: 10.1038/s41551-020-00641-5.

[12] O’Reilly, T., Teeuwisse, W. M., de Gans, D., Koolstra, K. & Webb, A. G. “In vivo 3D brain and extremity MRI at 50 mT using a permanent magnet Halbach array,” *Magn. Reson. Med*., vol. 8, no. 1, pp. 495–505, Jan. 2021, doi: https://doi.org/10.1002/mrm.28396.

[13] Danieli E, Mauler J, Perlo J, Blümich B, Casanova F. “Mobile sensor for high resolution NMR spectroscopy and imaging,” *J Magn Reson*., vol.198, no. 1, pp.80-7, Jan. 2009, doi: https://doi.org/10.1016/j.jmr.2009.01.022.

[14] He, Y. et al. “Use of 2.1 MHz MRI scanner for brain imaging and its preliminary results in stroke,” *J. Magn. Reson.,* vol. 319, pp.106829, Oct. 2020, doi: 10.1016/j.jmr.2020.106829.

[15] Wright, S.M., Brown, D.G., Porter, J.R. et al. “A desktop magnetic resonance imaging system,” *MAGMA,* vol. 13, no. 3, pp.177–185, Aug. 2001, doi: https://doi.org/10.1007/BF02678594.

[16] Yoshioka, Hiroshi, Ito, Satoshi, Handa, et al. “Low-field compact magnetic resonance imaging system for the hand and wrist in rheumatoid arthritis,” *Journal of magnetic resonance imaging*, vol. 3, no. 23, pp. 370-376, Feb. 2006, doi: https://doi.org/10.1002/jmri.20501.

[17] McDaniel PC, Cooley CZ, Stockmann JP, Wald LL. “The MR Cap: A single-sided MRI system designed for potential point-of-care limited field-of-view brain imaging,” *Magnetic Resonance in Medicine*, vol. 82, no. 5, pp. 1946-1960, Nov. 2019, doi: https://doi.org/10.1002/mrm.27861.

[18] F. Zhao, X. Zhou, X. Xie and K. Wang, “Design of Gradient Magnetic Field Coil Based on an Improved Particle Swarm Optimization Algorithm for Magnetocardiography Systems, ” IEEE *Trans. Instrum. Meas.*, vol. 70, pp. 1-9, Aug. 2021, doi: 10.1109/TIM.2021.3106677.

[19] Dardo Tomasi. “Stream function optimization for gradient coil design,” *Magnetic Resonance in Medicine*, vol. 45, no. 3, pp. 505 – 512, Mar. 2001, doi: 10.1002/1522-2594(200103)45:3<505:AID-MRM1066>3.0.CO;2-HR.

[20] Turner. “A target field approach to optimal coil design,” *J. Phys. D.,* vol. 19, pp. L147-L151, May. 1986, doi: 10.1088/0022-3727/19/8/001.

[21] Z. Ding, Z. Huang, M. Pang and B. Han, “Design of Bi-Planar Coil for Acquiring Near-Zero Magnetic Environment,” IEEE *Trans. Instrum. Meas*, vol. 71, pp. 1-10, Feb. 2022, doi: 10.1109/TIM.2022.3151939.

[22] H. S. Lopez. “Equivalent Magnetization Current Method Applied to the Design of Gradient Coils for Magnetic Resonance Imaging,” *IEEE Trans. Magn.,* vol.45, no. 2, pp. 767-775, Feb. 2009, doi: 10.1109/TMAG.2008.2010053.

[23] M. A. Brideson, L. K. Forbes, and Crozier S. “Determining complicated winding patterns for shim coils using stream functions and the target-field method,” *Concepts in Magnetic Resonance Part A*, vol. 14, no. 1, pp. 9-18, Jan. 2002, doi: 10.1002/cmr.10000.

[24] Xu, Zheng and Qi, Jinfeng. “Equivalent magnetic dipole method for designing gradient coils of the Halbach magnetic resonance device”. *International Journal of Applied Electromagnetics and Mechanics*. Vol.56. pp.595-604, Jan. 2018, doi: 10.3233/JAE-170115.

[25] J. Yang, X. Zhang, B. Han, J. Wang and L. Wang, “Design of Biplanar Coils for Degrading Residual Field in Magnetic Shielding Room, ” IEEE *Trans. Instrum. Meas.*, vol. 70, pp. 1-10, 2021, doi: 10.1109/TIM.2021.3108493.

[26] F. Zhao, X. Zhou, W. Zhou, X. Zhang, K. Wang and W. Wang, “Research on the Design of Axial Uniform Coils for Residual Field Compensation in Magnetically Shielded Cylinder, ” IEEE *Trans. Instrum. Meas.*, vol. 71, pp. 1-9, 2022, doi: 10.1109/TIM.2022.3188525.

[27] W. A. Roshena and D. E. Turcotte. “Planar inductors on magnetic substrates,” *IEEE Trans. Magn.,* vol.24, no. 6, pp. 3213-3216, doi: 10.1109/20.92379.

[28] W. A. Roshen. “Effect of finite thickness of magnetic substrate on planar inductors,” *IEEE Trans. Magn*., vol. 26, no. 1, pp. 270-275, Jan. 1990, doi: 10.1109/20.50553.

[29] Prasad, Sachidananda and D. M. Vinod Kumar. “Trade-offs in PMU and IED Deployment for Active Distribution State Estimation Using Multiobjective Evolutionary Algorithm.” *IEEE Trans. Instrum. Meas.*, vol. 67,no.6, pp. 1298-1307, Feb.2018, doi: 10.1109/TIM.2018.2792890.

[30] Prasad, Sachidananda and D. M. Vinod Kumar. “Optimal Allocation of Measurement Devices for Distribution State Estimation Using Multiobjective Hybrid PSO–Krill Herd Algorithm.” *IEEE Trans. Instrum. Meas.*, vol. 66, no.8, pp. 2022-2035, Mar.2017, doi: 10.1109/TIM.2017.2674718.

[31] Yang, Chenglin. “Parallel–Series Multiobjective Genetic Algorithm for Optimal Tests Selection With Multiple Constraints.” *IEEE Trans. Instrum. Meas.*, vol. 67, no.8, pp. 1859-1876, Mar.2018, doi: 10.1109/TIM.2018.2809839.

[32] Y. P. Du and D. L. Parker, “Optimal design of gradient coils in MR imaging: Optimizing coil performance versus minimizing cost functions”, *Magn. Reson. Imag.,* vol.40, no.3, pp.500–503, Dec.2005, doi: https://doi.org /10.1002/mrm.1910400323.

[33] Cobos Sanchez, Clemente, Pantoja, Mario, Poole Michael, Bretones, A. "Gradient-Coil Design: A Multi-Objective Problem". *IEEE Trans. Magn.,* vol.48, no.6, pp. 1967-1975, Dec.2011, doi: https:// ieeexplore .ieee.org/document/6105573.

[34] F. Zhao, X. Zhou, X. Xie and K. Wang, "Design of Gradient Magnetic Field Coil Based on an Improved Particle Swarm Optimization Algorithm for Magnetocardiography Systems, " *IEEE Trans. Instrum. Meas.*, vol. 70, pp. 1-9, Aug. 2021, doi: 10.1109/TIM.2021.3106677.

[35] Dardo Tomasi. "Stream function optimization for gradient coil design", *Magn. Reson. Med.*, vol. 45, no.3, pp. 505-512, Feb.2001, doi: https://doi.org/10.1002/1522-2594(200103)45:3<505: AID-MRM1066>3.0.CO;2-H

[36] C. Z. Cooley et al., "Design of Sparse Halbach Magnet Arrays for Portable MRI Using a Genetic Algorithm," *IEEE Trans. Magn.,* vol. 54, no. 1, pp. 1-12, Jan. 2018, doi: 10.1109/TMAG.2017.2751001.

[37] O'Reilly T, Teeuwisse W M, Webb A G, "Three-dimensional MRI in a homogenous 27cm diameter bore Halbach array magnet," *Journal of magnetic resonance imaging*, vol. 307, no. 106578, Oct. 2019, doi: 10.1016/j.jmr.2019.106578.

[38] Liang T O, Koh Y H, Qiu T, et al, "High-Performance Permanent Magnet Array Design by a Fast Genetic Algorithm (GA)-based Optimization for Low-Field Portable MRI," *Journal of magnetic resonance imaging*, vol. 345, no. 107309, Dec. 2021, doi: 10.1016/j.jmr.2022.107309.

[39] Patrick C. McDaniel, Clarissa Zimmerman Cooley, et al, "The MR Cap: A single-sided MRI system designed for potential point-of-care limited field-of-view brain imaging," *Magnetic Resonance in Medicine*, vol. 82, no. 5, pp. 1946-1960, Nov. 2019, doi:10.1002/mrm.27861

[40] Mercy H. Mazurek, Bradley A. Cahn, Matthew M. Yuen, et al, "Portable, bedside, low-field magnetic resonance imaging for evaluation of intracerebral hemorrhage," *Nature communications*, vol.12, no.1, pp. 5119, Aug.2021, doi: https://doi.org/10.1038/s41467-021-25441-6.

[41] Liu Y, Leong A T L, Zhao Y, et al, "A low-cost and shielding-free ultra-low-field brain MRI scanner," *Nature communications*, vol.12, no.1, pp. 1-14, Dec. 2021, doi: DOI: 10.1038/s41467-021-27317-1.

[42] He Y C, He W, Tan L, et al, "Use of 2.1 MHz MRI scanner for brain imaging and its preliminary results in stroke," *Journal of magnetic resonance*, vol. 319, no. 106829, Oct. 2020, doi: 10.1016/j.jmr.2020.106829.

[43] T. Sato, K. Watanabe, and H. Igarashi, “Multimaterial Topology Optimization of Electric Machines Based on Normalized Gaussian Network,” *IEEE Trans. Magn.*, vol. 51, no. 3, pp.1-4, Mar. 2015, doi: 10.1109/TMAG.2014.2359972.

[44] H. Sasaki and H. Igarashi, "Topology Optimization Accelerated by Deep Learning," *I IEEE Trans. Magn.*, vol. 55, no. 6, pp. 1-5, Jun. 2019, 10.1109/TMAG.2019.2901906.

[45] D. -C. Dang et al., "Escaping Local Optima Using Crossover With Emergent Diversity," *IEEE Trans. Evolut. Comput.*, vol. 22, no. 3, pp. 484-497, Jun. 2018, doi: 10.1109/TEVC.2017.2724201.

[46] J.M. Jin, Electromagnetic Design and Analysis in Magnetic Resonance Imaging, CRC, Boca Raton, FL, 1999.

[47] I. Frollo, P. Andris, I. Strolka, “Measuring method and magnetic field homogeneity optimization for magnets used in NUM-imaging”, *Measurement Science Review*, vol.1, no.1, pp.9-12, Jan. 2001, doi: https://www.measurement.sk/PAPERS/Frollo5.pdf.

[48] F. Romeo, D.I. Hoult, “Magnet field profiling: analysis and correcting coil design,” *Magnetic resonance in medicine*, vol.1, no. 1, pp.44-65, Mar. 1984, doi:10.1002/mrm.1910010107.

[49] B. Dorri, M.E. Vermilyea, W.E. Toffolo, “Passive shimming of MR magnets: algorithm, hardware, and results,” *IEEE Transactions on Applied Superconductivity*, vol.3, no.1, pp. 254–257, Mar. 1993, doi: 10.1109/77.233719.

[50] A. Belov, V. Bushuev, “Passive shimming of the superconducting magnet for MRI,” *IEEE Transactions on Applied Superconductivity*, vol. 5, no. 2, pp. 679–681, Jun. 1995, doi: 10.1109/77.402639.

[51] H.S. Lopez, F. Liu, E. Weber, S. Crozier, “Passive shim design and a shimming approach for biplanar permanent magnetic resonance imaging magnets,” *IEEE Transactions on Magnetics,* vol. 44, no. 3, pp. 394–402, Mar. 2008, doi: 10.1109/TMAG.2007.914770.

[52] L. Hong, D. Zu, “Shimming permanent magnet of MRI scanner,” *Piers Online*, vol. 3, no. 6, pp. 859-864, Jan.2007.

[53] Y. Zhang, D. Xie, B. Bai, H.S. Yoon, C.S. Koh, “A novel optimal design method of passive shimming for permanent MRI magnet,” *IEEE Transactions on Magnetics,* vol. 44, no. 6, pp. 1058–1061, May. 2008, doi: 10.1109/TMAG.2007.916267.

[54] S. Noguchi, S. Kim, S. Hahn and Y. Iwasa, "Passive Shimming by Eliminating Spherical Harmonics Coefficients of all Magnetic Field Components Generated by Correction Iron Pieces," *IEEE Transactions on Magnetics*, vol. 50, no. 2, pp. 605-608, Feb. 2014, doi: 10.1109/TMAG.2013.2276736.

[55] J. Wang et al., "Design and Shimming Method of Low Length-to-Interdiameter Ratio Halbach Magnet," *IEEE Transactions on Instrumentation and Measurement*, vol. 71, pp. 1-10, 2022, doi: 10.1109/TIM.2022.3199233.

[56] M. A. Bernstein, K. F. King, X. J. Zhou., "Handbook of MRI pulse sequences.", *Elsevier Academic Press*, MA, USA, 2004, pp:104-105.

[57] Magnetic resonance equipment for medical imaging - Part 1: Determination of essential image quality parameters, IEC 62464-1, 2007.

[58] Igarashi, H., Watanabe, K., Kost, A. "A reduced model for finite element analysis of steel laminations". *IEEE Transactions on Magnetics*, vol.42, no.4, pp. 739 - 742, Mar.2006, doi: https://ieeexplore.ieee.org/document/1608312.

[59] T. Kabashima, A. Kawahara and T. Goto, "Force calculation using magnetizing currents," *IEEE Transactions on Magnetics,* vol. 24, no. 1, pp. 451-454, Jan. 1988, doi: 10.1109/20.43954.

Acknowledgement

I would like to express my deepest gratitude to my supervisor, Professor Hajime Igarashi, for his invaluable guidance, unwavering support, and continuous encouragement throughout my doctoral journey. His expertise, patience, and dedication to my research have been instrumental in shaping this work.

I am also grateful to Professor Xu Zheng at Chongqing University for his invaluable influence on me in the field of MRI, as well as for providing access to a top-notch experimental platform. He has been a constant source of inspiration, pushing me to explore new ideas and tackle new challenges.

I extend my appreciation to my colleagues at Applied Electromagnetic Laboratory of Hokkaido University, and low-field MRI laboratory of Chongqing University, whose stimulating discussions and collaborative spirit have enriched my research experience.

I would like to acknowledge the financial support provided by Japan Science and Technology Agency (JST) Support for Pioneering Research Initiated by the Next Generation (SPRING) during my doctoral studies. Without their support, this research would not have been possible.

My sincere thanks go to my friends and family for their unwavering belief in my abilities and their constant encouragement. Their emotional support sustained me through the challenges of this academic journey. Lastly, I want to express my gratitude to all the participants who generously contributed their time and expertise to this research project.

Kong Xiaohan

2023.09.07

Research Achievements

Journal papers

[1] **X. Kong**, Z. Xu, S. Sheng, J. Wu, Y. He, L. Xuan and H. Igarashi, “Gradient Coil Design Method Specifically for Permanent-Magnet-Type Low Field Portable MRI Brain Scanner,” *IEEE Transactions on Instrumentation and Measurement*, vol. 72, pp. 1-12, 2023, doi: 10.1109/TIM.2022.3225042.

[2] **X. Kong**, Z. Xu, S. Sheng, J. Wu, Y. He, and H. Igarashi, “Z-gradient Coil Design with Improved Anti-Eddy Performance for MRI system with Opposed Permanent Magnets,” *Applied Magnetic Resonance*, vol. 54, pp. 869–890, Jul. 2023, doi: https://doi.org/10.1007/s00723-023-01577-0.

Other journal papers

[1] **X. Kong**, Y. Zhu, S. Sheng, J. Wu, Y. He, M. Hong and Z. Xu, “A Low-cost Portable 50 mT MRI Scanner for Dental Imaging” *IEEE Transactions on Instrumentation and Measurement*, doi: 10.1109/TIM.2023.3329089.

[2] X. Xu, **X. Kong**, J. Zhang, G. Wang, Z. Bao, H. Yu, Z. Xu, "Optimization of Inside-Out Nuclear Magnetic Resonance Sensor With Logging-While-Drilling Tool Specification and Experimental Validation," *IEEE Transactions on Instrumentation and Measurement*, vol. 71, pp. 1-10, 2022, doi: 10.1109/TIM.2022.3169572.

[3] S. Shen, **X. Kong**, F. Meng, J. Wu, Y. He, P. Guo, Z. Xu, “An optimized quadrature RF receive coil for very-low-field (50.4 mT) magnetic resonance brain imaging,” Journal of Magnetic Resonance, vol. 342, no. 107269, Sep. 2022, doi: 10.1016/j.jmr.2022.107269.

[4] L. Xuan, **X. Kong**, J. Wu, Y. He, Z. Xu, "A Smoothly-Connected Crescent Transverse Gradient Coil Design for 50mT MRI System," *Applied Magnetic Resonance,* vol. 52, doi: 10.1007/s00723-021-01330-5.

International conferences

[1] **X. Kong**, Z. Xu and H. Igarashi, Equivalent Image Magnetic Dipole Method Considering the Magnetic Effect of Ferromagnetic Material Applied in Gradient Coil Design, (COMPUMAG 2022), online, Jan. 2022.

[2] **X. Kong**, Z. Xu and H. Igarashi, Multi-fidelity Topology Optimization of Portable Low-field MRI Device, (COMPUMAG 2023), Kyoto, Japan, May, 2023.

[3] **X. Kong**, Z. Xu, H. Igarashi, Multi-objective Optimization of Inductors Based on Neural Network, (OIPE 2023), Graz, Austria, Sep.2023.

Domestic conferences

[1] **X. Kong**, Z. Xu and H. Igarashi, Equivalent Image Magnetic Dipole Method for Gradient Coils Design in Bi-planar-magnet MRI Devices, 第 31 回 MAGDA コンファレンス, OS-4-13, Sep, 2022, Oral.

[2] **X. Kong** and H. Igarashi, Optimal Design of Passive Shimming for a 50mT Portable MRI Device, Oral presentation, 電気学会静止器/回転機 合同研究会, SA-23-022, RM-23-022, Mar, 2023, Oral.